Analysis and Control of Electromechanical Oscillations in Renewable-Integrated Power Systems

by Balakrushna Sahu



DEPARTMENT OF ELECTRICAL ENGINEERING

INDIAN INSTITUTE OF TECHNOLOGY ROPAR

June 2024

Analysis and Control of Electromechanical Oscillations in Renewable-Integrated Power Systems

A

Thesis Submitted
In the Partial Fulfilment of the Requirements
for the Degree

DOCTOR OF PHILOSOPHY

by

Balakrushna Sahu (2018EEZ0005)

Under the Guidance of Dr. Bibhu Prasad Padhy



DEPARTMENT OF ELECTRICAL ENGINEERING

INDIAN INSTITUTE OF TECHNOLOGY ROPAR

June 2024

COPYRIGHT ©2024

All Rights Reversed
Indian Institute of Technology Ropar



Declaration of Originality

I hereby declare that the work which is being presented in the thesis entitled Analysis and Control of Electromechanical Oscillations in Renewable-Integrated Power Systems has been solely authored by me. It presents the result of my independent investigation/research conducted during the period from July 2018 to June 2024 under the supervision of Dr. Bibhu Prasad Padhy, Assistant Professor, IIT Ropar. To the best of my knowledge, it is an original work, both in terms of research content and narrative, and has not been submitted or accepted elsewhere, in part or in full, for the award of any degree, diploma, fellowship, associateship, or similar title of any university or institution. Further, due credit has been attributed to the relevant state-of-the-art and collaborations with appropriate citations and acknowledgments in line with established ethical norms and practices. I also declare that any idea/data/fact/source stated in my thesis has not been fabricated/ falsified/ misrepresented. All the principles of academic honesty and integrity have been followed. I fully understand that if the thesis is found to be unoriginal, fabricated, or plagiarized, the Institute reserves the right to withdraw the thesis from its archive and revoke the associated Degree conferred. Additionally, the Institute also reserves the right to appraise all concerned sections of society of the matter for their information and necessary action. If accepted, I hereby consent for my thesis to be available online in the Institute's Open Access repository, inter-library loan, and the title & abstract to be made available to outside organizations.

Signature

Balakrushna Sahu

2018EEZ0005

Ph.D.

Department of Electrical Engineering

Indian Institute of Technology Ropar Rupnagar, Punjab 140001

ACKNOWLEDGEMENT

I would like to extend my sincere gratitude to my thesis supervisor, Dr. Bibhu Prasad Padhy, without whose valuable guidance, persistent support, and encouragement throughout my Ph.D journey, the thesis would not have been completed. I am deeply grateful for his stronghold on research concepts, crucial advice, and kindness towards me and my family. These have been the key pillars to form the foundation upon which my thesis rests.

I profoundly appreciate the administration of the Indian Institute of Technology, Ropar, for offering a great opportunity, conducive research infrastructure, and institute fellowship to smoothly accomplish my Ph.D research program. I wish to express my heartfelt appreciation to my respected teachers as well as Doctoral Committee (DC) members Dr. C. C. Reddy (Chair Person), Dr. Ranjana Sodhi, Dr. Smruti Ranjan Behera, and Dr. Kailash Chandra Jena for their valuable suggestions and timely support.

I deeply acknowledge the continuous support and consistent motivation throughout my journey furnished by Digamber Kumar, Subal Beura, Dr. Satish Kumar Ancha, Sourav De, Mahesh Pundru Reddy, Ritesh Kumar, Manish Kumar, Dr. Baibhav Kumar Gupta, Dr. Vaibhav Shah, Dr. Mehtab Alam, Dr. Shitikanth dash and many more. I am grateful to all those who have provided support, both directly and indirectly, throughout this endeavor.

I immensely thank my parents, Sri Kamal Lochan Sahu and Smt. Pramodini Sahu, my inlaw parents Prof. Sri Sukanta Panda and Smt Sanjukta Panda, my wife Mrs. Lipika Panda, brother Mr. Nimain Charan Sahu, Mr. Priya Ranjan Sahu, and sister Mrs. Bishnupriya Panda, brother-in-law Mr. Dandapani Panda, nephews Om Prakash and Krushna Chandra for their selfless support, trust, and prayer. At last, my special thanks go to my sweet and beloved daughter Annie (Asima Sahu), whose infectious smile and unconditional love have been my source of strength and refreshment throughout my Ph.D endeavor.

Balakrushna sahu

210, Electrical Department, J C Bose Block Indian Institute of Technology Ropar June, 2024.

CERTIFICATE

This is to certify that the thesis entitled Analysis and Control of Electromechanical Oscillations in Renewable-Integrated Power Systems, submitted by Balakrushna Sahu (2018EEZ0005), for the award of the degree of Doctor of Philosophy of Indian Institute of Technology Ropar, is a record of bonafide research work carried out under my guidance and supervision. To the best of my knowledge and belief, the work presented in this thesis is original and has not been submitted, either in part or full, for the award of any other degree, diploma, fellowship, associateship or similar title of any university or institution.

In my opinion, the thesis has reached the standard of fulfilling the requirements of the regulations relating to the Degree.

Signature of the Supervisor

Dr. Bibhu Prasad Padhy

Department of Electrical Engineering

Indian Institute of Technology Ropar

Rupnagar, Punjab-140001, India.

June, 2024

Abstract

In response to global climate change, there has been a significant shift in energy generation towards sustainable, renewable energy sources, with an increasing focus on wind and solar-based renewable sources. Continued global collaboration, international cooperation, and national commitments are significant global efforts involving more economic investments and technological research that cause the widespread transition from fossil fuel to adopting more sustainable and low-carbon energy for future generations. Rapid developments of renewable sources worldwide, their intermittent characteristics, complex control architecture, and characteristics of dynamic response have issued major challenges in the stability of modern power systems.

Therefore, it is essential to explore the dynamic interaction between the various control loops of renewable sources and synchronous generators of the power system. One of the major aspects to consider in addressing such concerns is understanding the synchronizing/damping torque offered by renewable sources to the electromechanical oscillation loop of the synchronous generator. In this regard, the work explores the major impacts and challenges arising from the increasing penetration of wind or solar-based renewable sources into power systems. Further, it explores the major impacts and challenges arising from the growing penetration of wind and solarbased renewable sources into power systems. A unique methodology is proposed to evaluate the impact of various system parameters on the damping torque offered by the Doubly-Fed Induction Generator-based (DFIG-based) Wind Energy System (WES) to the Electromechanical Oscillation Loop (EOL) of the Rest of the Power Systems (RPS). Furthermore, a new method of Power System Stabilizer (PSS) design is proposed for a power system that contains a DFIG-based wind farm enabled with a Virtual Inertial Controller (VIC) and Phase Locked Loop (PLL) and also presents a unique methodology of probabilistic small signal stability analysis of power systems consisting of large-scale SPVs, which is performed considering various parameters and their uncertainties. Ranking of all the generator buses of a power system is obtained by probabilistic modal sensitivity analysis based on different Sensitivity Analysis (SA) tools such as (a) Sobol Sensitivity Analysis, (b) Random Balance Designs - Fourier Amplitude Sensitivity Test (RBD -FAST), (c) Delta Moment, and (d) Pianosi and Wagener (PAWN) on the power system by replacing

each generator with a similarly rated Solar Photo-Voltaic (SPV) system under the uncertainties of load variations and generator output.

Keywords: DFIG-based wind energy systems, solar photo-voltaic systems, virtual inertia controller, phase locked loop, small-signal analysis, synchronizing/damping torque, synchronous generator, power system stabilizer, probabilistic modal analysis

Contents

Abst	ract		X
Glos	sary		, XV
List	of Figu	res	xvi
List	of Table	esx	viii
Chap	oter 1	State-of-the-Art	1
1.1	Motiv	vation	1
	1.1.1	Climate Change	1
	1.1.2	Energy Transformation	2
	1.1.3	Wind Power Technology	3
	1.1.4	Solar Photo-Voltaic (SPV) System	3
1.2	Resea	arch Objective	5
1.3	Litera	ature Review	6
	1.3.1	Grid Integration of DFIG-Based WES and its Impact on Power System	6
	1.3.2	Stability analysis DFIG-based WES with VIC	8
	1.3.3	Oscillatory Stability Analysis of SPV-Integrated Power System	9
	1.3.4	Impact of SPV with VIC on stability of power system	11
1.4	Conti	ribution Overview	. 12
1.5	Struc	ture of the Thesis	. 13
	oter 2	Investigation of Damping Torque Offered by DFIG to the EOL of RPS for	17
		Various System Parameters	
2.1		duction	
2.2	-	ct of System Parameter on Damping of Low-Frequency Inter-Area Mode	
2.3	•	ytical and Simulation Results	
		Study of damping torque influenced by line reactance	
		Influence voltage on damping torque contribution	
	2.3.3	Effect of H constants on damping torque contributions	. 35
	2.3.4	Influence of bus voltage and machine inertia constant on damping contributions.	. 37
	2.3.5	Damping contribution influenced by the location of WES	. 37
2.4	Discu	ussions and results on multimachine test systems	. 39

	2.4.1	39 bus test systems	39
2.5	Conc	lusion	43
Chapter 3 Systems		Small Signal Stability Analysis of DFIG-based Wind Energy-Integrated Power 47	
3.1	Intro	duction	47
3.2	Mode	el of DFIG-Based Wind-Integrated Power System	48
	3.2.1	Modeling of a Mechanical System	48
	3.2.2	Modeling of DFIG	50
	3.2.3	Modeling of Controllers Associated with Converters	50
3.3	Dyna	mic Modeling of an SMIB with a DFIG-based WES	52
3.4	Desig	gn Algorithm for PSS	56
3.5	Effec	t VIC and PLL on Synchronizing and Damping Torque	58
3.6	Resu	lt and Analysis	62
	3.6.1	SMIB System	62
	3.6.2	Modified 9-bus Test System	67
3.7	Conc	lusion	70
	oter 4 em Unc	Modal Sensitivity Analysis of Large-Scale PV-Integrated Power System U	
4.1		duction	
4.2		al Sensitivity Analysis Methods	
		Sobol sensitivity analysis [89]	
		Random Balance Designs - Fourier Amplitude Sensitivity Test (RBD-FAST) [76	
	4.2.3	Delta Moment Independent Measure (Borgonovo indices) [91]	77
	4.2.4	PAWN Sensitivity Indices [92]	78
	4.2.5	Sampling	78
4.3	Syste	m Under Study and Uncertainties	79
	4.3.1	Study of the solar PV (SPV) systems in place of the SGs:	80
	4.3.2	Identify the most influential parameter of the modified IEEE 39 bus system	84
4.4	Inerti	al Distribution of Modified NETS	87
4.5	Parar	neter Tunning of VIC-based BESS with PSS of SGs	88
4.6	Resu	Its and Discussions	90
4.7	Conc	lusion	92

	ı v	Evaluation of Power System Oscillatory Modes Under the Influence of PV- nics95	
5.1	Introduction	95	
5.2	Small Signal Modeling of PV-BESS-Based Power Systems	96	
	5.2.1 Modeling of PV inverters	96	
	5.2.2 Model BESS Controllers	98	
5.3	Stochastic Model Analysis of PV-BESS-Integrated Power System	100	
5.4	Results and Discussions:	101	
	5.4.1 Power System without PV-BESS	102	
	5.4.2 Power system with PV-BESS	102	
5.5	Conclusion	107	
Chap	pter 6 Conclusion and Future Scope	109	
6.1	Recap of Main Contributions	109	
6.2	Summary of the Key Findings	110	
6.3	Future Research Scope	113	
App	endix A	115	
App	endix B	125	
Refe	rences	127	

Glossary

AC Alternating Current SPE Sensitive PSS Effect

BESS Battery Energy Storage System SPV Solar PV

COI Center of Inertia VIC Virtual Inertia Controller

DAE Differential and Algebraic Equations WES Wind Energy System

DC Direct Current WTG Wind Turbine Governor

DFIG Doubly Fed Induction Generator

DMIM Delta-Moment Independent Measure

EmOM Electromechanical Oscillatory Mode

EOL Electromechanical Oscillation Loop

GSAT Global Sensitivity Analysis Techniques

GSC Grid Side Converter

LEOs Low-frequency Electromechanical Oscillations

MPPT Maximal Power Point Tracking

PAWN Pianosi and Wagener

PCC Point of Common Coupling

PI Proportional Integral

PLL Phase Locked Loop

PMSG Permanent Magnet Synchronous Generator

POM PLL Oscillation Mode

PSS Power System Stabilizer

PSO Particle Swarm Optimization

PV Photovoltaic

RBD-FAST Random Balance Design Fourier Amplitude Sensitivity Test

RES Renewable Energy System

RPS Rest of the Power System

RSC Rotor Side Converter

SFR System Frequency Regulation

SOC State of Charge

List of Figures

Figure 1.1 Growth of generations from Renewable sources [2]	. 2
Figure 1.2 Schematic of DFIG-based WES	. 4
Figure 1.3 Schematic of an SPV system	. 5
Figure 2.1 Two-machine system with wind farm at bus 3	19
Figure 2.2 Control loop between RPS and WES	20
Figure 2.3 Wind generators in a wind farm	22
Figure 2.4 Rotor Side Converter Controllers: (a) Active power controller (b) Reactive power	
controller	24
Figure 2.5 Magnitude plot of DFIG-based WES	27
Figure 2.6 Close-loop interconnection between RPS and DFIG-based WES	28
Figure 2.7 Flow chart of the proposed work	31
Figure 2.8 Damping torque affected by varying line reactance	32
Figure 2.9 Impact of line reactance on WES states participation in the system low-frequency	
EmOM	33
Figure 2.10 Damping torque contribution due to variation of bus voltage	34
Figure 2.11 Impact of bus voltage on WES states participation in the system low-frequency	
EmOM	35
Figure 2.12 Damping toque contribution for various values of inertia constants	35
Figure 2.13 Impact of machine inertia on WES states participation in the system low-frequency	Į
EmOM	36
Figure 2.14 Damping contribution due to variation in bus voltage and inertia constants of	
synchronous machines	36
Figure 2.15 Damping contribution corresponds to various locations of WES	38
Figure 2.16 Locus of inter-area oscillation mode when the location of WES is varied from M1	to
M2	38
Figure 2.17 Configuration of 39 bus test system with relative distance of buses from COI	40
Figure 2.18 Index of Electrical distance from COI among buses of 39-bus systems	41
Figure 2.19 Generators' rotor angular velocity for three-phase fault at bus 15	43

Figure 3.1 Modified SMIB system	49
Figure 3.2 A Model of SRF PLL	55
Figure 3.3 Modified Phillip Heffron Model	57
Figure 3.4 Change in ΔP_S and ΔP_D for (a) location 1, Prop. PSS1 (b) Location 2, Prop.	PSS2
	63
Figure 3.5 Dynamic response for different values of Kinert	64
Figure 3.6 Change in $\triangle PS$ and $\triangle PD$ for (a) Proposed PSS. (b) CPSS	66
Figure 3.7 Root locus of SG	66
Figure 3.8 Simulation result of fault response of proposed and conventional PSS	67
Figure 3.9 Modified IEEE 9 bus test system	69
Figure 3.10 Three-phase fault response of 9 bus system for (a)Generator load angle (δ 2) a	nd (b)
Power output from WES, (Pw) with variation of Kinert	69
Figure 3.11 Root locus of Generator 2	70
Figure 3.12 Simulation result of (a)Generator load angle (δ 2) and (b) Power output from V	WES,
(Pw) for three-phase fault at bus 5 of 9-bus system	70
Figure 4.1 Flow chart for sensitivity analysis by different SA methods	81
Figure 4.2 Probabilistic distribution of the damping ratio of most critical eigenvalue	82
Figure 4.3 Modified IEEE 39 bus NETS	85
Figure 4.4 Indexing of busses as per the electrical distance from COI of modified IEEE 39	bus
test system	88
Figure 4.5 VIC Enabled PV-BESS system.	88
Figure 4.6 The real power flow of $L4 - 14$ due to BESS at $B22$.	91
Figure 4.7 The real power flow of $L4 - 14$ due to BESS at different busses	91
Figure 5.1 Schematic of grid-integrated PV-BESS system	97
Figure 5.2 The Proposed algorithm of Monte Carlo Simulation	101
Figure 5.3 Modified IEEE 39 bus test system	103
Figure 5.4 Stochastic Solar Irradiance data	104
Figure 5.5 Probabilistic Distribution function of critical eigenvalues	105

List of Tables

Table 1.1: Pros and Cons of Type 3 and Type 4-based WES 4
Table 2.1: Torque Contribution to SGs of IEEE 39 Bus System 42
Table 2.2: Inter-Area Modes for Open Loop RPS and Close Loop Interconnection of RPS and
WES
Table 2.3: Error Norm of The Generator Rotor Angle Velocity w.r.t ωn 43
Table 3.1: PSS Parameters for Locations 1 and 2 63
Table 3.2: Parameters of Proposed PSS and CPSS 65
Table 3.3: Proposed PSS and CPSS Parameters for G2 of Modified IEEE 9 Bus Test System 68
Table 4.1: Modeling of uncertainties of various power system components
Table 4.2: SIcum of All Uncertain Parameters by Different SA Methods 83
Table 4.3: Ranking of SGs to be replaced by an SPV considering system uncertainties 83
Table 4.4: Electromechanical Modes of Modified IEE 39 bus NETS 84
Table 4.5: Sensitivity of different uncertain parameters considered for the modified IEEE 39 bus
system
Table 4.6: SPE of Each Synchronous Generator 89
Table 4.7: Parameter of VIC and PSS 90
Table 5.1: Parameters of PV-BESS Controllers 102
Table 5.2: Inter-Area Modes of IEEE 39 Bus Test System Without PV-BESS 102
Table 5.3: Critical Eigen Modes of IEEE 39 Bus Test System With PV-BESS
Table 5.4: Mean And Variance of Critical Modes 106

xviii

Chapter 1

State-of-the-Art

This chapter highlights the background of different renewable sources and their impact on power system stability. To combat climate change and continuous technological development in sustainable sources, renewable sources have rapidly grown worldwide; their intermittent characteristics, complex control architecture, and characteristics of dynamic response have issued major challenges in the stability of modern power systems. In this regard, it is essential to explore the dynamic interaction between the various control loops of renewable sources and synchronous generators of the power system. This chapter introduces the state-of-art of renewable energy generation from sustainable sources like solar or wind and their influence on power system dynamic stability.

1.1 Motivation

1.1.1 Climate Change

Climate change is clearly observed from the continuous rise of average global temperature and its impact on the world's climate system. The air temperature on Earth has gone to an all-time high since post-industrialization. A study on global temperature analysis conducted by a group of scientists of the National Aeronautics and Space Administration (NASA), USA, indicates that the earth's air temperature has reached little more than 1° *C*, since 1880 [1]. Compared to previous years, the current condition of the global warming effect on the earth's health is more rapid and primarily caused by the large-scale burning of fossil-based energy resources. Nearly 75% of total greenhouse gas emissions and 90% of total carbon dioxide emissions are from fossil-based energy generation only. To combat global warming, the Paris Agreement was adopted by 196 parties across the globe on 12th December 2015. The Paris Agreement then became effective in December 2016 with three main objectives: (a) The global average temperature must be limited well below 2° *C* rise since the pre-industrial level, (b) the carbon emission should be reduced to 45% by 2030, and (c) zero carbon emissions should be achieved by 2050 [1].

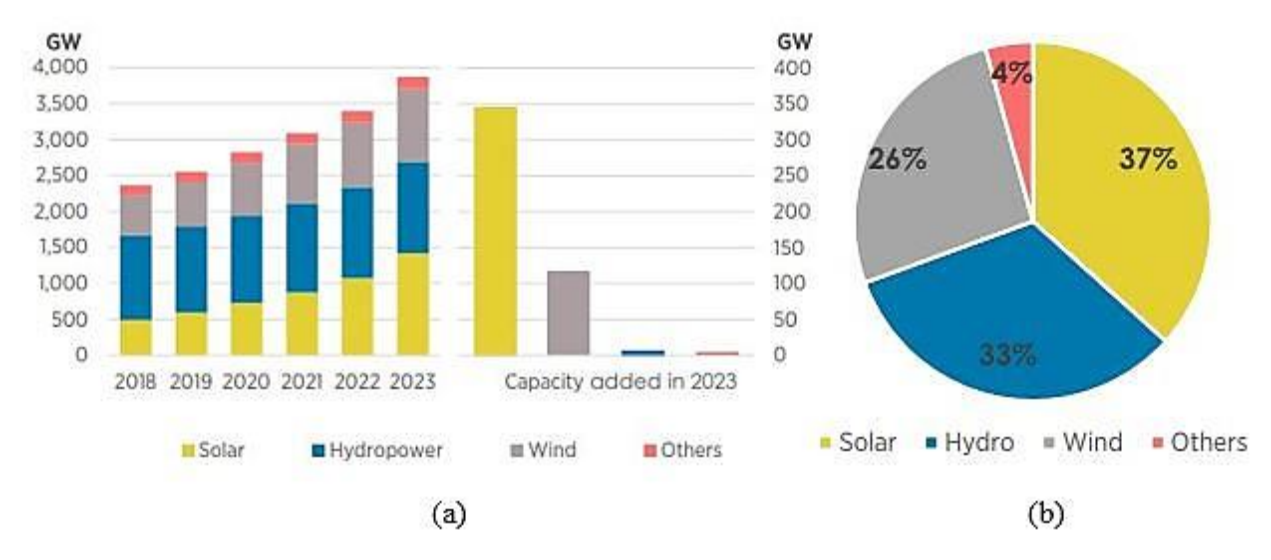


Figure 1.1 Growth of generations from Renewable sources [2]

1.1.2 Energy Transformation

Substantial acceleration in the energy sector in the post-Paris Agreement was pursued to meet the roadmap outlined in the Paris Agreement, which primarily centered on renewable energy, electrification, and energy efficiency. Further, increasing electricity demands and greater awareness of the environmental effects of fossil fuels have prompted efforts to develop cleaner and more efficient energy sources. The swift global transitions of renewable energy generations and their efficient harness of electrification is the culmination of recent innovations in powerelectronic converters. Further, continued global collaboration, international cooperation, and national commitments are significant global efforts involving more economic investments and technological research that cause the widespread transition from fossil fuel to adopting more sustainable and low-carbon energy resources for future generations. As a result, the global participation of total installed capacity has reached 3870 GW by the end of 2023 [2]. The yearwise growth of global installed capacity in renewable energy resources can be viewed in Figure 1.1. It is apparent from Figure 1.1 (b) that besides hydropower, solar and wind contribute to the remaining installed capacity of renewable-based energy generation with a total of 1053 GW (37%) and 1017 GW (26%), respectively. Figure 1.1 (a) exhibits the year-wise growth of the installed capacity of renewable sources from 2018 to the end of 2023. It can be observed that the total installation of renewables has grown by 13.9 %, with 473 GW during 2022. In the year 2023, the solar power generation increase continued to be at the top by adding 346 GW with a +32.2%increase, followed by the wind of 116 GW with a +12.9% growth. Hence, the growth of solar and wind can be seen as the two dominant renewable sources from all possible sustainable sources that contribute to meeting the power demand with the cleanest way of power generation, as outlined by the Paris Agreement.

1.1.3 Wind Power Technology

Wind power is one of the most dominant renewable sources that has the potential to fulfill the growing electricity demand with technological advances, starting from wind turbine generators to complex converter control loops. Despite intermittence characteristics, wind power is a popular renewable source because of (a) clean energy with zero risk of energy exhaustion, (b) low installation cost, (c) lower operational/maintenance cost [3], and (d) its quick payback period [4]. Having these given characteristics, the installed capacity of wind power production has increased in recent years. Wind power is produced by four different types of technologies such as: (a) Type 1, (b) Type 2, (c) Type 3, and (d) Type 4 [5]. Type 1 and Type 2 are induction generator-based Wind Energy Systems (WES), whereas Type 3 and Type 4 are Doubly-Fed Induction Generators (DFIG) and Permanent Magnet Synchronous Generators (PMSG), respectively. In recent years, Type 3 and Type 4-based WES have become more popular due to their respective pros and cons provided in Table 1.1. Using Type 3-based WES is advantageous over Type 4 primarily because Type 3 requires a smaller capacity converter than its rating. In contrast, PMSG necessitates a converter with a rating matching its full capacity. The Wind Turbine Generator (WTG) considered in this thesis is the DFIG-based WES (Type 3). The schematic of DFIG-based WES can be represented in Figure 1.1. Figure 1.2 illustrates that the wind-generated power is AC and is injected into the power system through the stator and rotor. Additionally, the rotor is connected to the grid through two stages of the DC-AC converter: the Rotor Side Converter (RSC) and Grid Side Converter (GSC). In the case of DFIG-based WES, the rotor deals with nearly 30 % of the total power exchange at the Point of Common Coupling (PCC) [6]. Hence, the rating of the DFIG-based wind system is moderate compared to PMSG.

1.1.4 Solar Photo-Voltaic (SPV) System

As illustrated in Figure 1.1, Solar Photo-Voltaic (SPV) systems are the fastest emerging renewable energy resource. Electricity is extracted from solar energy through PV arrays. PV arrays are formed by series-parallelly connected PV modules that collect solar lights and convert them into electricity [7]. The schematic illustrating a standard solar PV system is depicted in Figure 1.3.

Table 1.1: Pros and Cons of Type 3 and Type 4-based WES

Doubly Fed Induction Generator (DFIG)			
Pros:	Cons:		
Limited turbine speed range −30 % to 30 % around	Need of gearbox, Slip		
synchronous speed	rings		
Small capacity converter rating			
Complete control over the active and reactive powers			
The magnitude and frequency of terminal voltage can be			
maintained no matter the value of wind velocity on the wind			
turbine rotor.			
Permanent Magnet Synchronous Generator (PMSG)			
Pros:	Cons:		
No need for a gear system	PMSG needs a full-scale		
There is no requirement for a power converter for the field, and it	power converter.		
needs a full-rated capacity converter rating.			
Active and reactive power can be controlled completely.			
Brushless and low maintenance.			

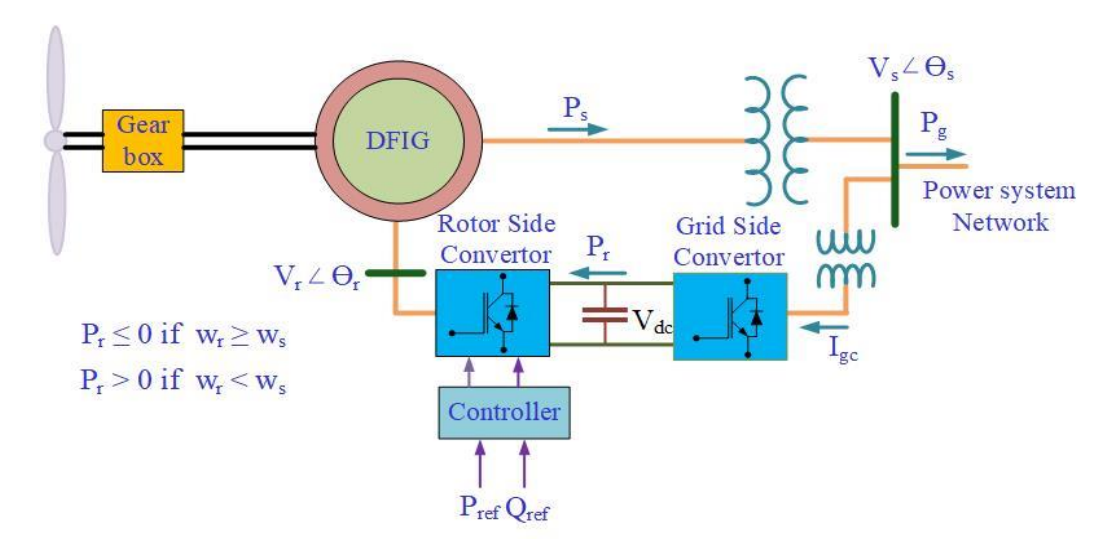


Figure 1.2 Schematic of DFIG-based WES

The electricity generated from PV arrays is in DC and has a very low voltage. Hence, DC output from PV arrays undergoes a DC-DC boost converter to increase the voltage level. Subsequently, the DC from the boost converter is connected through a DC-AC inverter and transformer.

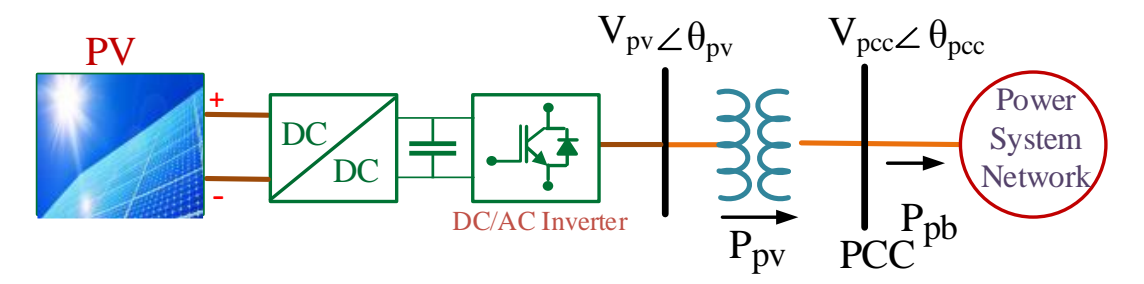


Figure 1.3 Schematic of an SPV system

Wind and solar power production is highly intermittent, as they depend on weather conditions that are not constantly available. In the case of grid integration, the intermittency of wind and solar poses challenges to grid stability and reliability, as energy generation may not align with peak demand periods. Rapid developments of renewable sources worldwide, their intermittent characteristics, complex control architecture, and characteristics of dynamic response have issued major challenges in the stability of modern power systems. Therefore, it is very important to explore the dynamic interaction between the various control loops of renewable sources and synchronous generators of the power system. One of the major aspects to consider in addressing such concerns is understanding the synchronizing/damping torque offered by renewable sources to the electromechanical oscillation loop of the synchronous generator.

1.2 Research Objective

The overarching goal of the thesis is to investigate the synchronizing/damping torque offered by renewable sources to the electromechanical oscillation loop of the synchronous generator. The set goal of the thesis is pursued by the following research objectives:

- 1. Investigation of the damping torque offered by DFIG-based WES:
 - a) To develop an analytical model of a DFIG-based WES-integrated power system.
 - b) To derive a mathematical expression of the damping torque offered by WES on the Electromechanical Oscillation Loop (EOL) of the Rest of the Power Systems (RPS) as a function of various system parameters.
 - c) Further, to validate the analytical outcome through the time domain simulation.
- 2. Impact Phase Locked Loop (PLL) and Virtual Inertia Controller (VIC) on synchronizing/damping torque contributed by DFIG-based WES:

- a) To develop mathematical relationships between synchronizing/damping torque contributed by DFIG-based WES and control parameters of PLL and VIC.
- b) To analyze the influence of PLL and VIC on the synchronizing/damping torque offered by DFIG-based WES.
- c) To design a PSS for a synchronous generator under the influence of PLL and VIC dynamics.
- d) Finally, to verify the theoretical analysis of the WES-integrated power systems with time domain simulation.
- 3. Probabilistic modal sensitivity analysis of a large-scale PV-integrated power system:
 - a) Analyzing the uncertainties associated with PV-dominated power systems.
 - b) Evaluating the influence of uncertainties on critical oscillatory modes of the PV-dominated power system.
 - c) To design a VIC-based Battery Energy Storage System (BESS) and its location based on the probabilistic analysis of the uncertainties.
- 4. Evaluate the power system oscillatory modes for the influence of PV-BESS dynamics:
 - a) To develop a small-signal model of a PV-BESS-integrated power system.
 - b) To investigate the influence of PV-BESS dynamics on critical oscillatory mode.
 - c) Finally, to examine the Examine the modal shift of the critical oscillatory modes for uncertain solar irradiance.

1.3 Literature Review

1.3.1 Grid Integration of DFIG-Based WES and its Impact on Power System

In a DFIG-integrated power system, interaction with the grid is primarily influenced by both stator and rotor flux linkages. However, as stator winding is directly exposed to the power system without any intermediary power electronic interface, the stator flux has fast dynamics. Hence, it can be neglected to model the non-linearity of the DFIG [5]. Therefore, rotor flux dynamics are crucial to model grid-integrated DFIG-based WES. Large-scale integration of WES into the power grid introduces transient and small-signal stability issues [8]. A DFIG-based WES

can influence the power system's small signal stability by affecting two major aspects, such as load flow and dynamic interactions with the RPS [9]. According to [10], the DFIG-based WES interacts with the EOL of the synchronous generator through active and reactive power controller dynamics. In addition, it was revealed in [11] that the interaction of converter-based generation with low-frequency EOL depends on the power system's inertia distribution. Further, the dynamic interaction with the power system by DFIGs due to relatively low inertia and inherent variability in power generation may deteriorate the small-signal angular stability of the power system.

The power system with WES integration forms a multivariable, nonlinear coupled network. A wind generator may be decoupled from any power system oscillatory mode as it is coupled with the grid through power converters. However, large-scale wind integration can affect the power system's oscillatory behavior, particularly inter-area modes, as discussed in [12]. Wind power injection at the Point of Common Coupling (PCC) may exert a positive or negative impact on the damping of Electromechanical Oscillatory Modes (EmOM) in the power system [13]. On the other hand, the investigation in [14] claims that the variation of certain system parameters specific to DFIG-based WES also significantly impacts the stability of grid-connected DFIG. The detailed study in [14] involves the derivation of the stability limit of various system parameters such as line reactance, stator impedance, rotor impendence, and wind velocity so that any deviation in such parameters falls beyond the stability limit may deteriorate the operation of the gridconnected wind farm. As a result, careful attention must be given to understanding the damping mechanism of power system oscillations. Research conducted in [15] demonstrates a very interesting phenomenon: the operation under a weak grid scenario, a grid-connected DFIG-based WES induces Sub-Synchronous Oscillations (SSO) in power systems, which are very resonant to PLL oscillations. Recently, in [16], it has been shown that the control parameters of the real and reactive power of PV generation systems significantly affect the damping of electromechanical oscillations.

The damping mechanism offered by WES to low-frequency electromechanical oscillations of power systems has been investigated in three ways [9], [17], [18]. In [9], the WES is a feedback controller whose real and reactive power (P_D, Q_D) output is investigated to influence the damping of EOL of Synchronous Generators (SGs). In [17] a Phillip Heffron model of a multi-machine power system including WES is developed to probe the implication of WES parameters on the

EOL of SGs. Reference [18] has presented a mode-based damping torque method for understanding the damping mechanism offered by the feedback controller. Moreover, in [19], the mutual impact of damping on EmOM and PLL oscillation mode (POM) is demonstrated by the bilateral damping torque analysis method, which is inherited from [9].

On the other hand, [11], [20], [21] have investigated the optimal location for placing a converter-based renewable energy system, which effectively improves the damping performance of the overall system. The work in [20] has proposed a flexibility indexing for all the buses in the system for optimal renewable energy sources (RES) locations. The indexing depends upon system parameters, network topology, and inertial distribution. However, in [11], the location of RES is based on a locational index, which depends on the residue of the concerned electromechanical mode. A mathematical derivation has shown that the residue is a function of the transmission line parameter and inertia of synchronous machines. It has been found that the best location for any RES to be installed is far away from the Center of Inertia (COI).

1.3.2 Stability analysis DFIG-based WES with VIC

Because of their clean, sustainable, and excellent operational characteristics, Wind Energy Systems (WESs) integration in power systems has been rapidly increasing [22]. However, the stochastic nature of WES power output poses many challenges in the secure, reliable, and stable operation of power systems. Several researchers have recently conducted systematic investigations of the dynamic interaction of DFIGs and synchronous generators (SGs) of power systems on an electromechanical time scale [12], [23], [24]. The effects of WES dynamics on the EmOMs of power systems are demonstrated in [12]. References [12] and [25] conclude that DFIG-based wind farms are practically decoupled from power systems, which minimally affect low-frequency EmOMs. However, DFIGs with improper PLL settings may deteriorate the small-signal stability of power systems [24], [26]. According to [27], a high penetration level of type 3/4 wind power generation without a frequency control capacity may decrease frequency response tendencies on the power grid due to a low inertia system. Thus, a WES that uses frequency support technology is critical for enhancing the stability and security of power systems. Previous studies have shown that the frequency control scheme of a WES is accomplished through two methods: frequency droop control and VIC [28]. Many researchers have determined that VIC can provide inertial support with improved System Frequency Regulation (SFR). The frequency support can be

provided by injecting active power [29] or extracting kinetic energy stored in the wind farm [30]. One significant advantage of extracting kinetic energy for frequency stability is that the wind generator does not need to deviate from the Maximal Power Point Tracking (MPPT) during normal operation (i.e., the derated operation is avoided), and results in reduced energy waste [31]. According to [32], increased wind penetration can adversely affect low-frequency EmOMs. Furthermore, [32] concludes that the inertial response from the WES protects the system from stability loss and improves the damping of inter-area system modes. A key performance indicator is proposed in [33] to understand the frequency stability limit of wind generators in power system planning studies. Under severe contingency conditions, extraction of kinetic energy by conventional VIC reduces the efficiency of variable-speed wind generators. This issue has been resolved by proposing an adaptive VIC [34].

Reference [35] proposes an adaptive virtual capacitor to provide inertial support. Later, [36] develops an optimal auxiliary frequency controller containing a droop controller for WTGs operating at MPPT for improved SFR. As part of the work in [8], the kinetic energy from an SG and locally installed DFIG is shared to improve the transient and dynamic stability of the power system. In [37], an optimized proportional-integral-derivative controller is proposed to improve the performance of VIC to achieve better frequency stability. References [38] and [39] investigate power system stability regarding energy dissipation under the combined influence of a PLL and VIC. The studies have found that with a higher virtual inertial gain, the possibility that the energy dissipation may cause power system instability will be greater. Further, [39] explicitly shows that a WES with a PLL and VIC participates significantly in the low-frequency EmOMs of the power system. Therefore, careful cooperation in the design of the PLL is required for wind systems that include a PLL and VIC, as improved power angle stability in the power system can then be achieved.

1.3.3 Oscillatory Stability Analysis of SPV-Integrated Power System

The power grid is rapidly evolving with more participation of power electronically interfaced sources like solar, wind, BESS, etc., leading to increased uncertainties and reduced inertia [40], [41]. In addition, the power system also witnesses uncertainties due to the deregulation of the energy market and load variations [42]. The uncertainties from renewable sources make the power system complex and encounter critical challenges in terms of swift response to the change

in system frequency and damping to the electromechanical oscillations. The increased penetrations from renewable sources critically challenge the frequency and dynamic stability of power systems. Therefore, increased penetration of renewables attracts careful attention to the study of uncertainties.

As the integration of inverter-based energy resources is anticipated to grow in the future grid, the research articles from [39], [43], and [44] have proposed various technologies for virtual inertia mode control of converter operations. In the context of PV operation, the approach suggested in [43] involves introducing a derated mode to enhance the PV's responsiveness to frequency excursion events. However, a different perspective is presented in the articles [44] - [45]. The articles introduced the involvement of charging and discharging of DC link capacitors to provide virtual inertia support to solar PV systems. In [45], an active power controller-based virtual synchronous controller is proposed for DFIG-based wind systems. Most of the virtual inertia controller methods in the existing literature are based on a deterministic approach.

Conventional deterministic approaches, based on fixed and known parameters, may not be effective in an intermittent power system. Hence, to address the challenging issue of the stochastic characteristic of the power system, many authors have contributed their research in the development of the stochastic dynamic model of wind or PV systems [46], [47], [48], adaptive damping controller design using uncertainties [49], [50] online inertia estimation of power system [51], [52]. In this context, the articles [47], [53], and [54] have formulated the power generations from solar and wind systems based on modeling natural characteristics of solar irradiation and wind velocity with Gaussian/Beta distribution and Weibull distribution, respectively. As a result, stochastic models for these sources are widely employed to conduct crucial studies, including probabilistic steady-state analysis of power systems [55] and stochastic eigenvalue analysis for future grid scenarios [53], [47]. Power penetrations from stochastic-based renewable sources alter the system inertia and, with disturbances, may lead to system instability [56]. Hence, in literature like [57], [53], [58], the study of change in system inertia from the prospect of small signal stability due to large-scale integration of stochastic sources is performed using various probabilistic approaches such as Monte Carlo Simulation, Gram-Charlier expansion, or Polynomial Chaos expansion.

Global Sensitivity Analysis Tools (GSATs) are employed to identify the most impactful parameters among extensive sets of uncertain inputs. Limited applications of GSATs in power systems are currently limited to areas like the ranking of bus [59], design of Power System Stabilizer (PSS) [60], voltage stability [61], and transient stability [62]. However, the applications of Global Sensitivity Analysis (GSA) are found most in the field, like financial decisions [63], acoustic energy modeling [64], environmental models [65], public deliveries [66], and medical science [67]. In the literature survey, the application of GSATs in small signal stability assessment of power systems is limited except in some publications like [68], [69], [61]. Research works in [68] and [69], analyze the uncertainties of the modern power system using various GSATs to recognize the most influential parameters affecting frequency stability and small signal stability of the power system.

1.3.4 Impact of SPV with VIC on stability of power system

Solar PV power plants, wind energy systems, and other renewable energy sources are becoming more and more prevalent due to decarbonization and a lack of energy from conventional sources. The penetration from renewable sources has steadily expanded in past decades and is also anticipated to grow rapidly [70]. In a practical scenario, the participation of PV systems in meeting the energy demand from clean and sustainable sources is very significant. Moreover, replacing synchronous generators with equal-rating PV power plants encounters some critical challenges, such as quick response to system frequency change and damping to electromechanical oscillations [71]. Therefore, large-scale PV integration into the power grid needs thorough investigation to realize the impact of PV systems on the dynamics of the RPS.

In recent decades, the PV system has been enabled with various means of VIC to provide frequency support as described in [72], [44], [73]. PV systems operated in derated mode utilize reserved power, which is the difference between maximum power generation capacity (i.e., power at MPPT) and operating power to adjust the generation in response to frequency excursion events [72]. The major demerit of this control mechanism is that it would result in economic loss. Reference [44] has introduced the charging and discharging of DC link capacitors to provide virtual inertia to solar PV systems. In this technology, the terminal voltage reference of the DC link voltage controller varies according to the change in system frequency. As discussed in [73], the virtual inertia control strategy used in the BESS in PV power plants modifies BESS reference

power to provide additional support for system frequency variation while smoothing the fluctuation of PV power output. BESS's State-of-Charge (SOC) is very important when offering frequency support. The finding of [74] aims to propose an adaptive SOC recovery strategy for BESS to deliver under-frequency support. In the scenario of increasing PV penetration into existing power systems, it is essential to study the power system oscillatory modes before and after the placement of PV systems. It is noticed in [75] that the PV systems enabled with virtual inertia controller provide inertial support and dampen power system oscillation by creating a new oscillatory mode. Damping of such oscillatory modes is also crucial to maintaining power system stability. Recently, in [76], an adaptive wide-area damping control strategy is proposed for a PV-integrated power system. However, the control mechanism does not consider the uncertainty associated with PV output power, and the PV system was not capable of any change in grid side frequency. In [77], a BESS is modeled to dampen a target oscillation mode for a power system, but it does not consider any renewable source in the power system.

1.4 Contribution Overview

The primary focus of the research contribution in this thesis involves investigating the impact of grid-connected WES or SPV on the EOL of the rest of the power system. The dynamic stability of the renewable-integrated power system is basically dictated by the strength of damping/synchronizing torque afforded by the EOL of the synchronous generator, which is significantly affected by the grid-interacted renewable-based energy systems. The key contributions of the thesis in this regard are:

- a) Extensive literature surveys addressing various problems affecting the damping of power system oscillatory modes or affecting the small signal angular stability of the power system are thoroughly presented in the research.
- b) A unique methodology is proposed to evaluate the impact of various system parameters on the damping torque offered by DFIG-based WES to the EOL of the RPS.
- c) A new PSS design method for a power system with a DFIG-based wind farm enabled with VIC and PLL has been proposed.
- d) Probabilistic small signal stability of power systems consisting of large-scale SPVs is performed considering various parameters and their uncertainties.

e) Ranking of all the generator buses of a power system is obtained by probabilistic modal sensitivity analysis based on different Sensitivity Analysis (SA) tools like Sobol, Random Balance Designs - Fourier Amplitude Sensitivity Test (RBD-FAST), Delta Moment-Independent Measure (DMIM), and Pianosi and Wagener (PAWN) on the power system by replacing each generator with a similarly rated SPV under the uncertainties of load variations and generator output.

1.5 Structure of the Thesis

Chapter 1: State-of-the-Art

This chapter introduces the motivation behind the research undertaken in this thesis, exploring the necessity of addressing climate change. It has provided the recent development of energy transition of modern power systems from various renewable sources. The chapter also discusses an overview of the technology used to harness the energy from wind and solar. Further, the chapter outlines the key contribution of the research, followed by the structure of the thesis.

Chapter 2: Investigation of Damping Torque Offered by DFIG to the EOL of RPS for Influence of Various System Parameters

The chapter presents a simplified mathematical formulation for analyzing the impact of system parameters on the damping of interarea oscillations. A simple power system model consisting of two synchronous machines and a DFIG has been considered for mathematical derivations. The derived mathematical formulation has been validated for a higher-order power system integrated with WES. The derived expression of damping contribution to synchronous machines supports the concept that damping is highly dependent on transmission line reactance. This further supports the idea that WES placement in the power system is crucial in improving damping contribution to synchronous machines.

Chapter 3: Small Signal Stability Analysis of DFIG-based Wind Energy-Integrated Power Systems Under Combined Influence of PLL and Virtual Inertia Controller

WESs based on DFIGs have enormous potential for meeting the future demands related to clean energy. Integration of WES challenges the stability of power systems due to low inertia and intermittent power injection offered by DFIGs. The research of this chapter proposes mathematical formulations to compute synchronizing and damping torque coefficients of a WES-integrated Single-Machine Infinite Bus (SMIB) system while considering PLL and VIC dynamics. In addition, a PSS is designed for a wind energy-integrated power system to enhance electromechanical oscillation damping. The proposed research methodology is tested in an SMIB and nine-bus test systems integrated with WES under several case studies.

Chapter 4: Probabilistic Modal Sensitivity Analysis of Large-Scale PV-Integrated Power System

This chapter evaluates the ranking of the generator bus by replacing each generator at a time with a similar rating of the SPV system, considering the various uncertain parameters like the probabilistic output of SPV, uncertainties of generator output, and load demand. The ranking of the buses is compared by widely used popular numerical sensitivity analysis (SA) techniques such as Sobol, RBD-FAST, DMIM, and PAWN. Then, the inertial distribution among all the busses is investigated to find a suitable bus for BESS installation. The BESS in this research is considered with a virtual inertia controller. The PSS to be installed with the synchronous generators is identified by the Sensitive PSS Effect (SPE). The VIC gain and PSS parameters are tuned simultaneously by the PSO optimization method.

Chapter 5: Evaluation of Power System Oscillatory Modes for the Influence of PV-BESS Dynamics

The increase of power electronically interfaced PV power plants into power systems causes severe stability problems due to lack of inertia and damping effect. The BESS at PV stations can be controlled by a VIC to provide virtual inertia and damping support while smoothing the power fluctuations of the PV power plant. The research of this chapter investigates the probabilistic distribution of power systems' Low-frequency Electromechanical Oscillations (LEOs) for various controller gains of VIC and stochastic variation of solar irradiance under the influence of PLL dynamics. Using the Monte Carlo simulation approach, the modal interaction of PLL and VIC with power system oscillatory modes is investigated by stochastic eigenvalue analysis.

Chapter 6: Conclusion and Future Research

The summary of the main research findings from the thesis work is unveiled in conclusion. This chapter also provides the insights of future research domains.

Appendix A: Derivation and System Data

The appendix provides some mathematical derivations and system data that support Chapter 2 to Chapter 5 of the thesis.

Appendix B: List of Publication

The appendix contains the list of publications resulting from the research work conducted during the Ph.D. program.

Chapter 2

Investigation of Damping Torque Offered by DFIG to the EOL of RPS for Influence of Various System Parameters

The chapter presents an analytical formulation for analyzing the impact of system parameters on the damping of interarea oscillations. A simple power system model consisting of two synchronous machines and a Doubly-Fed Induction Generator (DFIG) has been considered for mathematical derivations. The derived mathematical formulation has been validated for a higher-order power system integrated with the Wind Energy System (WES). The derived expression of damping contribution to synchronous machines supports the concept that damping is highly dependent on transmission line reactance. This further supports the idea that WES placement in the power system is crucial in improving damping contribution to synchronous machines.

2.1 Introduction

As mentioned in Chapter 1, the low inertia and intermittency of Doubly-Fed Induction Generator-based (DFIG-based) wind farms significantly influence the dynamic interaction with the power system, which can potentially jeopardize the small signal stability of the complete system. The integration of DFIG with the power system impacts the steady state and dynamic performance of the system [13]. As per the literature survey presented in Chapter 1, the real and reactive power output from DFIG-based Wind Energy System (WES) can impose a direct impact on the damping of the Electromechanical Oscillation Loop (EOL) of the synchronous generator [9], [17]. Further, it can be observed that the various control parameters of the inner/outer loop controller of real/reactive power also substantially impact the damping of the electromechanical mode of interest [16]. Moreover, the location of WES also plays a significant role in the stability of the system.

The major contribution of the proposed research work in this chapter includes further investigation of the small-signal stability of the DFIG-integrated power system impacted by the variation of the various system parameters like transmission line reactance, bus, voltage, and inertia of synchronous machine. The main objective of the proposed work is to assert the existing research gap by contributing the following points:

- 1) A mathematical formulation of damping torque influenced by DFIG-based WES to the electromechanical oscillation is presented by considering the impact of variation of several system parameters such as line reactance, bus voltage, and machine inertia. To the best of the authors' knowledge, this comprehensive analysis is unique and includes the impact of system parameters on the damping effect produced by the DFIG system.
- 2) To realize the damping torque explicitly by an analytical mathematical expression, a reduced-order DFIG-based WES model has been developed by using Cross-Gramian and SVD methods [78]. The mathematical expression defines the impact of variation in parameters of the system mentioned above on damping contribution from DFIG to the Rest of the Power Systems (RPS) as a function of transmission line reactance, bus voltage, and machine inertia.
- 3) Finally, a systematic analysis of the expressions obtained with respect to the different values of system parameters was carried out. The main aim is to realize the positive or negative effect of the change in parameters on the damping torque influenced by the DFIG system on the electromechanical oscillation loop of the RPS.

The derived expression of damping contribution to synchronous machines supports the concept that damping is highly influenced by transmission line reactance. This further supports the idea that WES placement in the power system has a crucial role in improving the damping contribution of synchronous machines. The conceptual derivation is also validated on the IEEE 39 bus test system.

2.2 Impact of System Parameter on Damping of Low-Frequency Inter-Area Mode

This section presents a comprehensive analysis of mathematical expressions for damping torque contribution to the EOL of synchronous machines by system parameters.

2.2.1 Open Loop State Space Model of Power System

To derive the expression for damping torque provided by WES to EOL of synchronous machines affected by system parameters, a simple lossless line, as shown in Figure 2.1, is considered. A synchronous generator (M1) and synchronous motor (M2) are connected at bus nos. 1 and 2, respectively. Both the synchronous machines are represented by the classical model, i.e.,

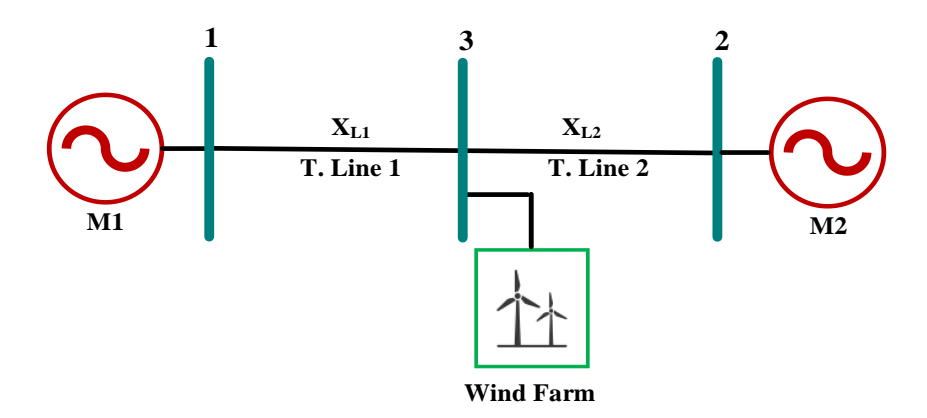


Figure 2.1 Two-machine system with wind farm at bus 3

it is represented by an internal transient voltage E'_i is in series with d-axis transient reactance X'_{di} . The wind farm is aggregated into a single DFIG and connected to bus 3. The transmission lines are considered lossless and represented only as series reactance. The reactance of the line connecting buses 1-3 and 2-3 is represented by X_{L1} , and X_{L2} respectively. The non-linear dynamic states of the synchronous machines are expressed by the following differential equations [79]

$$\begin{cases} \delta_{1} = \omega_{s} - \omega_{1} \\ \delta_{2} = \omega_{s} - \omega_{2} \\ \omega_{1} = \frac{1}{m_{1}} \left(P_{m1} - \frac{E'_{1}V_{3}}{X_{13}} sin(\delta_{1} - \theta_{3}) \right) \\ \omega_{2} = \frac{1}{m_{2}} \left(\frac{E'_{2}V_{3}}{X_{23}} sin(\theta_{3} - \delta_{2}) - P_{m2} \right) \end{cases}$$
(2.1)

where i=1,2 indicates the number of synchronous machines, $X_{13}=X_{L1}+X'_{d1}$, $X_{23}=X_{L2}+X'_{d2}$. All parameters used in (2.1) are all presented per unit except the angular velocity ω_s and ω_i whose unit is in radians per second, δ_i in radian and m_i is evaluated by $\frac{2*H_i}{\omega_s}$. Here H is the inertia constant of synchronous machines in seconds. The angle differences are assumed to be small enough such that, $\sin(\delta_i-\theta_3)\approx(\delta_i-\theta_3)$ and $\cos(\delta_i-\theta_3)\approx1$. The DFIG-based WES is connected to bus 3 and is assumed to inject only active power. The reactive power exchange by WES is assumed to be zero. For the load flow studies, the power generation from WES is assumed to be constant, i.e., $\Delta P_D=0$, as can be seen from the equations (2.2) and (2.3). With the inclusion of WES at bus 3, the relationship between bus voltage $(V_3 \angle \theta_3)$ with state variables are given by:

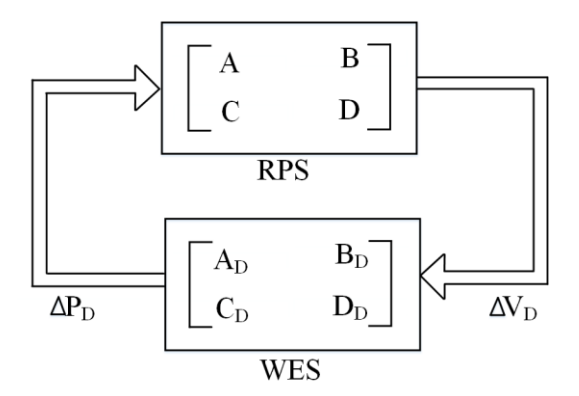


Figure 2.2 Control loop between RPS and WES

$$S_3 = V_3 e^{j\theta_3} conj \left(\frac{V_3 e^{j\theta_3} - E_1' e^{j\delta_1}}{jX_{13}} + \frac{V_3 e^{j\theta_3} - E_2' e^{j\delta_2}}{jX_{23}} \right)$$
(2.2)

By taking real and imaginary parts of (2.2), the following two equations are obtained:

$$\begin{cases} P_3 = \frac{V_3 E_1'}{X_{13}} (\theta_3 - \delta_1) + \frac{V_3 E_2'}{X_{23}} (\theta_3 - \delta_2) \\ Q_3 = \frac{V_3^2}{X_{13}} + \frac{V_3^2}{X_{23}} - \frac{V_3 E_1'}{X_{13}} - \frac{V_3 E_1'}{X_{13}} \end{cases}$$
(2.3)

In (2.3), as per the mentioned assumptions, $P_3 = P_D$, and $Q_3 = Q_D = 0$. Now, to develop an analytical expression of damping torques for defining the dynamic interaction between the WES and RPS, the system has been partitioned as a feedback system, as shown in Figure 2.2. The Differential and Algebraic Equations (DAEs) model of the open-loop power system is formulated by only considering the synchronous machines and is given in (2.1) and (2.3). The initial machine states are obtained from power flow solutions and are assumed to be equilibrium points. The nonlinear differential equations of (2.1) and algebraic equations of (2.3) are linearized around the equilibrium point with state vectors $x = [\delta_1, \delta_2, \omega_1, \omega_2]$ and algebraic variable V_3 , the linearized state-space model of the open-loop power system (i.e., RPS) can be expressed as:

$$\begin{cases}
\dot{\Delta x} = A_1 \Delta x + B_1 \Delta V_3 \\
\Delta P_D = C_1 \Delta x + D_1 \Delta V_3
\end{cases}$$
(2.4)

To model the RPS with a change in power at bus 3 (ΔP_D) as input variable and change in voltage magnitude at bus 3 (ΔV_3) as output variable, (2.4) is augmented to:

$$\begin{cases} \dot{\Delta x} = A\Delta x + B\Delta P_D \\ \Delta V_3 = C\Delta x + D\Delta P_D \end{cases}$$
 (2.5)

where

$$A = A_1 - B_1 D_1^{-1} C_1 = \begin{bmatrix} 0 & 0 & 1 & 0 \\ 0 & 0 & 0 & 1 \\ \frac{-n_1 E_2' V_3}{E_1' X_{23} + E_2' X_{13}} & \frac{n_1 E_2' V_3}{E_1' X_{23} + E_2' X_{13}} & 0 & 0 \\ \frac{n_2 E_1' V_3}{E_1' X_{23} + E_2' X_{13}} & \frac{-n_2 E_1' V_3}{E_1' X_{23} + E_2' X_{13}} & 0 & 0 \end{bmatrix}$$

$$B = B_1 D_1^{-1} = \begin{bmatrix} 0 & 0 & \frac{X_{23}n_1}{E_1'X_{23} + E_2'X_{13}} & \frac{X_{13}n_2}{E_1'X_{23} + E_2'X_{13}} \end{bmatrix}^T$$

$$C = -D_1^{-1}C_1 = \frac{E_1'E_2'X_{13}X_{23}}{[E_1'X_{23} + E_2'X_{13}]X}[(\delta_2 - \delta_1) \quad (\delta_1 - \delta_2) \quad 0 \quad 0]$$

$$D = D_1^{-1} = \frac{-X_{13}X_{23}[E_1'X_{23}(\theta_3 - \delta_1) + E_2'X_{13}(\theta_3 - \delta_2)]}{V_3[E_1'X_{23} + E_2'X_{13}]X}$$

$$X = X_{23} + X_{13}, n_1 = \frac{E_1'}{m_1}, n_2 = \frac{E_2'}{m_2}$$

Here the voltages $E'_1 \angle \delta_1$, $E'_2 \angle \delta_2$, $V_3 \angle \theta_3$ are of buses 1, 2, and 3, respectively, and are evaluated at an operating point. The matrices A, B, C, and D are system state matrices, input coefficient vectors, output coefficient vectors, and feedforward matrices between changes in voltage magnitude at bus 3 (ΔV_3) and change in power at bus 3 (ΔP_D). The mathematical expression for electromechanical eigenvalue is obtained from the system state matrix given by,

$$\lambda_{1,2} = \pm j\omega = \pm j \sqrt{\frac{E_1' E_2' V_3 (m_1 + m_2)}{M_1 M_2 (E_1' X_{23} + E_2' X_{13})}}$$
(2.6)

Beyond this point, the eigenvalue is notified by λ instead $\lambda_{1,2}$. Let the right eigenvector be expressed by $v = [e \ f \ g \ h]^T$. Hence, the analytical value for the elements of the right eigenvector can be evaluated by:

$$Av = \lambda v \tag{2.7}$$

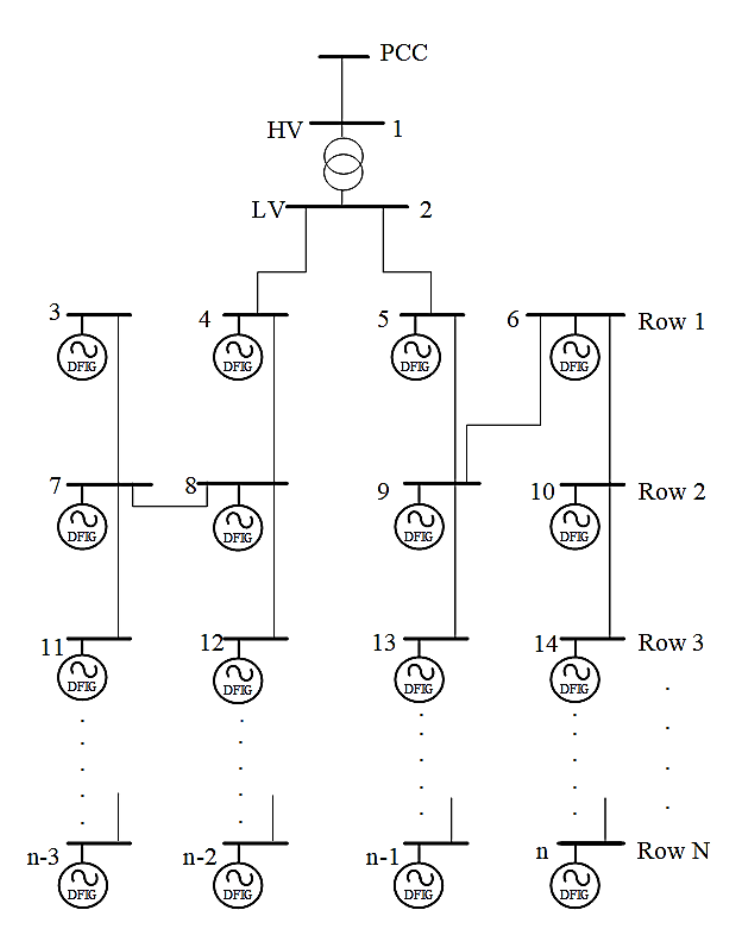


Figure 2.3 Wind generators in a wind farm

$$v = [-n_1 E_2'/\lambda \quad n_2 E_1'/\lambda \quad -n_1 E_2' \quad n_2 E_1']^T$$
(2.8)

For verification purposes, it can be noted here that the mode shape of rotor angle velocities for M1 and M2 is exactly 180^o to each other.

2.2.2 Close loop model of RPS with DFIG-based wind farm

In this research, the wind farm, consisting of 30 numbers of DFIG-based Wind Turbine and Generator Systems (WTGS), has been aggregated into a single system. The prime focus of the research, is to obtain the influence of the various parameters of the rest of the power system on the damping contribution of the DFIG to the EOL of the synchronous machines. Certainly, as the chapter does not consider the study of varying wind effect and varying cable impedance within the wind farm on the evaluation of damping torque contribution to the EOL of RPS, the chapter considers a basic wind farm that assumes the wind velocity across the entire farm remains uniform,

all machines within the farm have identical ratings and interconnected parallelly with each other, as shown in Figure 2.3. All the wind generators are placed in a distributed manner. The detailed modeling of each generator may be unaffordable due to the computational burden. Hence, to reduce the computational dimensionality, the whole wind farm has been aggregated into a single DFIG generator. According to the aggregation concept [80], the total input mechanical torque of the wind farm is defined as:

$$T_{mD}^{e} = \sum_{i=1}^{n} \frac{1}{2} B \omega_{s} C_{p}^{i} \frac{V_{w}^{i^{3}}}{\omega_{rD}}$$
 (2.9)

where B, C_p , and V_w are torque parameter $\left(\frac{pu\,s^3}{m^3}\right)$, power coefficient of the wind turbine, and wind velocity (m/s), respectively. The chapter evaluates how various system parameters influence the damping contribution offered by the DFIG to the EOL of synchronous machines. Thus, in this research, the wind speed is treated as the average of the various wind speeds. Therefore, this research assumes that the wind velocity and, thus, wind power output is constant. The equivalent electrical power output of the overall wind generator of the wind farm is:

$$P_{D,e} = \sum_{i=1}^{n} P_{Di} | n \in \text{ no. of wind generators}$$
 (2.10)

Similarly, the equivalent reference power of overall wind generators corresponds to active power:

$$P_{D,e}^* = \sum_{i=1}^n P_{D,i}^* = C \sum_{i=1}^n \omega_{rD}^{i}^3$$
 (2.11)

The equivalent stator and rotor current are as follows:

$$I_{dsD}^{e} = \sum_{i=1}^{n} I_{dsD}^{i} \quad I_{qsD}^{e} = \sum_{i=1}^{n} I_{qsD}^{i}$$

$$I_{drD}^{e} = \sum_{i=1}^{n} I_{drD}^{i} \quad I_{qrD}^{e} = \sum_{i=1}^{n} I_{qrD}^{i}$$
(2.12)

where I_{dsD} , and I_{qsD} are DFIG stator current on the d-q axis and I_{drD} , and I_{qrD} are DFIG rotor current on the d-q axis. In equations given by (2.17) and (2.18), the equivalent d-q axis rotor

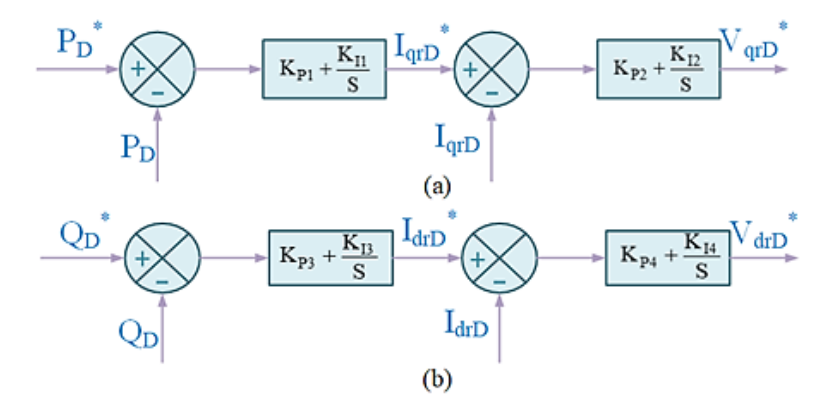


Figure 2.4 Rotor Side Converter Controllers: (a) Active power controller (b) Reactive power controller voltages, such as V_{drD}^{e*} and V_{qrD}^{e*} are of the same magnitude as an individual wind generator. Thus, the equivalent control parameters are:

$$K_{P2}^{e} = \frac{K_{P2}}{n} \quad K_{I2}^{e} = \frac{K_{I2}}{n}$$

$$K_{P4}^{e} = \frac{K_{P4}}{n} \quad K_{I4}^{e} = \frac{K_{I4}}{n}$$
(2.13)

As per the above modeling of the distributed wind-turbine systems, the damping contribution by the wind farm can be proportionately shared by each generator wind-turbine unit with respect to

their ratings. However, a detailed study is needed for damping torque analysis, which is outside the scope of this work.

The wind turbine gearbox dynamics and active and reactive power controllers are only considered for modeling DFIG-based WES. The dynamics of stator and rotor flux linkages are ignored, which is supported by the fact that the time constant of the rotor and stator flux linkage is much smaller than the rest of the dynamics, i.e., dynamics of wind turbine gearbox, active and reactive power controller [80]. The wind turbine gearbox is assumed to be stiff and, hence, modeled as a single mass drive system. The single mass model of the DFIG considers the dynamics of only one rotating mass and thus reduces the complexity of the mathematical analysis. As the chapter focuses on how various system parameters influence the damping contribution offered by the DFIG to the EOL of synchronous machines, the consideration of a single mass model of DFIG does not affect the accuracy. The dynamics of a single mass drive system are represented by:

$$\frac{d\omega_{rD}}{dt} = \frac{\omega_s}{2H_D} \left[T_{mD} - X_{mD} I_{qsD} I_{drD} + X_{mD} I_{dsD} I_{qrD} \right]$$
(2.14)

where X_{mD} , is magnetizing reactance, $I_{qsD} - jI_{dsD}$ and $I_{qrD} - jI_{drD}$ are stator and rotor currents, respectively, on d-q frame, T_{mD} is the mechanical torque input of a WTG is a function of wind velocity ω_r . The research of this chapter examines the influence of the DFIG-based wind energy system (WES) on the electro-mechanical oscillation loop (EOL) of the rest of the power system (RPS), taking into account the non-linearities of DFIG, including its controllers. The dynamics of the rotor side converter controller regulate active and reactive power output, playing a crucial role in how DFIG contributes damping to the EOL of the RPS through its real and reactive power control loops. The RSC dynamics control consists of the active and reactive power generation control of DFIG [24]. From Figure 2.4, the outer loop power control equations can be represented by:

$$\begin{cases} I_{qrD}^* = (P_g^* - P_g) \left(K_{P1} + \frac{K_{I1}}{s} \right) \\ I_{drD}^* = (Q_g^* - Q_g) \left(K_{P3} + \frac{K_{I3}}{s} \right) \end{cases}$$
(2.15)

Here, P_g and Q_g refer to total active and reactive power injected by wind energy systems (WES). Please note that, " * " is used for the reference signal. Considering the q-axis is aligned with the stator flux axis (i.e., $V_{qsD} = V_D = V_3$. and $V_{dsD} = 0$). The total active and reactive power penetrated by WES are as follows:

$$\begin{cases}
P_g = V_{qSD}I_{qSD} - (V_{qrD}I_{qrD} + V_{drD}I_{drD}) \\
Q_g = V_{qSD}I_{dSD}
\end{cases}$$
(2.16)

where $V_{qsD} - jV_{dsD}$ and $V_{qrD} - jV_{drD}$ are stator and rotor voltage on d - q reference frame. By ignoring the impact of the feedforward rotor voltage compensation term, the inner loop current control equations can be written as [80]:

$$\begin{cases} V_{qrD}^* = \left(I_{qrD}^* - I_{qrD}\right) \left(K_{P2} + \frac{K_{I2}}{s}\right) \\ V_{drD}^* = \left(I_{drD}^* - I_{drD}\right) \left(K_{P4} + \frac{K_{I4}}{s}\right) \end{cases}$$
(2.17)

The relationship between stator and rotor current can be stated as follows [81]:

$$\begin{cases} I_{drD} = \frac{1}{X_{mD}} \left(V_D + R_{sD} I_{qsD} + X_{sD} I_{dsD} \right) \\ I_{qrD} = \frac{1}{X_{mD}} \left(-R_{sD} I_{dsD} + X_{sD} I_{qsD} \right) \end{cases}$$
(2.18)

where $R_{SD} + jX_{SD}$ is the stator impedance of DFIG. Similarly, the interdependence between stator current and rotor parameters can be obtained by:

$$\begin{cases} I_{dsD} = \frac{1}{sX_{mD}} \left(R_{rD} I_{qrD} + sX_{rD} I_{drD} - V_{qrD} \right) \\ I_{qsD} = \frac{1}{sX_{mD}} \left(-R_{rD} I_{drD} + sX_{rD} I_{qrD} - V_{drD} \right) \end{cases}$$
(2.19)

The DFIG-based WES combined model described in (2.14) - (2.19) is fifth-order dynamics. Now, considering state variables $x_D = \{\omega_{rD}, x_1, x_2, x_3, x_4\}$, input variable V_D and output variable as, $P_D = P_g$ the full-order linear state equation is as follows:

$$\begin{cases}
\Delta \dot{x}_D = A_D \Delta x_D + B_D \Delta V_D \\
\Delta P_D = C_D \Delta x_D + D_D \Delta V_D
\end{cases}$$
(2.20)

Algorithm 1 Model order reduction of DFIG-based wind farm by Cross-Gramian and SVD method [78]

Input: Original 5th-order model of DFIG-based WES

Solve the Sylvester equation $A_DW_x + W_xA_D + B_DC_D = 0$ for W_x .

1: (where $W_x = \int_0^\infty e^{A_D t} B_D C_D e^{A_D t} dt | W_x$:crossGramian)

Compute the right and left eigenvectors of W_x such that

2: $W_x = U_R \wedge U_L^T$, where \wedge is a diagonal matrix

Rearrange U_R and U_L in the following manner

3: $U_R = \begin{bmatrix} U_R^{large} & U_R^{Small} \end{bmatrix}^T, U_L^T = \begin{bmatrix} U_L^{large} & U_L^{Small} \end{bmatrix}$

4: Obtain M_{big} and apply SVD as:

$$M_{big} = U_{L,large}^{T} U_{R,large} = U_{large} \Sigma_{large} V_{large}^{T}$$

- 5: Compute $C_R = U_R^{large} V_{large} \Sigma_{large}^{-0.5}$ and $C_L^T = U_L^{large} U_{large} \Sigma_{large}^{-0.5}$.
- **6:** Evaluate reduced coefficient matrices as $A_r = C_L^T A_D C_R$, $B_r = C_L^T B_D$, $C_r = C_D C_R$

Output: The coefficient matrices of the reduced DFIG-based WES model are obtained.

The detailed procedure adopted to form a state-space model of the DFIG-based WES is provided in Appendix A. 1. To simplify the analysis, the farm has been reduced to a single-order model using Cross-Gramian and SVD methods [78]. The algorithm of the model-order reduction by the Cross-Gramian and SVD method is given in Algorithm 1. The advantage of the reduction method is that it reduces the original system based on eigenspace associated with the largest eigenvalue of the Cross-Gramian , which means that the original system is reduced to a system with only the highest energy state. Moreover, the reduction method reduces the computational burden without compromising the results. The data of each wind turbine and synchronous generator are provided in Appendix A. 3. Figure 2.5 shows the comparison of the magnitude plot of the original and reduced model of WES. The original system is a 5th-order model of DFIG-based WTGs. The reduced system accurately follows the original system for frequencies 0.5 rad/sec. (≈ 0.1 Hz) and

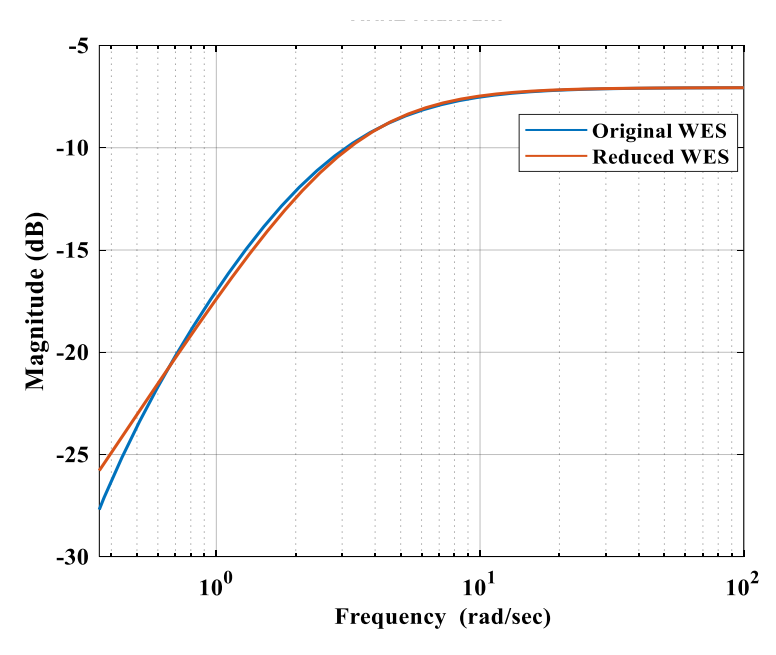


Figure 2.5 Magnitude plot of DFIG-based WES

above. As the low-frequency Electromechanical Oscillatory Modes (EmOM) of the power system generally lie in the range of 0.3 Hz to 3 Hz (\approx 20 rad/sec), the reduced-order WES can be considered for further analysis. After reduction, the linearized open-loop state-space model of DFIG-based WES can be defined as:

$$\begin{cases} \Delta \dot{x}_r = A_r \Delta x_r + B_r \Delta V_D \\ \Delta P_D = C_r \Delta x_r + D_r \Delta V_D \end{cases}$$
 (2.21)

Here, the size of the WES state matrix is A_r , input co-efficient vector B_r , output co-efficient vector C_r and the input/output coupling matrix D_r are $[1 \times 1]$ each. From (2.21), the transfer function of DFIG can be obtained as:

$$\frac{\Delta P_D}{\Delta V_D} = C_r (sI - A_r)^{-1} B_r + D_r = H_{DP}(s)$$
 (2.22)

where *I* is an identity matrix. To obtain the closed-loop interconnection between RPS and DFIG-based WES, the RPS linearized model, defined in (2.5), can be rewritten as:

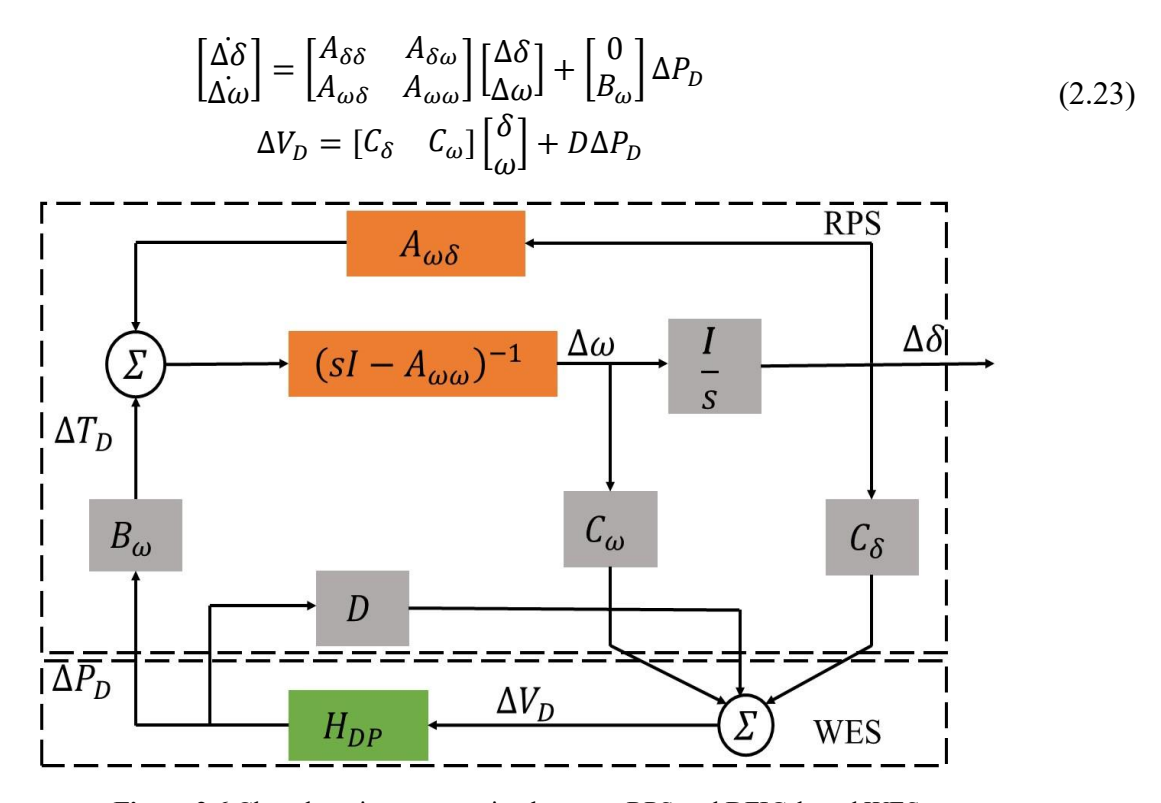


Figure 2.6 Close-loop interconnection between RPS and DFIG-based WES

Here, $\Delta \delta = \{\Delta \delta_1 \ \Delta \delta_2\}^T$, $\Delta \omega = \{\Delta \omega_1 \ \Delta \omega_2\}^T$. From (2.22) and (2.23), the close-loop linearized model of RPS, including DFIG-based WES, is shown in Figure 2.6. In Figure 2.6, ΔT_D represents torque contribution from DFIG to the electromechanical loop of synchronous machines. From this figure, the ΔT_D can be defined by:

$$\Delta T_D = B_\omega H_{DP}(s) \Delta V_D \tag{2.24}$$

From (2.22) and (2.23) ΔV_D can be expressed as

$$\Delta V_D = \frac{[C_\delta \quad C_w] \Delta x}{1 - DH_{DP}(s)} \tag{2.25}$$

Here, Δx is the solution of (2.23) and can be expressed as:

$$\Delta x = \frac{vz}{s - \lambda}, \qquad \Delta \omega_j = \frac{v_{\omega j} z}{s - \lambda}$$
 (2.26)

where $j=1,2,\ v$ is the right eigenvector associated with λ and $z=u\Delta x(0)$, where u is the left eigenvector of λ , $v_{\omega 1}$ and $v_{\omega 2}$ are the entries of v corresponding to $\Delta\omega_1$ and $\Delta\omega_2$. From (2.25) and (2.26), the relationship of ΔV_D with $\Delta\omega_1$ and $\Delta\omega_2$ can be expressed as:

$$\Delta V_D = \frac{[C_\delta \quad C_w]v}{(1 - DH_{DP}(s))v_{\omega i}} \Delta \omega_i, \quad i = 1, 2$$
(2.27)

Now, for the given eigenvalue λ , (2.24) can be rewritten as:

$$\Delta T_{Di} = \frac{B_{\omega i} H_{DP}(\lambda) [C_{\delta} \quad C_{w}] v}{(1 - DH_{DP}(\lambda)) v_{\omega i}} \Delta \omega_{i}, \quad i = 1, 2$$
(2.28)

where $B_{\omega i}$ are the entries of the vector B_{ω} corresponding to $\Delta \omega_i$. Now, the damping torque provided by DFIG can be expressed by:

$$D_{\omega i} = Re(\Delta T_{Di}/\Delta \omega_i), \quad i = 1,2 \tag{2.29}$$

2.2.3 Derivation of $D_{\omega 1}$ and $D_{\omega 2}$

The DFIG transfer function defined in (2.22) can be represented as follows:

$$H_{DP}(s) = D_r + \frac{C_r B_r}{sI - A_r}$$
 (2.30)

where $s = j\omega$. ω is the frequency of oscillation of electromechanical inter-area mode, λ . Using $s = j\omega$ in (2.30)

$$H_{DP}(\omega) = \frac{D_r (A_r^2 + \omega^2) - B_r C_r A_r}{A_r^2 + \omega^2} - j \frac{B_r C_r \omega}{A_r^2 + \omega^2}$$
(2.31)

Using (2.31) in (2.29), the $D_{\omega i}$ can further be elaborated as

$$D_{\omega i} = Re \left(\frac{B_{\omega i} \left(\frac{D_r (A_r^2 + \omega^2) - B_r C_r A_r}{A_r^2 + \omega^2} - j \frac{B_r C_r \omega}{A_r^2 + \omega^2} \right) [C_\delta \quad C_w] v}{\left(1 - D \left(\frac{D_r (A_r^2 + \omega^2) - B_r C_r A_r}{A_r^2 + \omega^2} - j \frac{B_r C_r \omega}{A_r^2 + \omega^2} \right) \right) v_{\omega i}} \right)$$
(2.32)

The $D_{\omega i}$ in equation (2.32) states the damping torque contribution from DFIG to the electromechanical loop of each machine, i.e., M1 and M2. The matrices in (2.32), such as B_{ω} , C_{δ} , C_{ω} , D are of appropriate dimension satisfying the equations (2.23), (2.24) and functions of system parameters such as line reactance, bus voltage, and machine inertia. After substituting the expressions of B_{ω} , C_{δ} , C_{ω} , D, ω , v, obtained from (2.23), (2.6), and (2.8) into (2.31), the elaborated form of damping contribution to the M1 and M2 as a function of system parameters are derived in (2.33) and (2.34).

$$D_{\omega 1} \approx -\frac{E_1' X_{L1} X_{L2}^2 B_r C_r m_1 m_2 [n_1 E_2' + n_2 E_1'] (\delta_2 - \delta_1)}{(X_{L1} + X_{L2}) (E_1' X_{L2} + E_2' X_{L1}) [A_r^2 m_1 m_2 (E_1' X_{L2} + E_2' X_{L1}) + E_1' E_2' V_3 (m_1 + m_2)]}$$
(2.33)

$$D_{\omega 2} \approx -\frac{E_2' X_{L2} X_{L1}^2 B_r C_r m_1 m_2 [n_1 E_2' + n_2 E_1'] (\delta_1 - \delta_2)}{(X_{L1} + X_{L2}) (E_1' X_{L2} + E_2' X_{L1}) [A_r^2 M_1 M_2 (E_1' X_{L2} + E_2' X_{L1}) + E_1' E_2' V_3 (m_1 + m_2)]}$$
(2.34)

The change in damping torque coefficients (D_{w1} , D_{w2}) derived in (2.33) and (2.34), are functions of bus voltage magnitude and angle, line reactance, machine inertia, and parameters of DFIG. According to (2.33) and (2.34), evaluating the effect of damping torque, whether positive or negative, mainly depends on the voltage angle difference between the synchronous machines. As a result, the exclusive expression of damping torques contributed by DFIG as a function of system parameters is derived. The validation of these expressions with a higher-order model is presented in the next section. The proposed methodology, discussed in Section 2.2, can be summarized in the flow chart given in Figure 2.7.

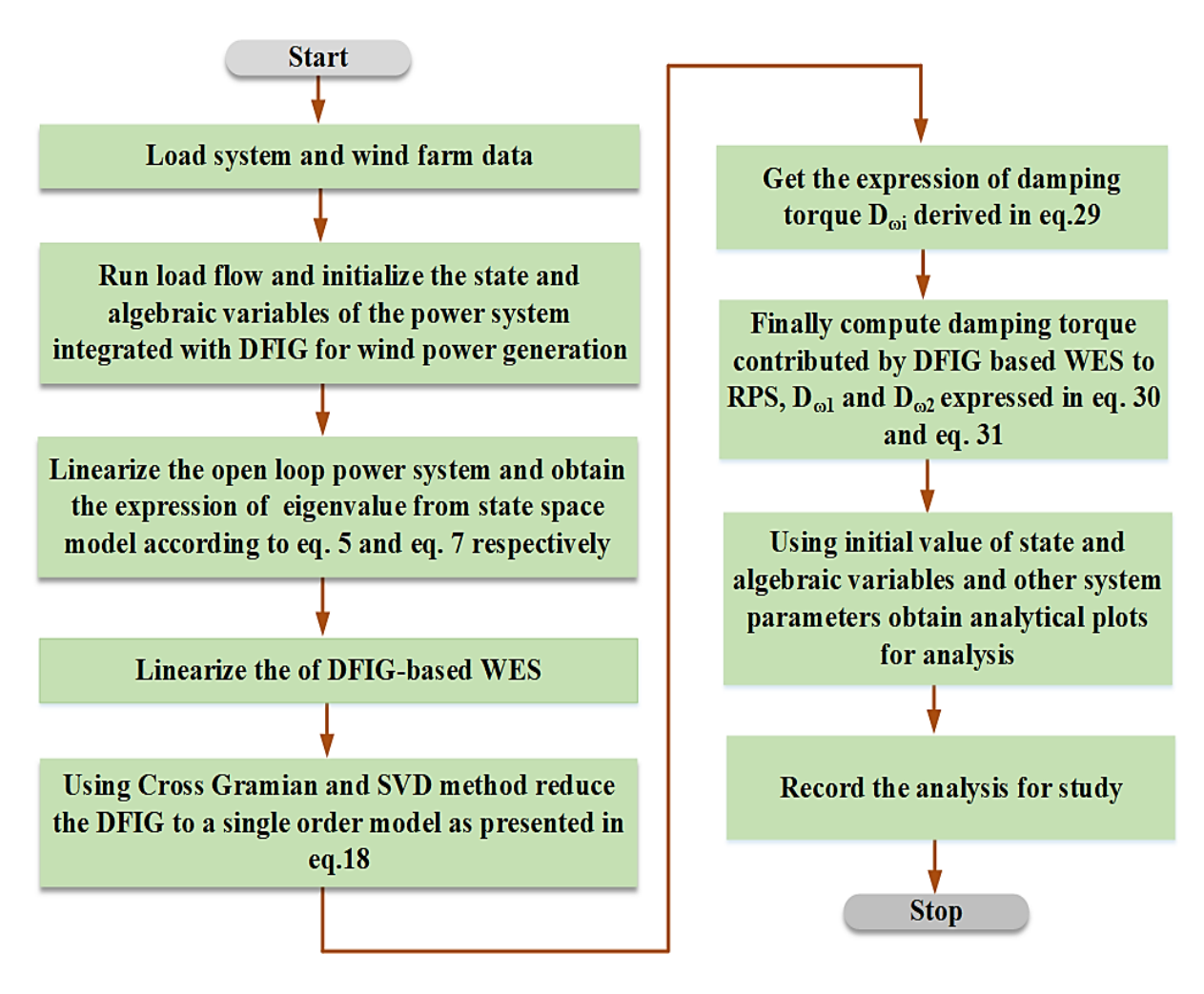


Figure 2.7 Flow chart of the proposed work

2.3 Analytical and Simulation Results

The configuration of Figure 2.1 is considered for various cases presented in this section. There are two synchronous machines in the said configuration, including 5th-order dynamics (4th-order machine model with 1st-order static exciter) and a wind farm comprising 30 nos. of 3.6 MW DFIG-based WTGs. The wind farm is aggregated into a single DFIG model. The data used to model DFIG-based WES is given in Appendix A. 3. The derived damping torque expressions presented in (2.33) and (2.34) have been validated against the full-order system in this subsection. The synchronous machines are presented by (i) the classical model (2nd-order) and (ii) the full-order model (5th-order) for comparison purposes. Data of the three bus systems shown in Figure 2.1 are: $P_{m2} = 1$ p.u, $P_D = 0.87$ p.u, $X'_{d1} = X'_{d2} = 0.05$ p.u., $H_1 = H_2 = 10$ sec. Here X'_{d1} , X'_{d2} , H_1 and H_2 are d-axis transient reactance and inertia constants of M1 and M2,

respectively. All the per-unit values are obtained using the base of 100 MVA. The wind farm is operated with a unity power factor (i.e., $Q_D = 0$). Hence, the wind farm only exchanges real power (P_D) with the power systems. For all the study cases, the wind velocity is assumed to remain within its operating bounds. Please note that the damping torque curve obtained from (2.33) and (2.34) is indicated as that obtained from the reduced-order model.

2.3.1 Study of damping torque influenced by line reactance

In Figure 2.8, the damping torque curves are obtained by assigning line reactance values such as $0.1 \le X_{L1} \le 0.5$ p.u. with $X_{L2} = 0.1$ p.u. Due to the line reactance assigned with the above range, the load flow operation has provided the equilibrium points of voltage magnitude of bus 3 is varied in the range of $0.98 \ge V_3 \ge 0.96$ p.u., and angle of bus 1 and 2, variation has occurred $21^{\circ}.23' \le \delta_1 \le 47^{\circ}.05', -8^{\circ}.4' \le \delta_2 \le -8^{\circ}.26'$. Similarly, in Figure 2.8 (b), the damping torque curves are observed as $0.01 \le X_{L2} \le 0.2$ p.u. with $X_{L1} = 0.2$ p.u. For the given variation of X_{L2} the corresponding equilibrium points acquired from the load flow are as follows: $0.99 \ge V_3 \ge 0.9493$ p.u., $-8^{\circ}.5' \le \delta_1 \le -8^{\circ}.25^{\circ}$, and $17^{\circ}.29' \le \delta_2 \le 39^{\circ}.53^{\circ}$. All these values are used in equations (2.33) and (2.34) to obtain the damping torque curves for Figure 2.8 (a) and (b). The positive and negative torque contributions of Figure 2.8 can be evidenced by the terms $(\delta_2 - \delta_1)$ or $(\delta_1 - \delta_2)$, obtained in (2.33) and (2.34), respectively. The plots in Figure 2.8 represent the impact of line reactance on damping torque provided by DFIG to the RPS. This case study may be useful in practical applications to approximately assess the damping of low-

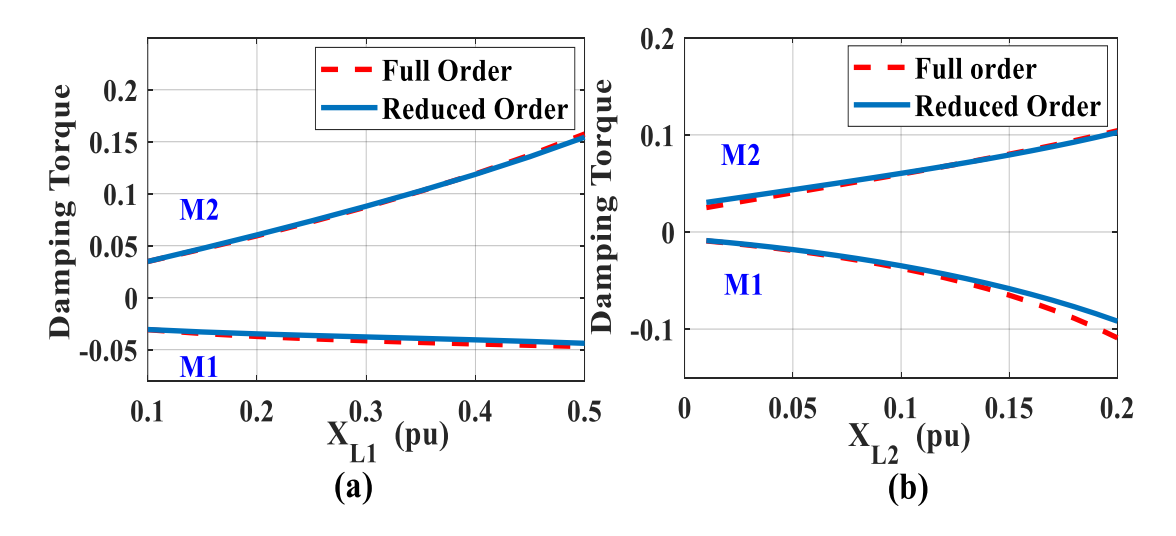


Figure 2.8 Damping torque affected by varying line reactance

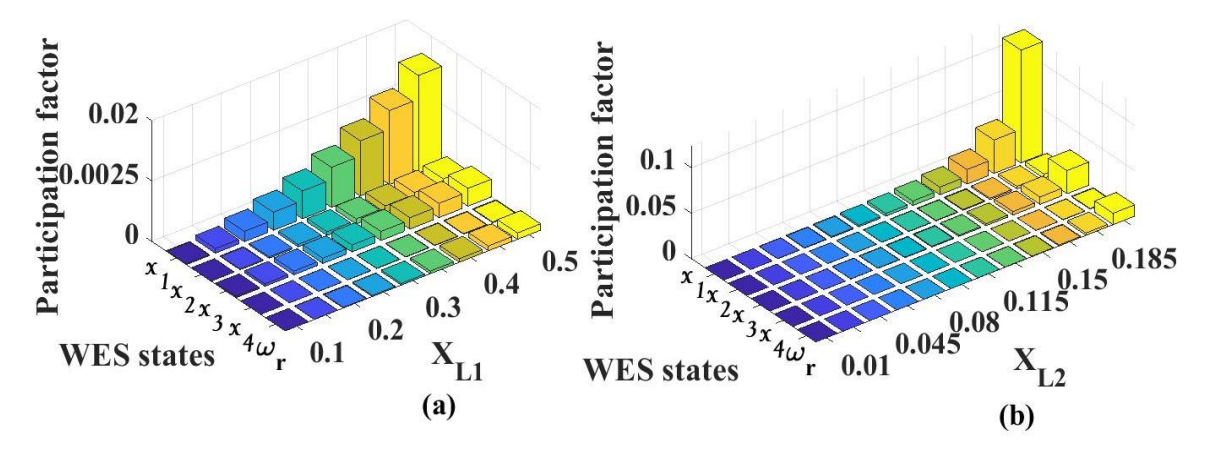


Figure 2.9 Impact of line reactance on WES states participation in the system low-frequency EmOM

frequency electromechanical oscillations of power systems contributed by the DFIG-based WES during the planning and operation of the wind farm. The damping torque contribution is applicable at a rotor frequency of oscillation. In the steady state, no damping is required. Hence, the (2.34) are derived considering a small perturbation in the system. It is expression (2.33) and observed from both Figure 2.8 (a) and (b) that the contribution of the damping torque curves obtained for the reduced-order system is in agreement with that of the full-order system. The figures show that as transmission line reactance increases, damping torque contribution from WES to both the synchronous machines gradually scales up in respective directions. The participation of WES states due to changes in line reactance is represented in Figure 2.9. It can be noticed from Figure 2.9 (a) and (b) that the participation of WES states in the EmOM system gradually increases with the line reactance. Hence, from Figure 2.8 (a) and (b) and Figure 2.9 (a) and (b), it is summarized that more the participation of WES states causes more damping contribution by WES to the electromechanical oscillation loop of synchronous machines. Further, from Figure 2.9 (a) and (b), it is evident that the state variable x_1 has the highest participation in the system mode among the rest of the WES states. Here, x_1 is an intermediate state of the active power controller of DFIG-based WES.

2.3.2 Influence voltage on damping torque contribution

According to (2.33) and (2.34), the damping torque contribution influences the bus voltage magnitude. Similarly, the voltage of bus 1 and bus 2 varies in the desired range to get the damping torque plots as shown in Figure 2.10. To get the plots of Figure 2.10 (a), the line parameters are set as $X_{L1} = 0.2$ p.u., $X_{L2} = 0.1$ p.u. and the voltage of bus 1 and 2 are set such as

 $0.9 \le V_1 \le 1.1$ p.u., and $V_2 = 1$ p.u. The range of V_1 and V_2 are chosen such that a maximum of ±10% of the nominal bus voltage variation is only allowed for normal operation. Assuming $V_1 \approx E_1'$ and $V_2 \approx E_2'$ the bus voltage with the given values, the other equilibrium points as voltage magnitude of bus 3 and angles of bus 1 and 2 are obtained as $0.94 \le V_3 \le 1.01$, 30^0 . $73' \ge \delta_1 \ge$ 24° . 54' and -8° . $63' \le \delta_2 \le -8^{\circ}$. 19', respectively. In a similar fashion, plots of Figure 2.10 (b) are accessed by varying the voltage of bus 2 in the range of $0.9 \le V_2 \le 1.1$ p.u. while keeping the voltage of bus 1 at $V_1 = 1$ p.u.. The load flow operation provides other equilibrium points corresponding to the voltage of bus 3, and the voltage angles of buses 1 and 2 are $0.91 \le V_3 \le$ 1.05 p.u., $30^{\circ}.28' \ge \delta_1 \ge 24^{\circ}.96', -10^{\circ}.31' \le \delta_2 \le -6^{\circ}.17'$, respectively. By using all these values in equations (2.33) and (2.34), the damping torque curves are obtained, as shown in Figure 2.10 (a) and (b). As can be seen in (2.33) and (2.34), the positive and negative torque contributions evident from Figure 2.10 can be justified by the terms $(\delta_2 - \delta_1)$ or $(\delta_1 - \delta_2)$, respectively. From Figure 2.10 (a) and (b) the evaluation of damping contribution to synchronous machines from WES holds good agreement between full-order and reduced-order systems. For the given range of bus voltage variation, the magnitude of damping contribution has scaled down in respective directions with a small effect as bus voltage increases.

The DFIG state participation in system electromechanical oscillation mode due to a change in bus voltage is shown in Figure 2.10. It is observed that the participation of the state x_1 is highest in the whole range of change in bus voltage. The x_1 state has decreased as voltage is increased from 0.9 to 1.1 p.u. The WES state participation is relatively very minimal for the change in bus voltage

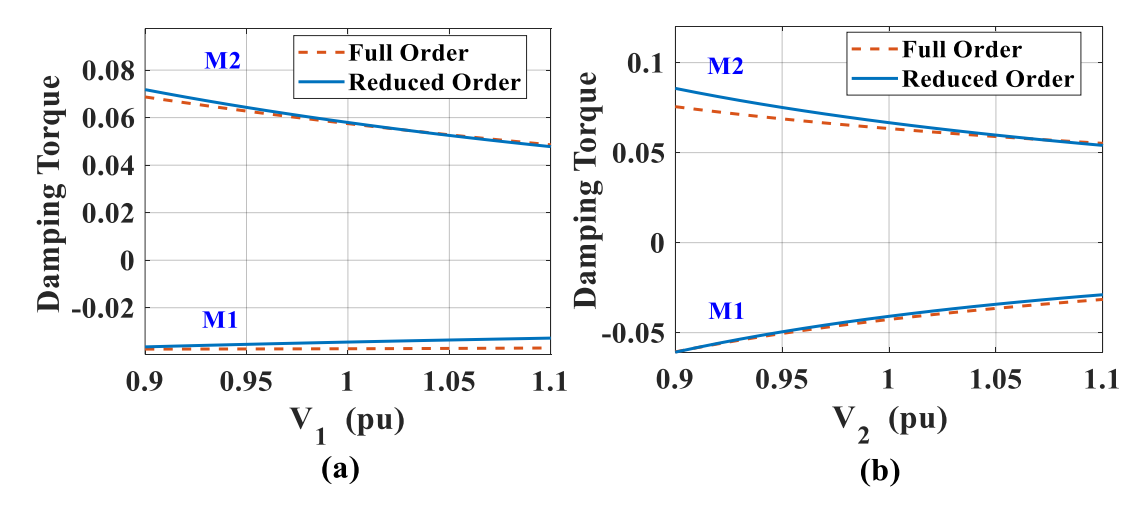


Figure 2.10 Damping torque contribution due to variation of bus voltage

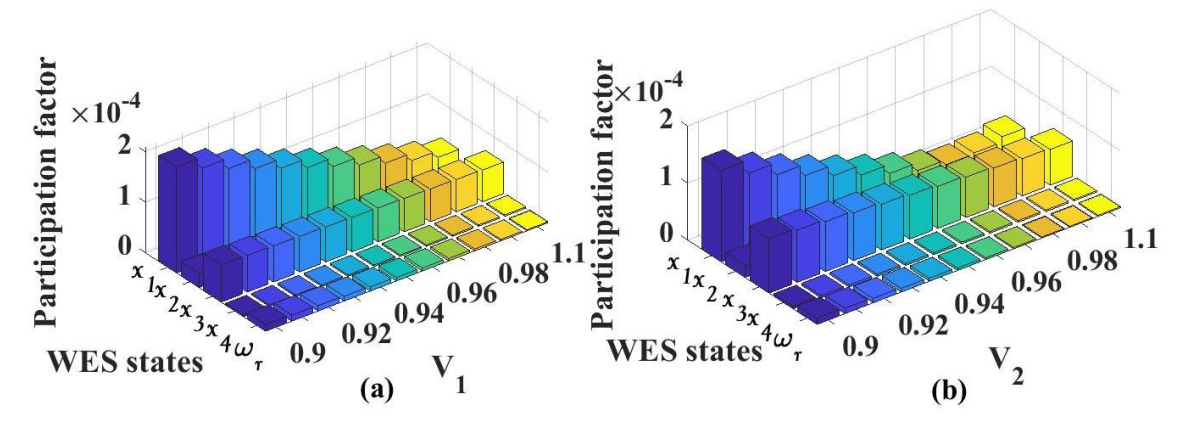


Figure 2.11 Impact of bus voltage on WES states participation in the system low-frequency EmOM

compared to the effect of line reactance, which is also evident from Figure 2.10, that the contribution of damping is minimal in influencing the change in bus voltage to the electromechanical oscillation mode of synchronous machines.

2.3.3 Effect of H constants on damping torque contributions

In Figure 2.12, the scenario is considered for variations in machine inertia. For obtaining the damping torque plots of Figure 2.12, the line reactances are fixed at $X_{L1} = 0.2$ p.u. and $X_{L2} = 0.1$ p.u. Figure 2.12 (a) shows the variation of damping torque by varrying the inertia of M1 as $5 \le H_1 \le 50$ sec., while keeping the inertia of M2 at $H_2 = 10$ sec. As the low inertia systems are more prone to system instability the range of inertia considered for this analysis is from 5 -50 sec. The Similarly, plots of Figure 2.12 (b) are acquired by setting the inertia of M2 as $5 \le H_2 \le 50$ sec., while keeping the inertia of M1 as $H_1 = 10$ sec. For both the scenarios of inertia constants, the equilibrium points of voltage magn itude of bus 3 and angles of bus 1 and 2 are achieved as

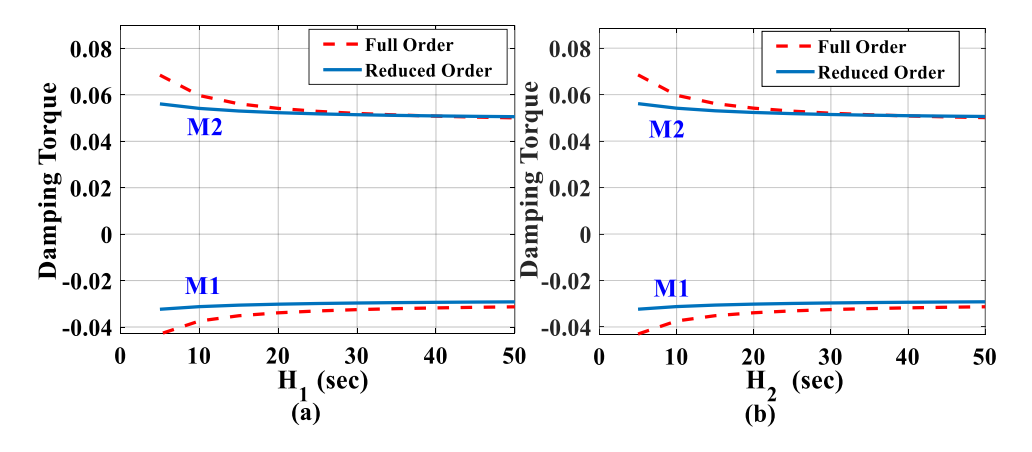


Figure 2.12 Damping toque contribution for various values of inertia constants

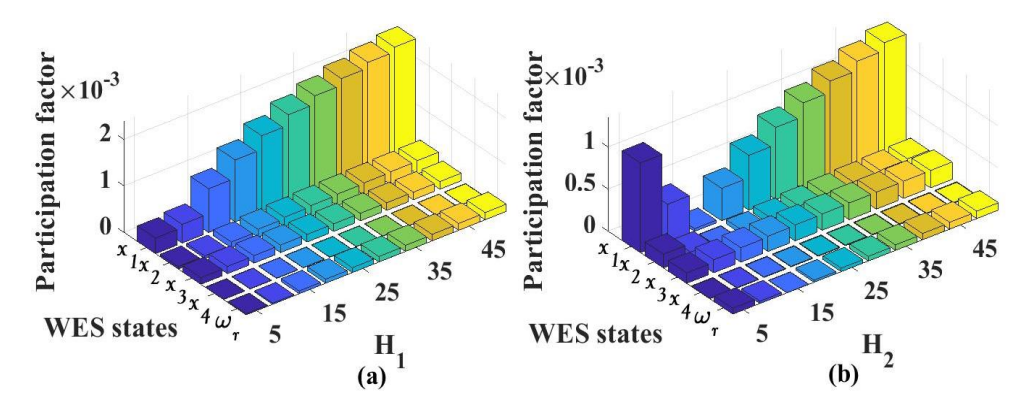


Figure 2.13 Impact of machine inertia on WES states participation in the system low-frequency EmOM

 $V_3 = 0.98$ p.u., $\delta_1 = -8^0.43'$, $\delta_2 = 27^0.47'^0$, respectively. By using these values in damping torque equations of (2.33) and (2.34), the plots of Figure 2.12 are achieved. The positive and negative torque contributions, which are shown in Figure 2.12, are obtained by the terms ($\delta_2 - \delta_1$) and ($\delta_1 - \delta_2$), of (2.33) and (2.34), respectively. It is observed that the curve obtained has error between the reduced and full-order model for the inertia close to 5 is due to the involvement of higher dynamics associated with the full-order model. The full-order system is a 5th-order model that includes the generator dynamics of the 4th order and the exciter of the 1st-order dynamics. As can be noticed in the Figure. 2.12, the error is also below 0.01 range. However, the error for the majority range of the inertia is negligible and has good agreement with that of the full-order system. Both figures show that the *H* constant has an almost negligible influence on the damping contribution provided by DFIG-based WES. The DFIG state participation in system electromechanical oscillation mode influenced by system inertia is provided in Figure 2.13. Here,

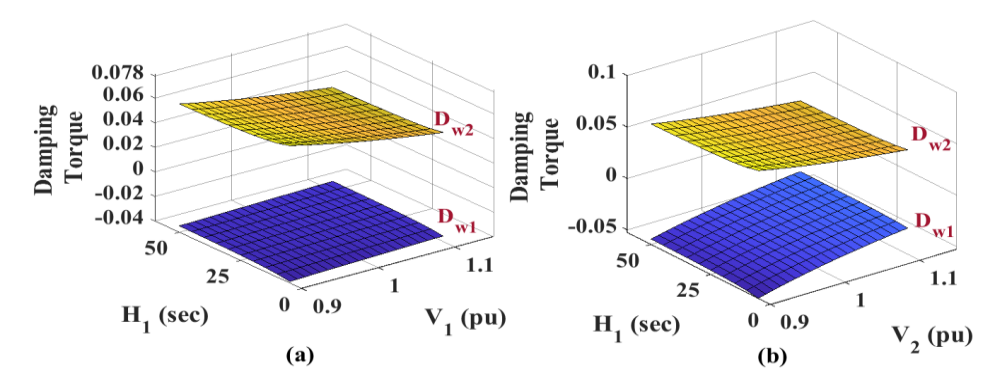


Figure 2.14 Damping contribution due to variation in bus voltage and inertia constants of synchronous machines

also, the state x_1 has the highest participation in the whole range of change in machine inertia. The WES state participation is relatively minimal for the variation in machine inertia compared to the effect of line reactance, which also can be observed from Figure 2.12 that the contribution of damping is insignificant in the influence of change in machine inertia on the EmOM of synchronous machines.

2.3.4 Influence of bus voltage and machine inertia constant on damping contributions

In this sub-section, two scenarios are studied. In Figure 2.14 (a), the damping contribution to M1 and M2 (i.e., D_{w1} , D_{w2}) are obtained for $0.9 \le V_2 \le 1.1$ p.u., $V_1 = 1$ p.u. $5 \le H_1 \le 50$ sec., $H_2 = 10$ sec. It can be observed from Figure 2.14 (b) that for $H_1 = 5$ sec, when $0.9 \le V_1 \le 1.1$ p. u., D_{w1} varies from -0.038 to -0.035 and D_{w2} varies from 0.0717 to 0.048. For $V_1 = 0.9$ p.u, when H_1 is varied from 5 sec. ($H_1 < H_2$) to 50 sec. ($H_1 > H_2$), D_{w1} has varied from -0.038 to -0.0348 and D_{w2} has varied from 0.071 to 0.064, respectively. Similarly, at $V_1 = 1.1$ p.u., when H_1 is varied from 5 sec. to $H_1 = 50$ sec., D_{w1} has varied from -0.035 to -0.032 and D_{w2} has varied from 0.0487 to 0.044, respectively. Identically in Figure 2.14 (b) for any value of H_1 , when $0.9 \le V_2 \le 1.1$ p.u. both $|D_{w1}|$ and $|D_{w2}|$ has decreased, and for any value of V_2 , when $1.5 \le 1.5 \le$

2.3.5 Damping contribution influenced by the location of WES

WES's location significantly affects system stability [21], [82]. In this sub-section, WES's location has been chosen with respect to the Center of Inertia (COI) location. The exact location of COI for Figure 2.1 can be evaluated as follows [11]:

$$\beta_{COI} = \frac{E_1' H_2}{E_1' H_2 + E_2' H_1} \tag{2.35}$$

The location of DFIG-based WES could be somewhere in between the COI location and either bus 1 or bus 2. Hence β is used as a locational parameter to define the line reactance between the DFIG bus (i.e., bus 3) and the rest of the system buses. The line reactance X_{L1} and X_{L2} of

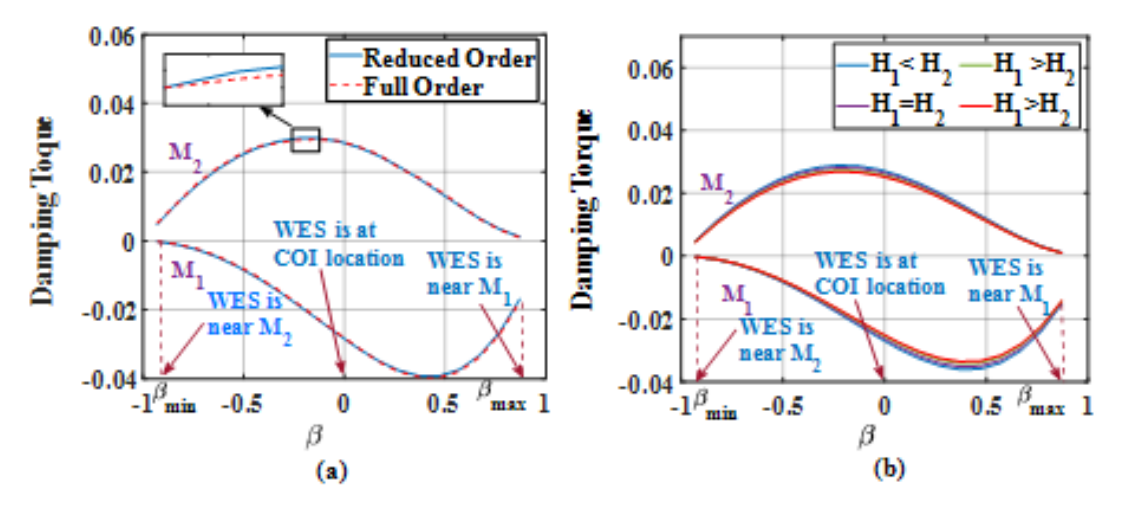


Figure 2.15 Damping contribution corresponds to various locations of WES

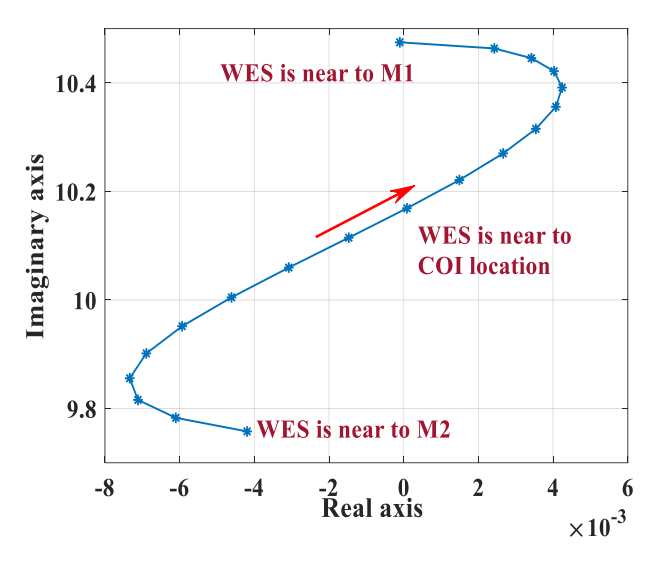


Figure 2.16 Locus of inter-area oscillation mode when the location of WES is varied from M1 to M2

Figure 2.1 can now be defined as:

$$X_{L1} = (1 - \beta)\beta_{COI}X_{L} X_{L2} = (1 + \beta)\beta_{COI}X_{L}$$
 (2.36)

where $X_L = X'_{d1} + X'_{d2} + X_{L1} + X_{L2}$, $\beta_{min} \leq \beta \leq \beta_{max}$, $\beta_{min} = (X'_{d1} - \beta_{COI}X_L)/\beta_{COI}X_L$ and $\beta_{max} = (\beta_{COI}X_L - X'_{d2})/\beta_{COI}X_L$. The damping contribution curve of Figure 2.15 (a) is obtained with, $H_1 = H_2 = 10$ sec., $E'_1 = E'_2 = 1.0$ p. u. The corresponding equilibrium point ranges are: $1.0 \leq V_3 \leq 1.03$ p. u, $18^0.08' \leq \delta_1 \leq 34^0.17'$, $\delta_2 = -1^0.05'$ and $0^0.12' \leq \theta_3 \leq 33^0.53$. Based on the equilibrium points, the damping torque contributed by WES to synchronous machines, evaluated from (2.33) and (2.34), demonstrated in Figure 2.15 (a), holds a good

agreement with the full-order model. The trajectory of the classical model's close-loop inter-area low-frequency oscillation mode for the given equilibrium points is given in Figure 2.16. According to this figure, if the location of DFIG-based WES is farther from the COI location, the critical eigenmode gradually moves towards the left side of the complex plane, which indicates that the system stability improves. In contrast, if the WES is located near the COI location, the critical eigenmode moves towards zero, which means that the ability to improve the stability of the closed-loop system gradually decreases. In Figure 2.15 (b), the damping contribution is obtained for different values of H_1 and H_2 . The damping torque contribution curves are obtained for different scenarios, such as $H_1 < H_2$, $H_1 = H_2$, $H_1 > H_2$. For all scenarios, it has been observed that the change in damping contribution is almost insignificant.

2.4 Discussions and results on multimachine test systems

2.4.1 39 bus test systems

The configuration of the IEEE 39 bus test system is shown in Figure 2.17. The data of the test system is found in [83] and is provided in Appendix A. 4 for reference. In this example, the 4th-order model of synchronous generators and the 3rd-order model of AVRs are adopted. None of the generators are equipped with any damping controllers like PSS. To evaluate the electrical distance of buses from the COI location, a three-phase fault is created at bus 15 for 50 ms. A normalized distance index is recommended in [11] and has been employed here. The index is evaluated from instant, t_0 sec, when fault is applied, to over a period T and is expressed as:

$$D_{k} = \lim_{N \to \infty} \sum_{i=1}^{N} (F_{k}(n_{i}) - F_{COI}(n_{i}))^{2} \cdot \Delta n$$

$$D_{index} = \frac{D_{k}}{\max_{k \in \{1, \dots n_{b}\}} D_{k}}$$
(2.37)

where $\Delta n = T/N$, $n_i = t_0 + \Delta n$, $F_{COI} = \sum_{j=1}^{ng} (H_j f_j) / \sum_{j=1}^{ng} H_j$ and f_j is frequency of j^{th} generator and n_b denotes the total number of buses. From the above set of equations, the higher the value of D_k , the higher the electrical distance between the k^{th} bus and COI is. Therefore, the k^{th} -bus is located under a low concentration of inertia. Hence, the bus with a higher value of D_{index} corresponds to the larger electrical distance between the measured bus and COI. As the COI location may not exactly lie on any bus, the nearest bus can be identified with a lower D_{index} . The

outcome of the distance index is shown in Figure 2.18. The buses are arranged in descending order of D_{index} value. The bus having $D_{index} = 1$, which means that it is far away from the COI location, and the bus with $D_{index} \rightarrow 0$ means that it is very near to the COI location. Figure 2.17 shows the IEEE 39 bus test system with color codes of buses according to the indexing color given in Figure 2.18. According to Figure 2.18, bus 19 is the farthest bus from the COI location in contrast to the generator buses, which are the nearest to the COI location. As the generator buses have $D_{index} \rightarrow 0$, for clarity, these are not shown in Figure 2.18. Hence, bus 19 should be the most suitable location for WES installation. To validate this, the damping contribution from DFIG-based WES to all synchronous generators is evaluated for the WES first installed at bus 19, which is farthest from the COI location. Thereafter, it was installed on bus 2, which is closer to the COI location. WES is modeled by aggregating 200 WTGs to an equivalent single WTG. The DFIG supplies a total of 5.6 p.u. of real power into the power system at the unity power factor mode of

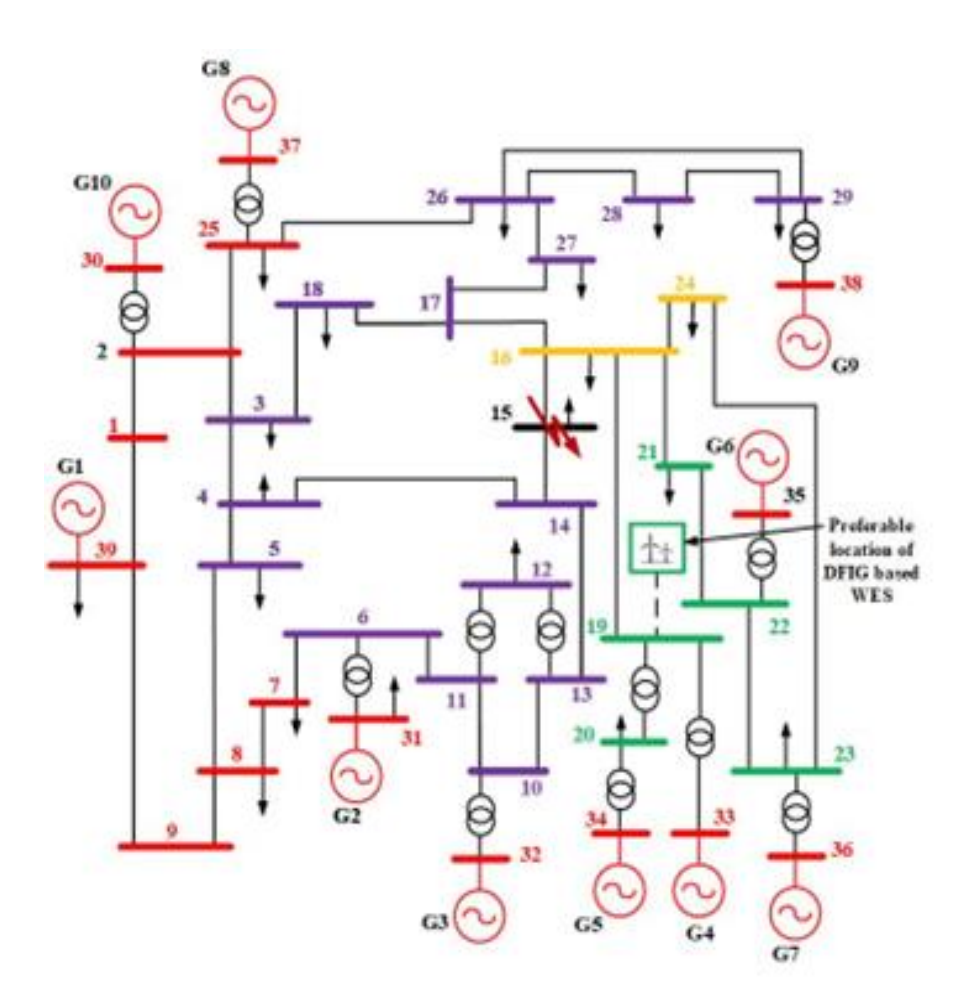


Figure 2.17 Configuration of 39 bus test system with relative distance of buses from COI

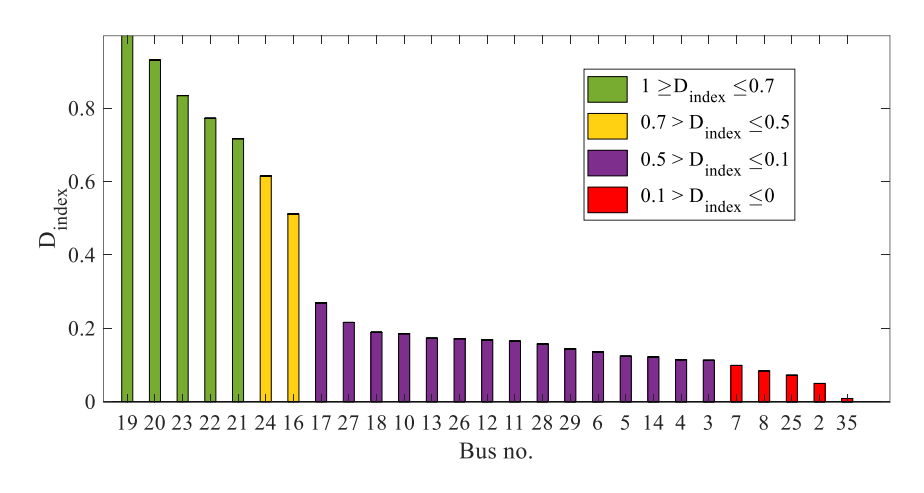


Figure 2.18 Index of Electrical distance from COI among buses of 39-bus systems

operation. The inter-area EmOM that is most crucial for small-signal angular stability is given in the 2nd column of Table 2.2 for the open-loop power system. The damping torque contributions to each of the SGs for each mode are given in Table 2.1, which are being evaluated from (2.30). As given in Table 2.1, for each mode, the damping contribution to most of the SGs are positive when the WES is installed on bus 19, whereas it is negative for most of the SGs when the WES is installed on bus 2. The EmOM of a closed loop system having an interconnection between RPS and WES is presented in Table 2.2. It can be observed from Table 2.2 that λ_1 and λ_2 of the close-loop RPS-WES interconnected system have shifted towards the left side of the complex plane when the WES is installed at bus 19, which is farther from the COI location. In contrast, if the WES is placed at bus 2, closer to the COI location, the modes have shifted towards the right side of the complex plane. From this discussion, it is evident that if WES is located far from the COI location, system stability improves.

The eigenvalue study can be convinced by the time domain simulation curves of generators' rotor angular velocities, shown in Figure 2.19. Considering the concept of electrical distance, bus 19 and bus 2 of the IEEE 39 system are chosen for the installation of WES. As per the above discussion, bus 19 is far away from the COI location, and bus 2 is nearer to the COI location. PSS is not equipped with any generators. Bus 15 is considered to apply a three-phase short circuit fault at 3 sec after the simulation started and cleared by 3.05 sec. Figure 2.19 represents the generators' rotor angular velocity curves in response to the fault for the DFIG placed at bus 19 and 2. An Error Index (EI) is proposed to evaluate the performance of this placement based on the angular velocity of the generators, as given below.

$$EI = \left[\sum_{i=1}^{10} \frac{\left(\omega_n - \omega_{gen}^i\right)^2}{\max_{i \in \{1, \dots, 10\}} \left(\omega_n - \omega_{gen}^i\right)^2} \right]^{1/2}$$
 (2.38)

Here, ω_n is the nominal value of the angular velocity of the system, i.e., 377 (rad/sec) and ω_{gen}^i is the generator rotor angular velocity for generators i=1,...,10. The value of the EI found for the WES locations at buses 19 and 2 are tabulated in Table 2.3. As can be evident from the results in Table 2.3, the EI for the WES location at bus 19 is lower than the WES at bus 2, showing the improvement of damping by placing the source far away from COI. From this discussion, it is obvious that if WES is located far from the COI location, the possibility of system stability has improved. Time domain simulation curves are shown in Figure 2.19, and the results of Table 2.3 can convince the eigenvalue study of generator angular velocities. The system model development and time-domain simulation study were carried out using MATLAB 2019b Simulink/Simscape toolbox.

Table 2.1: Torque Contribution to SGs of IEEE 39 Bus System

Location	λ_1		λ_2	
of WES Generators	WES at bus 19	WES at bus 2	WES at bus 19	WES at bus 2
1	0.008	-0.0375	0.0458	0.1157
2	0.001	-0.0126	0.0011	-0.0107
3	0.0021	-0.0142	0.0013	-0.0055
4	0.0053	-0.0326	0.0052	-0.0098
5	-0.1465	0.7664	-0.111	-0.0062
6	0.0013	-0.0091	0.0010	-0.0018
7	0.0020	-0.0135	0.0011	-0.0005
8	0.0027	-0.0187	0.0041	-0.0146
9	0.0008	-0.0056	-0.0003	0.0177
10	-0.0003	0.0024	-0.0013	0.0084

Table 2.2: Inter-Area Modes for Open Loop RPS and Close Loop Interconnection of RPS and WES

Mode	Open-loop	Close loop		
		WES at bus 19	WES at bus 2	
λ_1	-0.2713±j4.4216	-0.2728 ±j4.4236	-0.2177±j4.3010	
λ_2	-0.2079±j6.2773	-0.2112 <u>+</u> j6.2617	-0.2064±j6.1903	

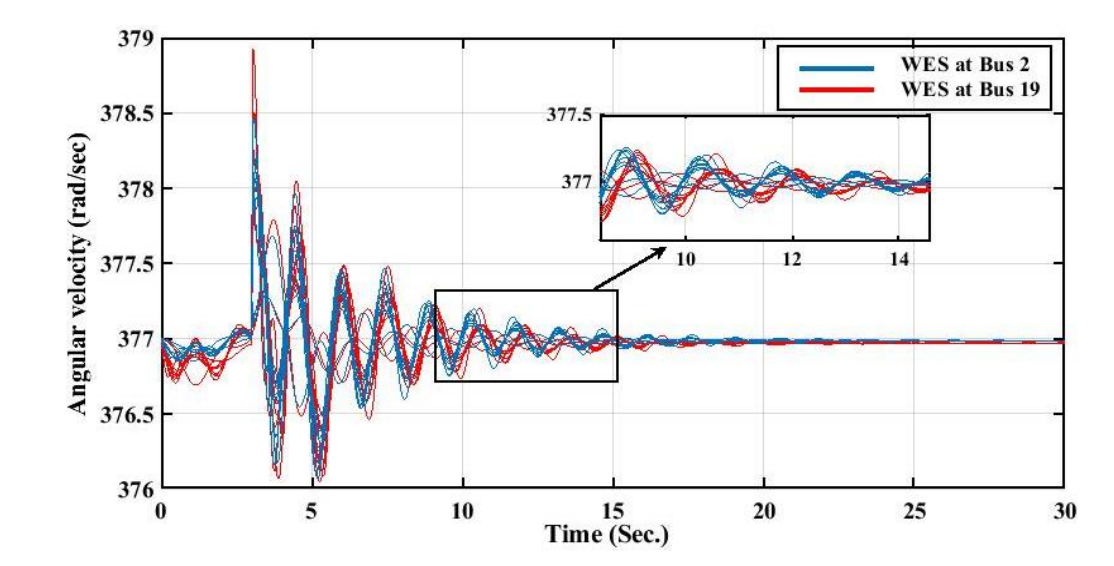


Figure 2.19 Generators' rotor angular velocity for three-phase fault at bus 15

Table 2.3:Error Norm of The Generator Rotor Angle Velocity w.r.t ω_n

WES Location Error	WES at bus19	WES at bus 2
EI	2.13	2.46

2.5 Conclusion

It is paramount to analyze the effect of system parameters on the damping contribution by DFIG to the rest of the power system. Further, how the damping characteristics of the systems depend on the wind farm location from the location of COI. In this research, a mathematical formulation of damping torque offered by DFIG-based WES to the electromechanical oscillation of synchronous machines in terms of the impact of various system parameters like line reactance, bus voltage, and machine inertia. This formulation is unique, and a novel relationship is derived in this research work. However, certain practical assumptions are being considered to simplify this relationship so that an analytical formulation can be obtained. Further, the classical model

represents the synchronous machines, and the DFIG-based WES is reduced to a single-order system by Cross-Gramian and SVD methods without loss of generality. The accuracy of this analytically formulated model is compared with the full-order system (without any assumptions) representation model, where the M1 and M2 are represented by 5th-order dynamics (4th-order machine model with 1st-order static exciter) and 5th-order DFIG model, as mentioned in Section 2.2. The comparative results presented in Figure 2.5, Figure 2.8, Figure 2.10, Figure 2.12, and Figure 2.15 show the accuracy of the analytical model. Further, the model accuracy is validated from the non-linear time domain simulation results in Section 2.4 for the IEEE 39 bus test system. In this model, all the synchronous machines, including DFIG-based WES, are assumed to be a full-order system. After going through the results obtained for damping torque influenced by system parameters, the main findings of the proposed work are as follows:

- i. The damping torque produced by DFIG to the EOL of RPS is greatly influenced by transmission line reactance.
- ii. The parameters like bus voltage and synchronous machine inertia have a negligible impact on the damping torque contributed by DFIG.
- iii. The positive or negative characteristic of damping torque mainly happens due to the load angle difference between synchronous machines.
- iv. A better damping phenomenon is observed in the low-frequency oscillatory mode of the system, while the DFIG-based WES is chosen to be located far from COI.

The presented study of the chapter is based on a particular operating condition. However, different operating conditions differ by different loading levels and power output. Therefore, different conditions exert different operating points around which the system is linearized for small signal stability analysis and different operating points may have varying stability margin and damping characteristics. Similarly, different types of fault and duration of fault significantly influence the dynamics performance of the system, which can have a leading impact on the rotor angle, and rotor velocity of both DFIG and synchronous machine. Therefore, the stability and the damping performance of DFIG and synchronous machines will be affected. Hence, the control system of DFIG can be tuned further to enhance damping performance according to varying

operating points and types of faults. The outcome of this research could potentially include a detailed investigation of some practical applications. For example,

- (a) While designing any damping controller for WES/conventional generator or FACTS, it is necessary to examine their impact on the small-signal angular stability of the system. This research can help to investigate the positive or negative influence on the power system EOL. Once the positive or negative damping contribution to power system EOL is found, the control parameters can be tuned to alter the impact.
- (b) In the planning stage, when a preferable location needs to be identified for WES placement, it has minimal effect on the small-signal stability of the power system.

Chapter 3

Small Signal Stability Analysis of DFIG-based Wind Energy-Integrated Power Systems

Wind Energy Systems (WESs) based on Doubly-Fed Induction Generators (DFIGs) have enormous potential for meeting the future demands related to clean energy. Grid integration of WES challenges the stability of power systems due to low inertia and intermittent power injection offered by DFIGs. The research of this chapter proposes mathematical formulations to compute synchronizing and damping torque coefficients of a WES-integrated Single Machine Infinite Bus (SMIB) system while considering Phase Locked Loop (PLL) and Virtual Inertia Controller (VIC) dynamics. In addition, a Power System Stabilizer (PSS) is designed to enhance electromechanical oscillation damping in wind energy-integrated power systems. The proposed research methodology is tested in SMIB and nine-bus test systems integrated with WES under several case studies.

3.1 Introduction

The DFIG-based WES is synchronized with the main power grid through PLL. In addition, using VIC technology with high penetration of DFIG-based WES enhances the stability and security of the power system. Hence, the consequence on stability in a WES-integrated power system is very much associated with the combined influence of PLL and VIC dynamics. The various technologies adopted by VIC in DFIG-based WES provide frequency support either by (a) injecting active power from energy storage devices [29] or (b) by extracting kinetic energy stored in the wind farm [30]. The mathematical model adopted for VIC in this chapter considers that the frequency support provided by the VIC is carried out by extracting kinetic energy stored in the wind farm.

The proposed research work in this chapter investigates the effects of DFIG integration on the electromechanical oscillation dynamics of the Synchronous Generator (SG) under the combined influence of a PLL and VIC. In addition, this work has also investigated a novel PSS design approach under the combined influence of PLL and VIC dynamics of a DFIG to improve the electromechanical oscillatory characteristics of the power system. These objectives are achieved

by developing mathematical functions for a Single-Machine Infinite Bus (SMIB) system integrated with a DFIG-based WES that defines the electromechanical dynamics of the SG. The contributions of this chapter are outlined as follows:

- 1) A mathematical formulation is developed based on the effects of the VIC of a DFIG-based wind farm on the electromechanical dynamics of a power system under the influence of PLL. As part of the formulation, the joint effect of the VIC and PLL are incorporated by retaining the original Heffron-Phillips structure.
- 2) Based on the modified Heffron-Phillips model, a PSS for SMIB is designed with parameters tuned to consider the effects of the VIC and PLL of a DFIG-based wind farm.
- 3) The effects of the VIC and PLL on the Electromechanical Oscillatory Mode (EmOM) are characterized by changes to synchronizing and damping torque coefficients, which are functions of VIC and PLL parameters.
- 4) Finally, a systematic analysis is conducted to explore the expression of change in synchronizing and damping torque coefficients with respect to increased proportional gains of the VIC. A time-domain simulation of a VIC-installed WES integrated with a single machine system and IEEE 9-bus system is conducted to validate the theoretical foundation.

3.2 Model of DFIG-Based Wind-Integrated Power System

The analysis demonstrated in this research consists of a DFIG-based wind system integrated into an SMIB. Figure 3.1 presents a schematic of DFIG integration with the SMIB. In this research, the DFIG-based wind system is modeled by aggregating multiple DFIGs of equal capacities and operating states connected in a parallel configuration. However, a single DFIG model is obtained by aggregating the individual wind turbine units. The complete system associated with a DFIG-based wind system is classified into three categories: mechanical system, induction generator, and converters with controllers.

3.2.1 Modeling of a Mechanical System

A single-mass drive-rotational system models the mechanical part of the overall power system. The mechanical system provides the input power to the wind system based on wind veloc-

ity. The shaft torque, i.e., the input to the wind turbine, is defined by:

$$T_{shD} = \sum_{i=1}^{n} \frac{1}{2} B \omega_s C_p^i \frac{(V_w^i)^3}{\omega_{rD}}$$
 (3.1)

where B, C_p , ω_{rD} , ω_s , and V_w are the torque parameter, power coefficient of the wind turbine, rotor angular velocity of the DFIG, rotor angular velocity of the SG, and wind velocity, respectively. The dynamics of the single-mass model of the rotational system can be defined as:

$$\frac{d\omega_{rD}}{dt} = \frac{\omega_s}{2H_D} (T_{shD} - T_{eD}) \tag{3.2}$$

where H_D is the inertial constant of the Wind Turbine Generator (WTG), and T_{eD} is the electromagnetic torque of the DFIG, which is given by:

$$T_{eD} = E'_{Dd}I_{Dds} + E'_{Dq}I_{Dqs} (3.3)$$

where $E'_{Dq} - jE'_{Dd}$ and $I_{Dqs} - jI_{Dds}$ are the rotor-induced Electromotive-Force (EmF) and stator current of the DFIG in the d-q axis, respectively.

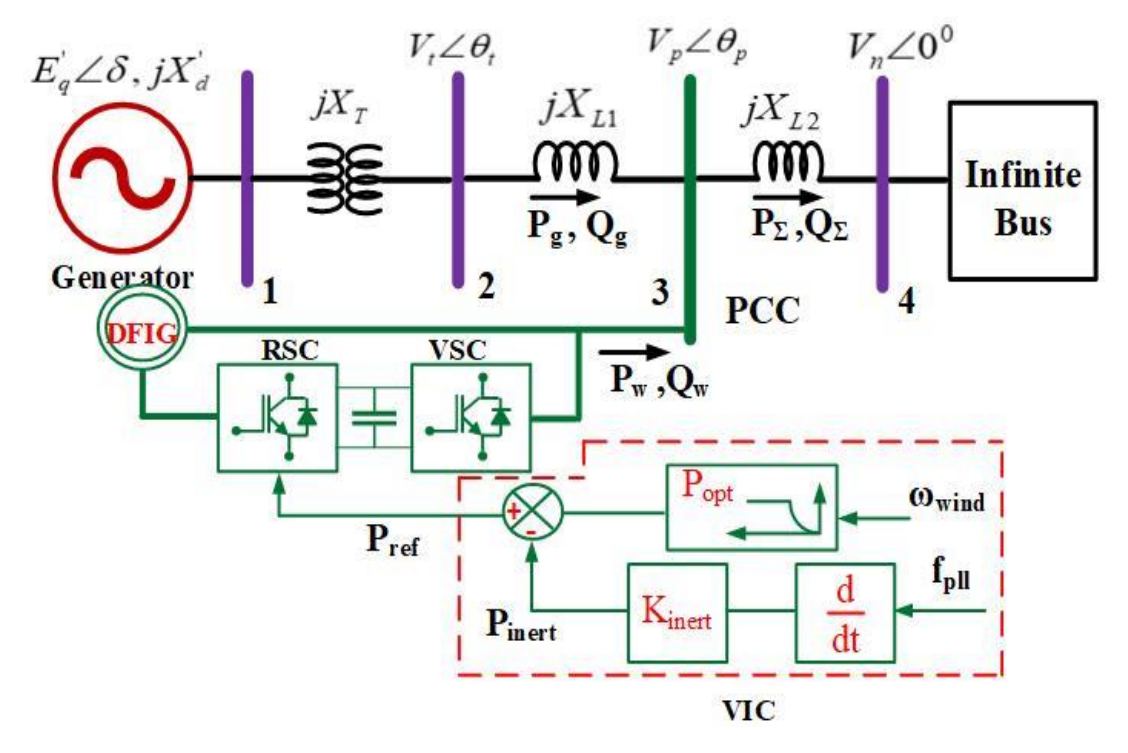


Figure 3.1 Modified SMIB system

3.2.2 Modeling of DFIG

DFIGs are used to generate electricity from available wind power. The rotor flux dynamics are used to simulate the DFIG, assuming that the stator flux linkage is infinitely fast. The dynamics of internal-induced EMF in the d-q axis of DFIG can be expressed as:

$$\frac{dE'_{Dd}}{dt} = \frac{1}{T'_o} \left((X'_s - X_s) I_{Dds} - E'_{Dq} \right) + (\omega_{rD} - \omega_s) E'_{Dd} + \frac{X_m}{X_r} \omega_s V_{Ddr}$$
(3.4)

$$\frac{dE'_{Dq}}{dt} = \frac{1}{T'_o} \left((X_s - X'_s) I_{Dqs} - E'_{Dd} \right) - (\omega_{rD} - \omega_s) E'_{Dq} - \frac{X_m}{X_r} \omega_s V_{Dqr}$$
 (3.5)

where T'_o , X_s , X'_s , X_r and X_m are the open-circuit transient time constant, stator reactance, stator transient reactance, rotor reactance, and mutual reactance of the stator and rotor of a DFIG, respectively, and $V_{Dqr} - jV_{Ddr}$ is the d-q axis rotor voltage of the DFIG.

3.2.3 Modeling of Controllers Associated with Converters

.The converters at the rotor and grid sides are known as the Rotor-Side Converter (RSC) and Grid-Side Converter (GSC), respectively. The GSC in this research is modeled as a constant current source. The transient behavior of the active and reactive power controllers of the RSC are expressed as:

$$\begin{cases} \frac{dx_{1}}{dt} = K_{i1}(P_{ref} - P_{gen}) \\ \frac{dx_{2}}{dt} = K_{i2}(K_{p1}(P_{ref} - P_{gen}) + x_{1} - I_{Dqr}) \\ \frac{dx_{3}}{dt} = K_{i3}(Q_{ref} - Q_{gen}) \\ \frac{dx_{4}}{dt} = K_{i4}(K_{p3}(Q_{ref} - Q_{gen}) + x_{3} - I_{Ddr}) \end{cases}$$
(3.6)

where $P_{ref/gen} - jQ_{ref/gen}$ are the reference/generated power outputs of the DFIG, respectively; $K_{px} + \frac{K_{ix}}{s}$; x = 1,2,3,4 are the Proportional Integral (PI) controllers associated with the RSC, x_1, x_2, x_3, x_4 are the state variables associated with RSC controllers; and $I_{Dqr} - jI_{Ddr}$ are the rotor currents in the d-q axis of the DFIG. Based on the assumption that the wind velocity is within its limit, the transient of the pitch angle controller is not included here. This chapter conducts stability

analysis for a DFIG-based wind energy-integrated power system using a PLL for grid synchronization and VIC to provide inertial support during frequency deviation events. The following equations describe the transient behavior of the PLL:

$$\frac{dx_{pll}}{dt} = K_i^{pll} V_p (\theta_p - \theta_{pll})$$
(3.7)

$$\frac{d\theta_{pll}}{dt} = K_p^{pll} V_p (\theta_p - \theta_{pll}) + x_{pll}$$
(3.8)

where $V_p \angle \theta_{pll}$ is the voltage at PCC, $K_p^{pll} + \frac{K_i^{pll}}{s}$ is the PI controller used in PLL and x_{pll} is the intermediate state variable related to the PI of PLL. The transient of the VIC is modeled by:

$$\frac{dx_{vic}}{dt} = \frac{1}{T} \left(f_{pll} - x_{vic} \right) \tag{3.9}$$

The f_{pll} , x_{vic} , and T are PLL output frequency, associated state variable, and time constant of VIC, respectively. Composing equations from (3.2) - (3.9), the transient equivalent model of the DFIG-based wind system can be represented by:

$$\dot{x}_w(t) = w(t) \tag{3.10}$$

where $x_w(t) = \left[\omega_{rD}, E'_{Dd}, E'_{Dq}, x_1, x_2, x_3, x_4, x_{pll}, \theta_{pll}, x_{vic}\right]$ and w(t) are the functions of the first derivative of the state variables. In this manner, the 10th-order model of the DFIG is integrated into the power system, where the power system in this work is composed of 4th-order SGs. The following state equations define the small-signal equivalent model of the open loop Rest of the Power System (RPS) and the DFIG-based wind energy system:

$$\begin{cases} \Delta \dot{x}_S = A_S \Delta x_S + B_S \Delta P_W \\ \Delta V_P = C_S \Delta x_S + D_S \Delta P_W \end{cases}$$
(3.11)

$$\begin{cases} \Delta \dot{x}_w = A_w \Delta x_w + B_w \Delta V_P \\ \Delta P_w = C_w \Delta x_w + D_w \Delta V_P \end{cases}$$
(3.12)

where the state vector of n SGs of the power system is $x_S = [\delta, \omega, E'_q, E_{fd}]_{7 \times n}^T$; the state variables δ , ω , E'_q , and E_{fd} are the load angle, angular velocity, transient internal EMF, and exciter field voltage, respectively; x_w is the state vector of the WES and P_w and V_P are the injected power and

voltage at the Point of Common Coupling (PCC) of the DFIG, respectively. The A_s , B_s , C_s , and D_s of (3.11) are the state matrix, input matrix, output matrix, and feedforward matrix, respectively. Similarly, A_w , B_w , C_w , and D_w of (3.12) is defined in a similar fashion as of (3.11). From (3.11) and (3.12), the state equation of the entire system takes the following form:

$$\dot{x} = A_{sys}x\tag{3.13}$$

where $x = [x_S, x_w]^T$ and A_{sys} is the closed-loop system state matrix. The following assumptions are adopted in the subsequent sections to investigate the effects of the DFIG-based WES on the power system under the influence of VIC and PLL dynamics.

- 1) A single-mass drive-train system models the mechanical part of the wind turbine.
- 2) The turbine pitch angle controller is not modeled.
- 3) The GSC is modeled as a controlled current source.
- 4) All analyses are conducted on the assumption of a constant wind velocity, where the wind velocity is assumed to be within the operational limit.
- 5) The nominal frequency of the entire system is 60 Hz.

3.3 Dynamic Modeling of an SMIB with a DFIG-based WES

An infinite bus in the SMIB system represents a power system with infinite inertia, such that it can absorb or supply power without any significant change in voltage or frequency. Hence, in a small signal stability study, this assumption allows to focus on other factors like power system stability through dynamics associated with rotor angle oscillation, exciter control, and PSS. In this context, the linearized model of the synchronous generator is used to approximate system dynamics around an operating point. This section develops a modified Heffron-Phillip model for small signal stability analysis that consists of 3rd order model of a generator, 1st order model of AVR, and a DFIG-based WES endowed with a VIC. The VIC can support power system frequency by changing the reference current of the RSC controller [39]. The VIC is installed near the RSC of the DFIG. Practically, as Figure 3.1 shows, the change in system frequency is measured by the PLL of the DFIG and processed through the VIC as a positive frequency error, which is then transformed into a corresponding inertial power output of VIC (*Pinert*). Thus, in frequency

excursion events, P_{inert} alters the reference of the RSC active power controller to extract the stored kinetic energy of the rotor. An improper gain setting on the VIC controller can adversely affect the system's operation and stability. Even though the system frequency of the SMIB is assumed constant, small disturbances in the given system can influence the PLL dynamics in phase tracking, which in turn impacts the output power of DFIG. Therefore, it is essential to investigate the exact impact of the VIC on the power system's small-signal stability. This section describes the theoretical basis for small-signal stability analysis of an SMIB system integrated with a DFIG-based WES. The theoretical study interprets how the dynamics of a PLL and VIC of a WES affect the electromechanical modes of the SG. As Figure 3.1 shows, an SG is installed at bus 1, and the DFIG is installed at bus 3. Buses 1 and 3 are connected through a transformer and lossless transmission line. The SG is modeled as a 3^{rd} -order flux decay model [79]. The differential equations associated with SGs and exciter dynamics [79] are given as:

$$\begin{cases} \dot{\delta} = \omega - \omega_s \\ \dot{\omega} = \frac{\omega_s}{2H} \left(P_m - P_g \right) \\ \dot{E}'_q = \frac{1}{T'_{do}} \left(E_{fd} - E'_q - (X_d - X'_d) I_d \right) \\ \dot{E}'_{fd} = \frac{1}{T_A} \left(-E_{fd} + K_A \left(V_{ref} - V_t \right) \right) \end{cases}$$

$$(3.14)$$

The variables and parameters of (3.14) follow the standardized notations from [79]. In the absence of a WES, the power balance equation at bus 3 satisfies:

$$\begin{cases}
P_{\Sigma} = P_g \\
Q_{\Sigma} = Q_g
\end{cases}$$
(3.15)

where
$$P_g = \frac{E_q' V_p}{X_{L1} + X_t + X_d'} \sin(\delta - \theta_p)$$
, $P_{\Sigma} = \frac{V_p V_n}{X_{L2}} \sin\theta_p$, $Q_g = \frac{E_q' V_p}{X_{L1} + X_T + X_d'} \cos(\delta - \theta_p) - \frac{V_p^2}{X_{L1} + X_T + X_d'}$, $Q_{\Sigma} = \frac{V_p^2}{X_{L2}} - \frac{V_p V_n}{X_{L2}} \cos\theta_p$; $V_p \angle \theta_p$ and $V_n \angle 0^0$ are bus voltages of the PCC and infinite bus, respectively, and X_d and X_d' are the d -axis steady-state and transient reactance of the SG, respectively. The transmission lines and transformers are considered to be lossless. Thus, the line and transformer equivalent impedances are represented only with reactance (i.e., X_{L1}, X_{L2} , and X_T , respectively). Linear modal analysis is conducted by linearizing the nonlinear differential-algebraic equations of the power system given in (3.14) and (3.15). In small-signal stability

analysis, the change in electrical power output following a perturbation can be resolved into two components: synchronizing and damping power. Hence,

$$\Delta P_a = P_S \Delta \delta + P_D \Delta \omega \tag{3.16}$$

where P_S and P_D are the synchronizing and damping coefficients, respectively. The coefficients can be evaluated for an Electromechanical Mode of Interest (EMI) $\bar{\lambda}_c$ and are widely used to measure the small-signal stability of power systems [84]. This section describes how the modified Heffron-Phillips model was evaluated under the joint effect of VIC-PLL for EMI $\bar{\lambda}_c$. To incorporate the effects of the WES, the power balance expressed in (3.15) can be augmented to:

$$P_{\Sigma} = P_g + P_w \tag{3.17}$$

The linear form of (3.17) can be expressed as:

$$\Delta P_{\Sigma} = \Delta P_g + \Delta P_w \tag{3.18}$$

where
$$\Delta P_{\Sigma} = \left(\frac{V_{po}V_{no}}{X_{L2}}\cos\theta_{p0}\right)\Delta\theta_{p} + \frac{P_{go}}{V_{po}}\Delta V_{p}$$
; and $\Delta P_{g} = \left(\frac{E'_{qo}V_{po}}{X_{1}}\cos(\delta_{0}-\theta_{p0})\right)\left(\Delta\delta-\Delta\theta_{p}\right) + P_{go}\left(\frac{1}{E'_{qo}}\Delta E'_{q} + \frac{1}{V_{po}}\Delta V_{p}\right)$, in which X_{1} is defined as $X_{1} = X_{L1} + X_{T} + X'_{d}$. The variables with subscript "0" indicate the initial operating points. Based on [24] and [85], the DFIG-based WES without VIC is practically decoupled from the RPS (i.e., the rotor velocity is decoupled with grid frequency). Therefore, the DFIG output active power (P_{w}) does not vary with small disturbances at the grid side. However, a DFIG endowed with VIC can modulate P_{w} with a variation in grid frequency. The frequency variation at the PCC is measured by the PLL. Thus, the active power output variation with the VIC and PLL can be defined as:

$$\Delta P_w = \begin{cases} -sK_{inert} \Delta f_{pll} & \text{With VIC and PLL} \\ 0 & \text{Without VIC} \end{cases}$$
(3.19)

where K_{inert} and f_{pll} are the proportional gain of the VIC and the frequency at the PCC measured by the PLL, respectively. A PLL based on a Synchronously-Rotating-Reference Frame (SRF-PLL) considered in this work is shown in Figure 3.2. Based on the assumption that $V_p = 1$ p. u., the relationship between Δf_{pll} and $\Delta \theta_p$ can be expressed as:

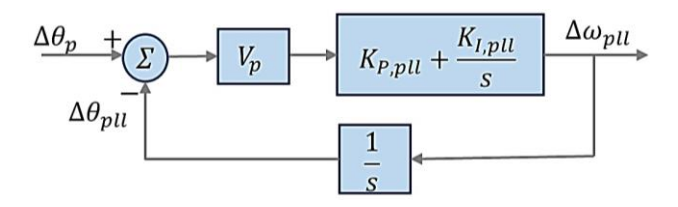


Figure 3.2 A Model of SRF PLL

$$\Delta f_{pll} = \frac{s}{2\pi} \left(\frac{sK_{P,pll} + K_{I,pll}}{s^2 + sK_{P,pll} + K_{I,pll}} \right) \Delta \theta_p \tag{3.20}$$

Thus, with the PI parameters of the PLL (i.e., $K_{P,pll}$ and $K_{I,pll}$), (3.19) can be rewritten as:

$$\Delta P_{w} = \begin{cases} -s^{2} \frac{K_{inert}}{2\pi} \left(\frac{sK_{P,pll} + K_{I,pll}}{s^{2} + sK_{P,pll} + K_{I,pll}} \right) \Delta \theta_{p} \\ 0 \end{cases}$$
(3.21)

Next, to consider the contribution of wind power controllers, the change in wind energy active power output can be expressed as:

$$\Delta P_w = -s^2 \frac{K_{inert}}{2\pi} F_{pll}(s) \Delta \theta_p \tag{3.22}$$

Similarly, the reactive power balance of (3.15) is linearized around the initial operating point to obtain the expression of ΔV_p . Based on the assumption that the DFIG reactive power output $Q_w = 0$, the linearization of the reactive power balance of (3.15) becomes:

$$\Delta Q_g - \Delta Q_{\Sigma} = 0 \tag{3.23}$$

where

$$\begin{cases} \Delta Q_{\Sigma} = \frac{V_p}{X_{L2}} \Delta V_p + \frac{Q_{\Sigma 0}}{V_{p0}} \Delta V_p + P_{\Sigma 0} \Delta \theta_p \\ \Delta Q_g = \frac{V_{p0}}{X_1} cos(\delta_0 - \theta_{p0}) \Delta E_q' - P_{g0} (\Delta \delta - \Delta \theta_p) + \\ \left(\frac{Q_{g0}}{V_{p0}} - \frac{V_{p0}}{X_1}\right) \Delta V_p \end{cases}$$

$$(3.24)$$

A modified Heffron-Phillips model can then be obtained by linearizing the nonlinear dynamics of the power system defined in (3.14) - (3.23) at an operating point when considering the dynamics of a wind-generator system endowed with VIC. The additional contribution to the original K_1 to K_6 constants of the SMIB can be obtained, respectively, as:

$$\Delta K_{1} = \frac{X_{L2}E'_{q0}{}^{2}V_{p0}\cos^{2}(\delta_{0} - \theta_{p0})}{X_{1}M_{en}}D(s) \quad \Delta K_{4} = \frac{P_{g0}(X_{d} - X'_{d})\cos(\delta_{0} - \theta_{p0})}{M_{en}/X_{L2}}D(s)$$

$$\Delta K_{2} = -\frac{P_{g0}X_{L2}\cos(\delta_{0} - \theta_{p0})}{X_{1}M_{en}}D(s) \quad \Delta K_{5} = \frac{X_{L1}X_{L2}P_{g0}}{M_{ep}}D(s)$$

$$\frac{1}{\Delta K_{3}} = \frac{P_{g0}^{2}(X_{d} - X'_{d})}{V_{p0}}D(s) \quad \Delta K_{6} = -\frac{P_{g0}^{2}X_{L1}X_{L2}X_{1}X'_{d}}{E'_{q}V_{P0}M_{en}M_{ep}}D(s)$$

$$\Delta K_{6} = -\frac{P_{g0}^{2}X_{L1}X_{L2}X_{1}X'_{d}}{E'_{q}V_{P0}M_{en}M_{ep}}D(s)$$
(3.25)

where
$$D(s) = \frac{s^2 \frac{K_{inert}}{2\pi} F_{pll}(s)}{\frac{V_{p0}}{X_1 X_{L2}} M_{en} + s^2 \frac{K_{inert}}{2\pi} F_{pll}(s)}$$
; $M_{en} = V_{no} X_1 \cos \theta_{po} + E'_{qo} X_{L2} \cos (\delta_0 - \theta_{p0})$; and $M_{ep} = V_{no} X_1 \cos \theta_{po}$

 $E'_{qo}X_{L1}\cos(\delta_0-\theta_{t0})+V_{po}X'_d\cos(\theta_{t0}-\theta_{p0})$. The steps for deriving the aforementioned functions are presented in Appendix A. 2. The modified K_1 to K_6 are then transformed into:

$$\begin{cases} G_i(s) = K_i + \Delta K_i(s) & i = 1, 2, \dots, 6, i \neq 3 \\ \frac{1}{G_i(s)} = \frac{1}{K_i} + \frac{1}{\Delta K_i(s)} & i = 3 \end{cases}$$
(3.26)

All $G_i(s)$ retain the properties of the classical Heffron–Phillips model, as shown in Figure 3.3. The following section describes the PSS design procedure in the presence of VIC and PLL.

3.4 Design Algorithm for PSS

The Phillip-Heffron model is best suited for low-frequency oscillation analysis and the design of PSS to provide additional damping torque. The design of a PSS for the SG, while considering the effects of the VIC and PLL dynamics of the DFIG, can improve the system's damping properties. Instead of those of the Conventional PSS (CPSS), the parameters of the proposed PSS are derived from the modified Heffron-Phillips model that incorporates the VIC and PLL dynamics of the DFIG. However, the structure of the transfer function model is identical to that of the CPSS. Thus, no limitation exists for the proposed PSS from a mathematical or implementation standpoint. The most efficient design of the PSS is through formulating the transfer function of GEP(s), where GEP(s) represents the transfer function between the change in electrical power output and the reference voltage, as shown in Figure 3.3 and expressed as:

$$GEP(s) = \frac{-G_2(s)G_3(s)H_{EXC}(s)}{G_3(s)G_6(s)H_{EXC}(s) + (1 + sG_3(s)T'_{do})}$$
(3.27)

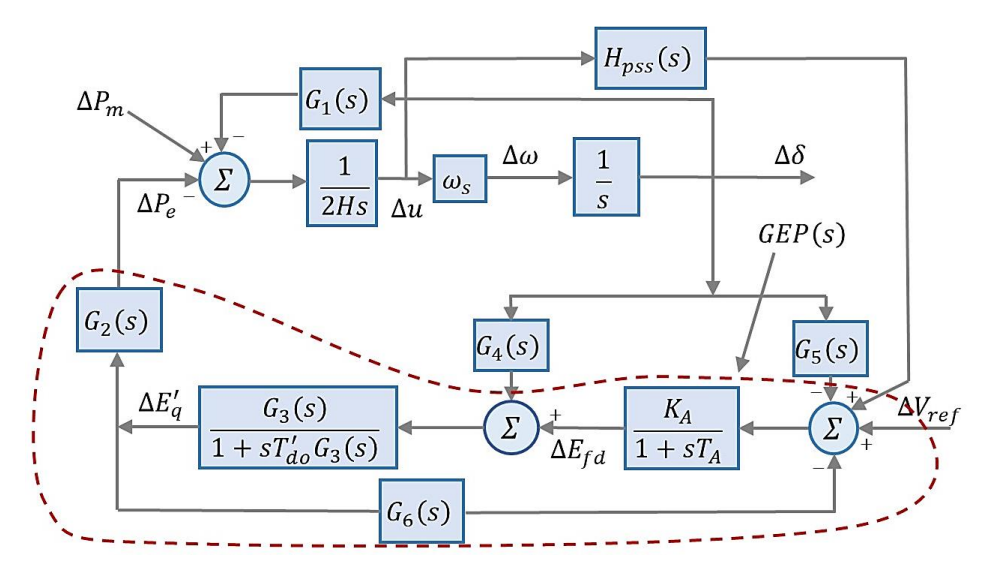


Figure 3.3 Modified Phillip Heffron Model

where $H_{EXC}(s)$ is the transfer function of the exciter dynamics. The model of PSS is preferred to be a lead-lag type of compensator, as expressed in (3.28). This lead-lag compensator provides a sufficient phase lead to compensate for the phase lag of the feedback loop at a low-frequency EmOM.

$$H_{pss} = K_{pss} \left(\frac{sT_w}{1 + sT_w} \right) \left(\frac{1 + sT_1}{1 + sT_2} \right) \left(\frac{1 + sT_3}{1 + sT_4} \right)$$
(3.28)

All the parameters of the PSS as given in (3.28), accord with the standard notations in [79]. The PSS tuning steps referenced in Algorithm 1 ensure sufficient damping for the critical EmOM. The difference between the tuning guidelines mentioned in [86] and those outlined in Algorithm 1 is that instead of constant parameters for the Heffron–Phillips model, here $G_1(s) - G_6(s)$ is used, which is a function of 's'. Power electronic converters control nearly 30% of the total electric power generation from DFIG-based wind technology. The rest of the power is directly fed to the grid through the DFIG stator, which is controlled by a mechanically rotated wind turbine. During electrical faults, the mechanical power available at the input of DFIG is in surplus to the electrical power available at its terminal. Thus, during a fault, a rotor oscillation event is triggered due to a sudden mismatch between demand and supply. The proposed PSS with a proper VIC gain (K_{inert}) setting, as demonstrated in this study discussed in the result section, can stabilize the system by extracting kinetic energy stored in the rotor of the DFIG. Therefore, in a frequency excursion event,

even if there is no energy storage device installed in the WES, the drivetrain will not have any additional strain.

3.5 Effect VIC and PLL on Synchronizing and Damping Torque

To assess the dynamic effects of the DFIG on the damping of the SG, it is necessary to determine the ΔP_g in terms of $\Delta \delta$ and $\Delta \omega$ as a function of the VIC and PLL parameters. This can be accomplished by further constructing $\Delta E_q'$ in terms of $\Delta \delta$ and $\Delta \omega$. The relationship of $\Delta E_q'$ to

Algorithm 1 Tuning of the proposed PSS parameters

Input: All data related to SG, VIC, PLL

- 1: Obtain $K_1 K_6$ from the classical Heffron–Phillips model.
- 2: Obtain the functions of $G_1(s) G_6(s)$ from the modified Heffron-Phillips model using (3.26) and Appendix A. 2.
- Neglecting damping from all other sources, obtain undamped natural frequency (ω_n) from torque angle loop presented in Figure 3.3.
- 4: Obtain the phase lag of GEP(s) of (3.27) at $s = j\omega_n$.
- 5: Set the phase lead of $H_{pss}(s)$ in (3.28) such that

$$\angle H_{pss}(s)|_{s=j\omega_n} + \angle GEP(s)|_{s=j\omega_n} = 0$$

6: Obtain the instability PSS gain K_{pss}^c from the root locus plot of the system, including PSS, and then set

$$K_{pss} = \frac{K_{pss}^c}{3}$$

Output: Parameters of the proposed PSS are obtained.

 $\Delta\delta$ and $\Delta\omega$ can be evaluated similarly as in [87] and represented as

$$\Delta E_q'(s) = \Lambda_{avr}(s)\Delta\delta + \Lambda_{pss}(s)\Delta\omega \tag{3.29}$$

where

$$\Lambda_{avr}(s) = \frac{-[G_4(s) + G_5(s)H_{EXC}(s)]G_3(s)}{G_3(s)G_6(s)H_{EXC}(s) + (1 + sG_3(s)T'_{do})}
\Lambda_{pss}(s) = \frac{-G_3(s)H_{pss}(s)H_{EXC}(s)}{G_3(s)G_6(s)H_{EXC}(s) + (1 + sG_3(s)T'_{do})}$$
(3.30)

Next, by substituting (3.29) into (A. 13) of Appendix A. 2, the change in generator output power can be expressed as

$$\Delta P_g = [G_1(s) + G_2(s)\Lambda_{avr}(s)]\Delta\delta + G_2(s)\Lambda_{pss}(s)\Delta\omega$$
 (3.31)

As this study focuses on low-frequency oscillations up to < 3 Hz, it can be assumed that $G_4(s)$ has a negligible impact on $\Lambda_{avr}(s)$ [88]. With the usual range of generator constants and the tuning process of the AVR and PSS [87], the $\Lambda_{avr}(s)$ and $\Lambda_{pss}(s)$ could be approximated to that of [88] as

$$\Lambda_{avr}(s) \approx \frac{-G_5(s)}{K_A K_6} \frac{H_{exc}(s)}{\left(1 + s \frac{T'_{do}}{K_A K_6}\right)}$$

$$\Lambda_{pss}(s) \approx \frac{-H_{exc}(s) H_{pss}(s)}{K_A K_6 \left(1 + s \frac{T'_{do}}{K_A K_6}\right)}$$
(3.32)

Then, with the replacement of $\Lambda_{avr}(s)$ and $\Lambda_{pss}(s)$ from (3.32) into (3.31), ΔP_g for EMI can be expressed in the form of (3.16) as

$$\Delta P_g \big|_{S=\lambda_c + \Delta \lambda_c} = P_S \Delta \delta + P_D \Delta \omega \tag{3.33}$$

where

$$P_S = G_1(s) - \frac{G_2(s)G_5(s)H_{exc}(s)}{K_A K_6 \left(1 + s \frac{T'_{do}}{K_A K_6}\right)}$$
(3.34)

$$P_D = \frac{-G_2(s)H_{exc}(s)H_{pss}(s)}{K_A K_6 \left(1 + s \frac{T'_{do}}{K_A K_6}\right)}$$
(3.35)

From (3.34) and (3.35), it can be seen that the synchronizing/damping coefficients (P_S/P_D) are mostly affected by $G_2(s)$ and $G_5(s)$. The $\Delta\lambda_c$ in (3.33) represents the change in EMI derived from the VIC and PLL dynamics of the DFIG. Next, all the parameters and functions without an inertia

controller and PLL are obtained, which are marked with " (Λ) ." With this property, (3.33) can be rewritten as

$$\Delta P_g \big|_{S=\lambda_C + \Delta \lambda_C} = (\hat{P}_S + \Delta P_S) \Delta \delta + (\hat{P}_D + \Delta P_D) \Delta \omega$$
 (3.36)

where \hat{P}_S/\hat{P}_D are the synchronizing/damping coefficients, respectively, for the case without a PLL and VIC. Thus, for the mode of interest λ_c , \hat{P}_S/\hat{P}_D can be expressed as

$$\widehat{P}_{s}\big|_{s=\lambda_{c}} = K_{1} + K_{2}\widehat{\Lambda}_{avr}(s)
\widehat{P}_{D}\big|_{s=\lambda_{c}} = K_{2}\widehat{\Lambda}_{pss}(s)$$
(3.37)

where $\widehat{\Lambda}_{avr}(s)/\widehat{\Lambda}_{pss}(s)$ indicate changes in the AVR/PSS transfer functions, respectively. In addition, from (3.32), the relationship between Λ and $\widehat{\Lambda}$ can be described as

$$\Lambda_{avr} = \hat{\Lambda}_{avr} \left(1 + \frac{\Delta K_5(s)}{K_5} \right)$$

$$\Lambda_{pss}(s) = \hat{\Lambda}_{pss}(s)$$
(3.38)

When (3.38) is substituted into (3.31), ΔP_g can be rewritten as

$$\begin{split} \Delta P_g &= \left[\left(K_1 + K_2 \hat{\Lambda}_{avr}(s) \right) \Delta \delta + K_2 \hat{\Lambda}_{pss}(s) \Delta \omega \right] \left(1 + \frac{\Delta K_2(s)}{K_2} \right) \\ &+ \left[\left(G_2(s) \frac{X_{L1} M_{en}}{X_1 M_{vv}} \hat{\Lambda}_{avr}(s) - K_1 \right) \left(\frac{\Delta K_2(s)}{K_2} \right) + \Delta K_1(s) \right] \Delta \delta \end{split} \tag{3.39}$$

where M_{vv} is defined as

$$M_{vv} = V_{no}X_{L1}\cos\theta_{po} + V_tX_{L2}\cos(\theta_{t0} - \theta_{p0})$$

As highlighted in [86] and [87], with a high AVR gain, both the AVR and PSS offer constant contributions to the synchronizing/damping coefficients for a small change in eigenvalues (i.e., $\lambda_c \to \lambda_c + \Delta \lambda_c$). With this property, (3.39) can be expressed as

$$\Delta P_g \big|_{s=\lambda_c} \approx \Delta P_g \big|_{s=\lambda_c + \Delta \lambda_c}$$
 (3.40)

Equation (3.39), therefore, becomes

$$\Delta P_g \big|_{s=\lambda_c} = \hat{P}_S \Delta \delta + \hat{P}_D \Delta \omega + (P_{Sa} \Delta \delta + P_{Da} \Delta \omega) \frac{\Delta K_2(s)}{K_2}$$
(3.41)

where

$$\begin{cases} P_{Sa} = \hat{P}_{S} + \frac{X_{L1}M_{en}}{X_{1}M_{vv}} P_{S,avr} + \frac{E'_{qo}V_{P}}{X_{1}} cos(\delta_{0} - \theta_{p0}) - K_{1} \\ P_{Da} = \hat{P}_{D} + \frac{X_{L1}M_{en}}{X_{1}M_{vv}} P_{d,avr} \end{cases}$$
(3.42)

The $P_{s,avr}$ and $P_{d,avr}$ are synchronizing and damping contributions from $K_2\widehat{\Lambda}_{avr}(\lambda_c)$. For the mode of interest, (3.41) implies that

$$\Delta P_S \Delta \delta + \Delta P_D \Delta \omega = (P_{Sa} \Delta \delta + P_{Da} \Delta \omega) \frac{\Delta K_2(\lambda_c)}{K_2}$$
(3.43)

Based on (3.25) and (3.26), the following is derived:

$$\frac{\Delta K_2(s)}{K_2} = \frac{E'_{qo} X_{L2} \cos(\delta_0 - \theta_{p0})}{M_{en}} D(s)$$
 (3.44)

Thus, at the mode of interest $(\lambda_c = \sigma_c + j\omega_c)$, the D(s) of (3.44) can be expressed as

$$D(s)|_{s=\lambda_c} = D_R + jD_I \tag{3.45}$$

If it is assumed that $\sigma_c \ll \omega_c$ such that $\lambda_c \approx j\omega_c$, the exclusive expressions of D_R and D_I are

$$\begin{cases}
D_{R} = \frac{-K_{inert}K_{I,pll}\omega_{c}^{2}A - K_{inert}K_{I,pll}\omega_{c}^{3}B}{A^{2} + B^{2}} \\
D_{I} = \frac{K_{inert}K_{I,pll}\omega_{c}^{2}B - K_{inert}K_{I,pll}\omega_{c}^{3}A}{A^{2} + B^{2}}
\end{cases} (3.46)$$

where *A* and *B* are expanded to:

$$\begin{cases}
A = \frac{2\pi V_{po} M_{en}}{X_1 X_{L2}} \left(K_{I,pll} - \omega_c^2 \right) - K_{inert} K_{I,pll} \omega_c^2 \\
B = \frac{2\pi V_{po} M_{en}}{X_1 X_{L2}} K_{P,pll} \omega_c - K_{inert} K_{p,pll} \omega_c^3
\end{cases}$$
(3.47)

Based on (3.43) - (3.45), ΔP_S and ΔP_D can ultimately be represented as in (3.48).

$$\begin{cases}
\Delta P_{S} = \frac{E'_{qo}X_{L2}\cos(\delta_{0} - \theta_{p0})}{M_{en}(A^{2} + B^{2})} \begin{pmatrix} (P_{da}K_{P,pll}\omega_{c}^{2} - P_{sa}K_{I,pll})K_{inert}\omega_{c}^{2}A - \\ (P_{sa}K_{P,pll} + P_{da}K_{I,pll})K_{inert}\omega_{c}^{3}B \end{pmatrix} \\
\Delta P_{D} = \frac{E'_{qo}X_{L2}\cos(\delta_{0} - \theta_{p0})}{M_{en}(A^{2} + B^{2})} \begin{pmatrix} -(P_{da}K_{I,pll} + P_{sa}K_{P,pll})K_{inert}\omega_{c}^{2}A + \\ (P_{sa}K_{I,pll} - P_{da}K_{P,pll}\omega_{c}^{2})K_{inert}\omega_{c}B \end{pmatrix}
\end{cases} (3.48)$$

Thus, the changes in synchronizing and damping coefficients as derived in (3.48) are the functions of damping frequency ω_c , the VIC and PLL parameters, and synchronizing/damping coefficients from the no-wind integration case (\hat{P}_S/\hat{P}_D) . According to (3.48), as K_{inert} increases to a non-zero value, a shift occurs in the mode of interest (i.e., $\Delta\lambda_c$), and the wind power inertial controller participates in damping and synchronizing torque.

3.6 Result and Analysis

The analytical results based on the above methodology have been tested on two different systems: (a) the SMIB system and (b) the IEEE 9 bus test system.

3.6.1 SMIB System

The outcomes described in the previous section were validated through an SMIB test system, as shown in Figure 3.1.

3.6.1.1 Effects of Variations in K_{inert} on ΔP_S and ΔP_D

 ΔP_S and ΔP_D were studied under different values of K_{inert} . The ΔP_S and ΔP_D curves inherited from (3.48) were validated against those obtained from (3.31), which consisted of exact expressions of AVR and PSS contributions. The parameters of the generator and AVR are presented in Appendix A. 3. The wind farm installed at bus 3 of the SMIB, as shown in Figure 3.1, consisted of 22 DFIGs at a 3.6 MVA rating and were connected in parallel. The wind farm was aggregated into a single DFIG for small-signal analysis. The parameters of the PLL used for synchronization purposes of the DFIG, where $K_{P,pll} = 0.01$ and $K_{I,pll} = 0.1$. The remainder of the data related to the SG, transformer, and DFIG are presented in Table A. 1 and Table A. 2. It should be noted that the change in the position of DFIG integration in the SMIB system, as marked in Figure 3.1, could result in changes to line reactance X_{L1} and X_{L2} . Equation (3.48) presents the effects of line reactance on the variations in synchronizing and damping torque of the SG. Under these conditions, the study was conducted with DFIGs installed at (a) Location 1: $X_{L1} = 0.05$ p. u.,

 $X_{L2}=0.15$ p. u. with the proposed PSS1 and at (b) Location 2: $X_{L1}=0.15$ p. u., $X_{L2}\coloneqq 0.05$ p. u. with the proposed PSS2. Figure 3.4 shows the effects of the location of the DFIG equipped with a VIC and PLL on the synchronizing and damping torque (ΔP_S and ΔP_D) of the SG. It can be observed that, the characteristics of ΔP_S and ΔP_D , was the similar for the critical socillating mode, λ_c in both cases. With the same data used in Location 1, the initial operating conditions of the system evaluated from load-flow studies as, $P_{g0}=1$ p.u., $P_{w0}=0.88$ p.u., $V_t=1 \angle 0.3398$ p.u., $V_{p0}=0.9887 \angle 0.2893$ p.u., and $V_{n0}=1 \angle 0$ p.u.. Similarly, the operating conditions of Location 2, where $P_{g0}=1$ p.u., $P_{w0}=0.88$ p.u., $V_t=1 \angle 0.2462$ p.u., $V_{p0}=0.9938 \angle 0.0947$ p.u., and $V_{n0}=1 \angle 0$ p.u..All p. u. values were based on 100 MVA. The parameters of the proposed PSS1 and PSS2 were tuned according to Algorithm 1, and the parameters obtained are presented in Table 3.1. The characteristic curves of $\Delta P_S/\Delta P_D$ versus K_{inert} are demonstrated in Figure 3.4. The degree of mismatch observed in Figure 3.4 can be due to certain assumptions used to derive (3.48). Note that the discrepancies in the results as obtained from the approximated exp-

Table 3.1: PSS Parameters for Locations 1 and 2

PSS	K_{pss}	T_w	<i>T</i> ₁	T_2	T_3	T_4
Proposed PSS1	62	10	0.2	0.02	0.1	0.52
Proposed PSS2	40	10	0.2	0.02	0.1	0.64

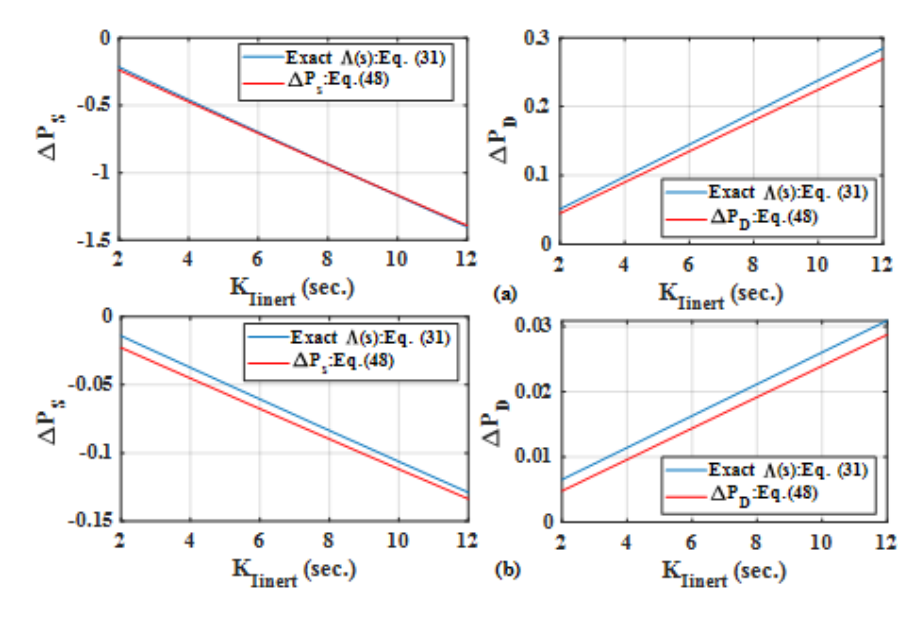


Figure 3.4 Change in ΔP_S and ΔP_D for (a) location 1, Prop. PSS1 (b) Location 2, Prop. PSS2

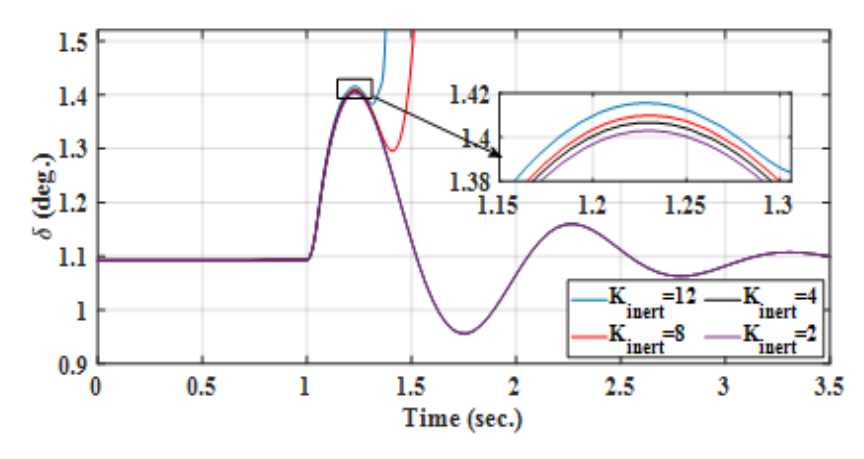


Figure 3.5 Dynamic response for different values of K_{inert}

ression in (3.48) and the exact expressions in (3.29) - (3.31) could be ignored, as this study focused on the nature and properties of the interaction between the wind farm with an inertial controller and the SG. Figure 3.4 shows that the increase in K_{inert} could adversly affect ΔP_S , as, can be seen that at a certain large value of K_{inert} , the ΔP_S may has become negative, which must be avoided to ensure the rotor angle stability of the system. In contrast to ΔP_S , the behavior of ΔP_D increased with K_{inert} . As expected, it can be concluded from Figure 3.4 (a) and (b) that the interaction between the wind farm and SG was more prominent when the wind was nearer to the SG, i.e., Location 1, and the effect diminished as it moved to a more remote location, i.e., Location 2. The aforementioned observations were validated through a time-domain simulation performed in MATLAB 2019b for the system shown in Figure 3.1. The SG and AVR parameters used in the simulation are presented in Appendix A. 3. The line parameters were chosen to be the same as for Location 1. A wind farm consisting of 22 DFIGs, each DFIG with a rating of 3.6 MW, was integrated into the system at bus 3. Data for each DFIG are provided in Appendix A. 3. The simulation of the inertial loop of the VIC consists of a rate limiter and low-pass filter to remove the noise from the frequency error signal, which was not modeled for the aforementioned mathematical analysis. This research evaluated the power system's damping as derived from DFIG integration while considering VIC and PLL dynamics. More specifically, DFIG integration into the power system affected the damping and synchronizing torque of the SG. Thus, in this chapter, the wind speed was treated as the average of the various wind speeds. Therefore, this work assumes that the wind velocity and, thus, wind power output were constant. The PLL parameters were set to $K_{P,pll}=0.01$ and $K_{I,pll}=0.1$ as mentioned above. The PSS parameters were chosen from Table 3.1 for Location 1 of the wind farm. Time-domain simulation results of the load angle curve of the system for a three-phase fault applied between the PCC and infinite bus at 1 sec. are shown in Figure 3.5. The system load angle curve was observed for different values of K_{inert} . Figure 3.5 shows that an increase in K_{inert} have deteriorated the system rotor angle stability.

3.6.1.2 $\Delta P_D/\Delta P_S$ versus CPSS and Proposed PSS

To demonstrate the effects of the proposed PSS and CPSS on changes in ΔP_D , the proposed PSS for Location 1 was designed according to the steps outlined in Algorithm 1. The CPSS parameters were tuned without considering the effects of the VIC and PLL. The modified Heffron-Phillips model was derived considering the wind farm placement. To design the proposed PSS for the SG, the PSS parameters were chosen as $T_1 = 0.2$ sec., $T_2 = 0.02$ sec., and $T_3 = 0.1$ sec., which is in the standard range of 0.02 to 0.2. The T_4 was inferred from the phase-lagging information of GEP(j ω_n). In this case, the undamped natural frequency was obtained as ω_n = 8.03 Hz, with damping from all other sources being neglected. For the given ω_n , T_4 is obtained as 0.52 sec. Then, K_{pss} was derived from the root locus diagram considering the dynamics of the full system. The root locus of the system is presented in Figure 3.7. According to the root locus diagram, the critical value of PSS gain is $K_{pss}^{cr} = 185$. Thus, in accordance with Step 4 of Algorithm 1, it follows, $K_{pss} = 62$. Figure 3.6(a) and (b) represents the changes in ΔP_S and ΔP_D with respect to K_{inert} for the proposed PSS and CPSS, respectively. The parameters of the CPSS and proposed PSS are presented in Table 3.2. Figure 3.6 shows that the proposed PSS significantly improved the damping contribution from wind farms over that of the CPSS with respect to the complete range of K_{inert} . These observations were validated through a time-domain simulation developed in MATLAB 2019b of the given system with $K_{inert} = 4$. A three-phase fault was applied at 1 sec. between the PCC and infinite bus. The fault response of load angle curve " δ " as

Table 3.2: Parameters of Proposed PSS and CPSS

Type of PSS	K_{pss}	T_w	T_1	T_2	T_3	T_4
Proposed PSS	62	10	0.2	0.02	0.1	0.53
CPSS	30	10	0.2	0.02	0.1	0.42

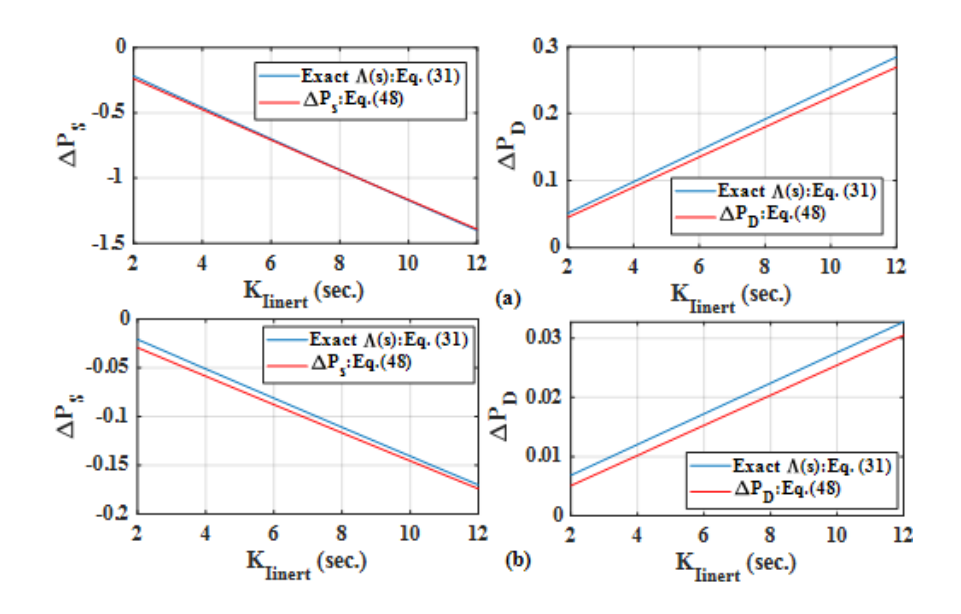


Figure 3.6 Change in ΔP_S and ΔP_D for (a) Proposed PSS. (b) CPSS

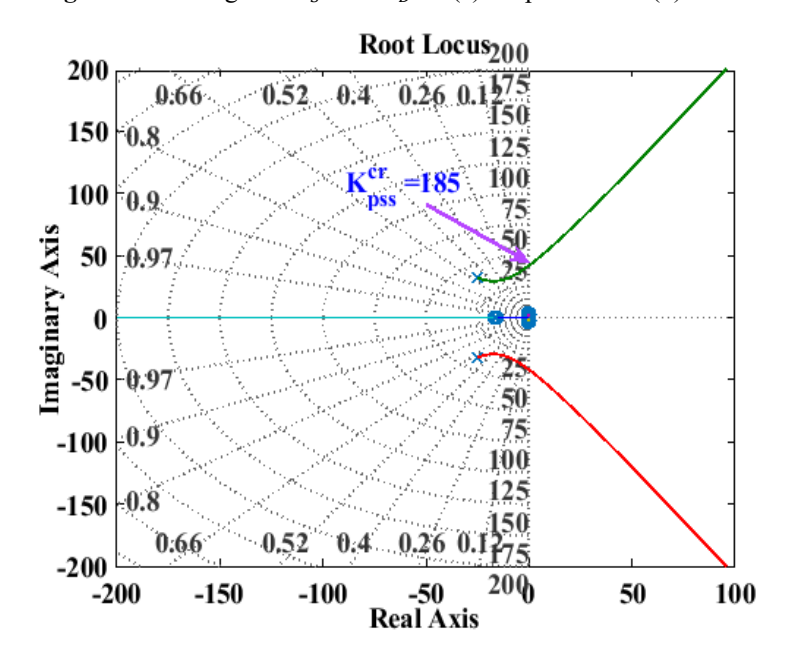


Figure 3.7 Root locus of SG

shown in Figure 3.8, clearly revealed that the proposed PSS exhibited very impressive damping characteristics over those of the CPSS.

The system response under fast dynamic conditions is shown in Figure 3.5 and Figure 3.8 for the SMIB system under the application of a three-phase fault between the PCC and infinite bus. The figures conclusively show that the proposed PSS, which was designed to consider the effects of the VIC and PLL of the DFIG at a lower range of K_inert, exhibited impressive results as compared

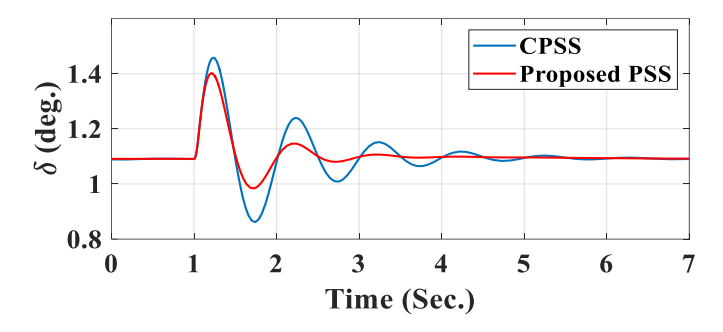


Figure 3.8 Simulation result of fault response of proposed and conventional PSS

with the CPSS. The infinite bus is considered an ideal voltage source with no internal impedance. However, as Figure 3.1 shows, the line impedance connected between the PCC bus and the infinite bus was X_{L2} . Based on (3.48), X_{L2} is one of the function parameters of ΔP_S and ΔP_D . The effects of changes in X_{L2} were simulated by changing the location of the DFIG. Here, X_{L2} could be treated as grid impedance. This research consideres the two locational scenarios as Locations 1 and 2. Results under the two locations are presented in Figure 3.4-Figure 3.8. From these plots, it is concluded that when the DFIG was located near the SG, the interaction between the DFIG and SG was prominent in terms of improved synchronizing and damping torque. Alternatively, high grid impedance promoted better system stability.

3.6.2 Modified 9-bus Test System

The modified version of the IEEE 9-bus test system, as shown in Figure 3.9 had a wind farm installed at bus 7. All the parameters for the 9-bus test system were derived from [79] and are also presented in Appendix A. 5. A wind farm with 50 DFIG-based wind generators with stator side capacities of 1.5 MW each is assumed to be installed near generator 2.

3.6.2.1 Effects of variations in K_{inert}

In this research, a generator near the wind farm was identified for installing the PSS. The PLL of the rotor-side converter was set to $K_{p,pll} = 0.52$ and $K_{i,pll} = 17$. The exciter parameters for Generator 2 were replaced with a gain of 200 and a time constant of 0.02 sec. This subsection describes the effects of K_{inert} variations on small-signal stability. The effects of K_{inert} were evaluated considering the presence of conventional PSS and the proposed PSS. The parameters are listed in Table 3.3. A three-phase fault was applied on bus 5 at 5 sec. to observe the fast dynamic response for the variations in K_{inert} , where K_{inert} was varied from 2 to 12 sec. to consider the

plots of load angle of SG 2 (δ_2) and active power output from the wind farm (P_w) as shown in Figure 3.10. The plots of δ_2 and P_w in Figure 3.10 show significant disturbances due to the presence of system transients. Figure 3.10 clearly shows that a higher value of K_{inert} resulted in a greater amplitude of oscillation, which is not conducive to rotor-angle stability. By contrast, a lower value of K_{inert} ensures better system performance.

3.6.2.2 Effects of CPSS and Proposed PSS

The proposed PSS was designed according to the steps outlined in Algorithm 1, with $K_{inert} = 4$ for the VIC of the DFIG. With the phase compensation technique described in Algorithm 1, the time constants of the proposed PSS are obtained: T_1 =0.1 sec., T_2 =0.01 sec., T_3 =0.2 sec., and T_4 =0.02875 sec. According to the root locus plot in Figure 3.11, the critical gain was found to be $K_{pss}^{cr} = 761$. The K_{pss} was set to $K_{pss} = K_{pss}^{cr}/3 \approx 254$ considering some margin of stability [79]. The parameters of the CPSS and proposed PSS are listed in Table 3.3. The simulation results of the post-fault response of the wind farm's active power output (P_w) and load angle curve of Generator 2 (δ_2) are presented in Figure 3.12 for a three-phase fault applied at bus 5. The plots show significant disturbances under the presence of system transients. Also, it shows the performances of the proposed PSS and CPSS. From the results, it is evident that the proposed PSS significantly outperformed the PSS with the parameters listed in Table 3.3. The simulation results of the post-fault response of the wind farm's active power output (P_w) and load angle curve of Generator 2 (δ_2) are presented in Figure 3.12 for a three-phase fault applied at bus 5. The plots in Figure 3.12 show significant disturbances under the presence of system transients. Figure 3.12 shows the performances of the proposed PSS and CPSS. Figure 3.12 (a) and (b) clearly show that the proposed PSS significantly outperformed the CPSS.

Table 3.3: Proposed PSS and CPSS Parameters for G2 of Modified IEEE 9 Bus Test System

Type of PSS	K_{pss}	T_w	T_1	T_2	T_3	T_4
Proposed PSS	254	10	0.1	0.01	0.2	0.02875
CPSS	127	10	0.1	0.01	0.2	0.21610

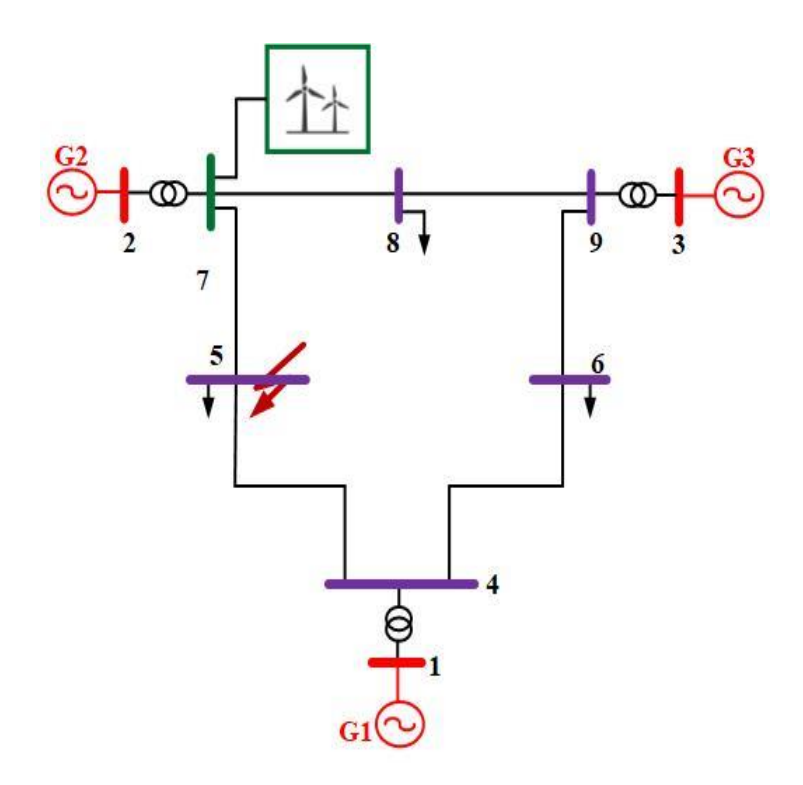


Figure 3.9 Modified IEEE 9 bus test system

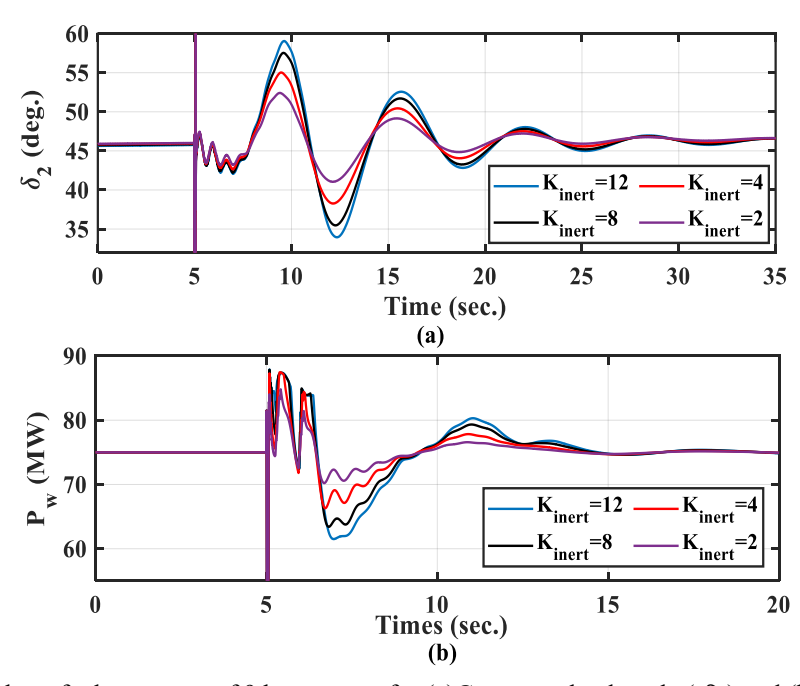


Figure 3.10 Three-phase fault response of 9 bus system for (a)Generator load angle (δ_2) and (b) Power output from WES, (P_w) with variation of K_{inert}

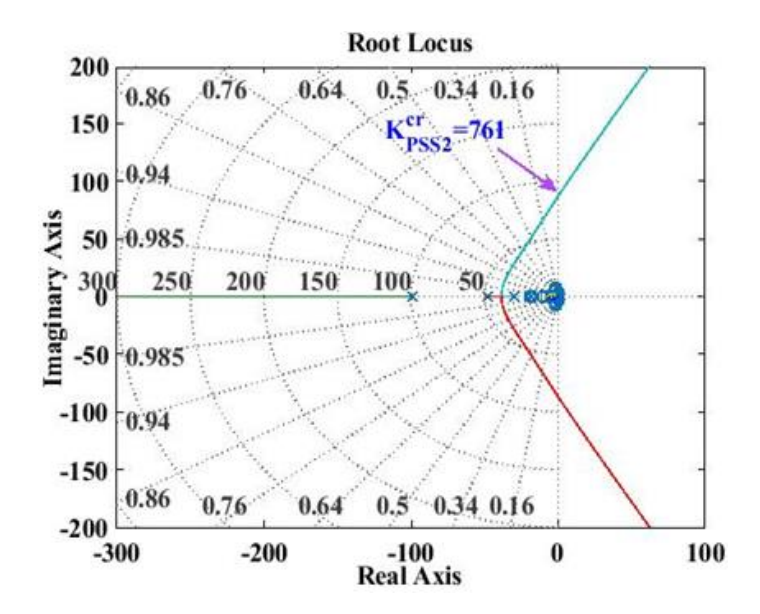


Figure 3.11 Root locus of Generator 2

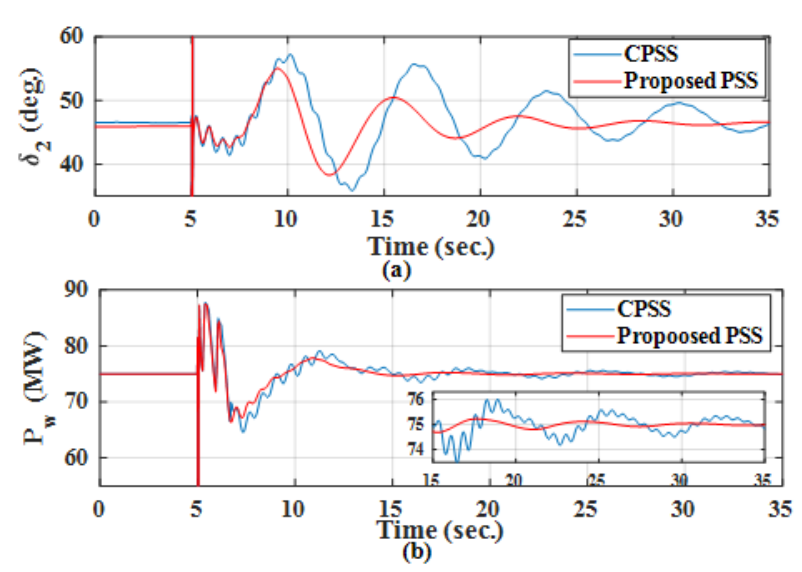


Figure 3.12 Simulation result of (a) Generator load angle (δ_2) and (b) Power output from WES, (P_w) for three-phase fault at bus 5 of 9-bus system

3.7 Conclusion

Existing power sectors have recently witnessed rapid growth in terms of wind power integration. As wind power is intermittent, a common practice has been to utilize VIC for frequency support. This chapter investigated the dynamic effects of VIC and PLL on the small signal stability of a power system. For this purpose, an average model of the DFIG-based wind farm was developed that incorporates VIC and PLL dynamics. An analytical formulation of damping and synchronizing coefficients was derived as functions of line reactance, K_{inert} , and PLL parameters. The significant coupling of the WES with the rest of the power system was

observed with the incorporated VIC and PLL dynamics. It was also found that the gain of the inertial controller contributes to power system stability by influencing the damping and synchronizing torque of the SG. The increase in value of virtual inertial gain (K_{inert}), reduced synchronizing torque but increased the damping torque of the system. Therefore, a system with high K_{inert} may lose synchronism. The study also revealed that the proposed PSS tuning method improved the power system's damping mechanism over that of CPSS. Thus, to improve the stability performance of a power system, the joint effects of the PLL and inertial controller of the DFIG must be considered in the design process of the PSS for the SG. The parameters of the proposed PSS were designed under a modified Heffron-Phillips model in a similar manner to that of the CPSS. However, more robustness could be obtained by applying some adaptive coordinated control methods. In this study, the parameters of the controllers were not optimized. Improved damping in the system could be achieved by considering advanced optimization techniques.

Chapter 4 Modal Sensitivity Analysis of Large-Scale PV-Integrated Power System Under System Uncertainties

This chapter evaluates the ranking of the generator bus by replacing each generator at a time with a similar rating of the Solar PV (SPV) system considering the various uncertain parameters like the probabilistic output of SPV, uncertainties of generator output, and load demand. The ranking of the buses is compared by widely used popular numerical Sensitivity Analysis (SA) techniques such as Sobol, Random Balance Designs Fourier Amplitude Sensitivity Test (RBD-FAST), Delta Moment-Independent Measure (DMIM), and Pianosi and Wagener (PAWN). Then, the inertial distribution among all the busses is investigated to find a suitable bus for Battery Energy Storage System (BESS) installation. The research has considered the BESS with a Virtual Inertia Controller (VIC). The PSS to be installed with the synchronous generators is identified by the Sensitive PSS Effect (SPE). The VIC gain and PSS parameters are tuned simultaneously by the Particle Swarm Optimization (PSO) optimization method.

4.1 Introduction

The transition of the power system has been expanding with large-scale integration of renewable sources driven by various factors, including overwhelming awareness of environmental concerns, technological advancement, and effective policy implementation. As technological breakthroughs ensure efficiency and cost-effectiveness, solar and wind-based renewable sources have gained worldwide acceptance as an alternative to fossil-based energy generation. The prime difficulties associated with these renewable sources are zero/low inertia and stochastic behavior of power injection into the main power grid. As a result, there will be serious consequences, such as the failure of the power system's stability. In previous chapters, the synchronizing/damping characteristics of DFIG-based WES are thoroughly investigated to propose a novel solution to improve the small signal stability of the power system. However, the research in this chapter investigates the small signal stability of power systems with large-scale integration of Solar PVs (SPVs), considering various uncertainties associated with SGs, loads, and SPVs. This chapter utilizes Global Sensitivity Analysis Techniques (GSATs) to account for the uncertainties. As mentioned in the literature survey of Chapter 1, the GSATs are reported in various areas of power systems like ranking of bus [59], design of PSS [60], voltage stability [61], and transient stability

[62]. However, in some recent publications, [61], [68] the GSATs are utilized to analyze the uncertainties that affect modern power systems' frequency stability/small signal stability.

The major contribution of this research addressing the objectives include

- (i) The ranking of generator buses of the given power system is obtained and compared based on the sensitivity outcome from four different GSATs named (a) Sobol Sensitivity Analysis, (b) Random Balance Designs Fourier Amplitude Sensitivity Test (RBD FAST), (c) Delta Moment, and (d) Pianosi and Wagener (PAWN).
- (ii) Comparison of the most important uncertain parameters affecting the critical mode is accomplished by four different GSATs.
- (iii) A VIC-based Battery Energy Storage System (BESS) is designed using the Particle Swarm Optimization (PSO) method to improve the small-signal stability of the systems.

4.2 Global Sensitivity Analysis Methods

Sensitivity analysis is crucial when a system is under the investigation of uncertain inputs and their influences on the uncertain output. Conducting sensitivity analysis involves propagating estimated uncertainties in the input parameters through the given model to be reflected in the output, ensuring a comprehensive exploration of the potential impact on the results. One of the processes of exploring this is utilizing Monte Carlo analysis, where the input uncertainties are derived from the estimated distribution function of the given input data. For example, if a system has uncertainties in 'n' nos. of input parameters. Introducing normal distribution function for each input, $\mathcal{N}(\bar{\mu}_j, \sigma_j)$, with j = 1, 2, ..., m samples on each of these parameters, the matrix of input uncertain estimated data sample can be formed as,

$$U_{in} = \begin{bmatrix} u_{11} & u_{12} & \dots & u_{1n} \\ u_{21} & u_{22} & \dots & u_{2n} \\ \vdots & \vdots & \ddots & \vdots \\ u_{m1} & u_{m2} & \dots & u_{mn} \end{bmatrix}$$
(4.1)

where $\bar{\mu}$ and σ are the mean and standard deviation of normally distributed data samples. Then, the given model is simulated using all the uncertain data samples to record the output as per the following format:

$$y = \begin{bmatrix} y_1 \\ y_2 \\ \vdots \\ y_m \end{bmatrix} \tag{4.2}$$

Having performed the Monte Carlo analysis, the sensitivity analysis can be carried out to explore the most crucial parameter that can influence uncertain resulted output. In this chapter, the outcomes of three different global sensitivities are compared. Details of the different global sensitivities are discussed in the following sections.

4.2.1 Sobol sensitivity analysis [89]

Sobol sensitivity analysis belongs to the category of variance-based methods, enabling the assessment of the influence of individual or interacting input parameters on the variability observed in the model's output [89]. Let the following form define a model:

$$y = g(u_1, u_2, u_3, ..., u_n) (4.3)$$

Sobol sensitivity indices belong to the decomposition of the variance of output y due to the influence of each input s_i (1st-order sensitivity, S_1) or due to the combined impact of more than one s_i (total sensitivity, S_T). The decomposition allows the model to be represented by

$$g(u_1, u_2, u_3, ..., u_n)$$

$$= g_0 + \sum_{k=1}^n g_k(u_k)$$

$$+ \sum_{1 \le k \le l \le n}^n g_{k,l}(u_k, u_l) + \dots + g_{1,2,...,n}(u_1, u_2, ..., u_n)$$
(4.4)

The terms of the decomposition can be defined as

$$g_{0} = \int g(u)du = E(y)$$

$$g_{k} = \int g(u) \prod_{q \neq k} du_{q} - g_{0} = E(y|u_{k}) - g_{0}$$

$$g_{k,l} = \int g(u) \prod_{q \neq k,l} du_{q} - g_{0} - g_{k}(u_{k}) - g_{l}(u_{l}) = E(y|u_{k}, u_{l}) - g_{0} - g_{k} - g_{l}$$

$$(4.5)$$

Eq. (4.5) satisfies,

$$\int_0^1 g(u_1, u_2, u_3, \dots, u_n) du_q = 0 \text{ for } q = 1, 2, 3 \dots n$$
(4.6)

Eq. (4.6) allows the following decomposition of variance as

$$V(y) = \sum_{k=1}^{n} V_i + \sum_{k} \sum_{k < l} V_{kl} + \dots + V_{1,2,\dots,n}$$
(4.7)

As a result, the sensitivity can be defined as:

$$S_T = \sum_{k=1}^n S_k + \sum_k \sum_{k < l} S_{kl} + \dots + S_{1,2,\dots,n} = 1$$
 (4.8)

The Sobol's 1st-order sensitivity can then be defined as

$$S_k = \frac{V(E(y|u_k))}{V(y)} \tag{4.9}$$

and 2nd-order Sobol sensitivities are represented as

$$S_{kl} = \frac{V(E(y|u_k, u_l)) - V_k - V_l}{V(y)}$$
(4.10)

The operator V in (4.9) and (4.10) indicates the variance of the given argument, whereas E denotes mean.

4.2.2 Random Balance Designs - Fourier Amplitude Sensitivity Test (RBD-FAST) [90]

The RBD-FAST is another variance-based sensitivity analysis method that can compute the robust and accurate 1st-order Sobol indices in a few hundred simulations, irrespective of the number of parameters [90]. The basic philosophy of this method involves:

- a) Partition the total uncertain input variable into groups of approximately equal input variables.
- b) Every group should be associated with a unique random permutation.
- c) Each group is assigned to a distinct frequency selected from a frequency set free of interferences up to a specified order.

For example, a n factor model may be associated with h groups, and each group is assigned with h distinct frequencies, such as $\omega_1, \omega_2, ..., \omega_h$. Now, the i^{th} factor of a group can be defined as

$$u_i(p_{ij}) = H_i(\sin \omega p_{ij}); \text{ for } i = 1, 2, ..., n, \text{ and } j = 1, 2, ..., m \text{ sample points}$$
 (4.11)

The function H_i is chosen according to the probability density function of the factor u_i . Then, the model output is obtained for each sample point as given in (4.12)

$$y_i(p_{ij}) = g(u_i(p_{ij}))$$
; for $i = 1, 2, ..., n$ and $j = 1, 2, ..., m$ sample points (4.12)

The resulting output is then re-processed according to the ascending order harmonics, and the sensitivity is determined by quantifying the Fourier spectrum of re-processed output.

4.2.3 Delta Moment Independent Measure (Borgonovo indices) [91]

The Delta Moment Independent Measure (DMIM) is one of the density-based sensitivity methods that can measure the importance of uncertainty of the input parameters, u_i , on the output, y, without considering the moment of y [91]. The influence of u_i 's distribution on distribution of y can be quantified by fixing u_i to u_i^* and allowing the remaining input parameters, \widetilde{u}_i , to vary. Then, the Borgonovo indices can be computed by considering the average of the estimation measure of the shift of area from un-conditional output distribution to conditional output distribution following the way

$$\delta_i(y, u_i) = \frac{1}{2} E[a(u_i)]; for i = 1, 2, ..., n$$
 (4.13)

where

$$a(u_{i}) = \int |f_{V}(y) - f_{V|u_{i}=u_{i}^{*}}(y)|du$$

$$E[a(u_{i})] = \int f_{u_{i}}(u) \left[\int |f_{V}(u) - f_{V|u_{i}=u_{i}^{*}}(y)|dy \right] du$$
(4.14)

In (4.14) $f_V(y)$ and $f_{V|u_i=u_i^*}(y)$ are the unconditional and condition output distribution, respectively. If the y is independent of u_i , then the output distribution will have no change for any value of u_i assumed to be u_i^* . Hence, $f_{V|u_i=u_i^*}(y)=f_V(y)$ and $\delta_i(y,u_i)=0$. On the other hand, if y is dependent upon the change in any input parameters, say $u_1,u_2,...,u_n$, then $\delta_{1,2,...,n}$ has any value between 0 and 1. The outer integral of (4.14) can be computed using a Monte Carlo-based integral around the range of u_i . Therefore, the computational cost to estimate Borgonovo indices

(δ) will be nmP, where n is the number of uncertain input parameters, m refers to the number of simulations required for outer integrals, and P is the required number of internal integrals.

4.2.4 PAWN Sensitivity Indices [92]

The sensitivity of the output of a system estimated by the PAWN sensitivity method considers the probability distribution of the system output rather than a particular moment of the output [92]. Therefore, the method is also known as moment-independent sensitivity analysis. To measure the sensitivity of the output (y) to a particular uncertain input (u_i) , the method quantifies the distance between the output distribution caused by unconditional input uncertainties and conditional uncertain inputs. The unconditional and conditional output distribution refer to the scenarios when uncertain inputs operate the system vary simultaneously and when the system operates with all the uncertain inputs except u_i , i.e., u_i is fixed by a known quantity, respectively. For PAWN sensitivity indexing, the output distribution function is quantified by the Cumulative Distribution Function (CDF) instead of the Probability Distribution Function (PDF). The difference between the unconditional and conditional output distributions is measured by the Kolmogorove-Smirnov statistic. Mathematically, the definition can be represented by:

$$T_i = \sup_{u_i} [F_y(y) - F_{y|u_i}(y)]; \text{ for } i = 1, 2, ..., n$$
 (4.15)

where $F_y(y)$ is the unconditional CDF of the system output, $F_{y|u_i}(y)$ is the conditional CDF of the output when u_i is fixed with a known value. The expression, $F_{y|u_i}(y)$ describes the impact of eliminating the variability associated with u_i on the distribution of y. The distance between, $F_{y|u_i}(y)$ and $F_y(y)$ serves as an indicator of the influence of u_i on y. The value of T_i varies between 0 and 1. The value of T_i equal to 0, referred to as the distribution, is non-influential by the input u_i and value of T_i closer to 1 indicates the out variation is highly influenced by the given input u_i . The different statistics between the distributions are accounted for by Min, Mean, Median, and Max across the slides/conditioning intervals, as well as the Coefficient of Variation (CV). However, the commonly indexed value is the median. In this chapter also, the PAWN index is reported by the median of the difference between the $F_{y|u_i}(y)$ and $F_y(y)$.

4.2.5 Sampling

One of the important steps for any sensitivity analysis is to organize the data samples to analyze how the input variation influences the system's output. This research utilizes the Saltelli sampling method to organize the input data samples by considering their probabilistic distribution. The Saltelli sampling technique is basically derived from Sobol's sensitivity analysis method [89]. The expression of sensitivity defined in (4.10) suggests that the total sensitivity is obtained by combining both 1st-order and 2nd-order sensitivity factors. To define the number of input data samples required to perform the total sensitivity analysis, let us define the 1st-order sensitivity further as

$$S_k = \frac{V(E(y|u_k))}{V(y)} = \frac{J_k - E^2(y)}{V(y)}$$
(4.16)

The term J_k can be further described as

$$J_k = \int E^2(y|u_k = \tilde{u}_k) \, p_k(\tilde{u}_k) d\tilde{u}_k; \quad k = 1, 2, ... \, n$$
 (4.17)

and the mean can be defined as

$$E(y) = \int \int \dots \int f(u_1, u_2, \dots u_n) \prod_{i=1}^{n} p_i(u_i) du_i$$
 (4.18)

The evaluation of the integral in (4.17) by the Monte Carlo simulation method may necessitate to solve n sets of m evaluations of f and similarly evaluation of the integral in (4.18) may require one set of m evaluations of f. In this way, the computation of the full set of first-order sensitivity S_k , need total m(n+1) of data samples. The m and n, are denoted as the sample size and number of uncertain input parameters, respectively. Similarly, the computation of total sensitivity S_T mentioned in (4.8) will need additional n sets of m evaluations of f, resulting in a total of 2m(n+1) numbers of data samples.

4.3 System Under Study and Uncertainties

In this section, the standard IEEE 39 bus-based New England Test System (NETS) has undergone all the sensitivity analysis studies discussed in the previous section for the following studies:

- a) Study of the SPV systems in place of the SGs
- b) Identify the most influential parameter of the modified IEEE 39 bus system

The elaborate representation of the above studies is discussed in the following sub-sections.

4.3.1 Study of the solar PV (SPV) systems in place of the SGs:

In the sensitivity analysis, each generator within the NETS, excluding the synchronous generators G1 and G2 (slack bus), was systematically replaced by an equivalent-rated SPV system. This replacement was conducted to evaluate how the introduction of SPV systems, individually and sequentially, affects the severity of the critical oscillatory mode compared to the original synchronous generators they were replacing. All the SGs were equipped with only AVR and IEEE Type1 exciter. None of the SGs were associated with a PSS. A total of 25 different uncertainties are considered for the given test system to facilitate the sensitivity studies using all the sensitivity analysis methods. The no. of samples is considered according to the Saltelli sampling method, as discussed in section 4.2. The value of m considered here is 1024. Hence, the total computational cost here is 54272. The uncertain parameters include stochastic variations in SPV, generation of all the SGs except G1 and G2 (slack bus), and loads.

- i. *Generators:* The test system (i.e., NETS) contains a total of 10 generators, and generator no.1 (i.e., G1) represents the aggregation of a large New York Power System (NYPS). Further, the G2 is considered a slack bus. Hence, the uncertainties associated with G1 and G2 are ignored. Therefore, the uncertainties belonging to G3-G10 are only considered for modeling, and the details are given in Table 4.1.
- ii. *Loads:* The NETS has a total of 19 loads. As the loads connected to buses 12 and 31 are 88.31 MVA and 10.28 MVA, compared to those connected to the rest of the buses, the load uncertainties are assumed to have less impact on the overall system performance. Hence, the uncertainties associated with those loads were ignored in the model. Therefore, a total of 17 load uncertainties were considered for the model. The modeling details of the loads are provided in Table 4.1.
- iii. *SPV Systems:* In the sensitivity analysis, as discussed above, the SGs were replaced once at a time by an equal-rated SPV. The uncertainties belonging to the SPV have been modeled with normal distribution, and its variances are mentioned in Table 4.1.

All the above-discussed uncertain parameters are inputted into each Global Sensitivity Analysis (GSA) method, and the system eigenvalues are the output parameters. The probabilistic Monte Carlo simulation has been used to analyze the sensitivity analysis. The flow chart of the sensitivity analysis performed by different GSA methods is provided in Figure 4.1. The figure shows the complete sensitivity analysis was conducted using DigSILENT by Power Factory and

Python. Initially, Python is utilized to define all the uncertainties, which are then interfaced with DigSILENT to conduct load flow and modal analysis for the samples of uncertain parameters generated from Python. This process continued until all the iterations of the Monte Carlo simulation ended. Then, the list of uncertain input samples and their corresponding resulting critical eigenvalues are provided as input for the given GSA methods to obtain the sensitivity of each uncertain input to the probabilistic distributed output. The probabilistic distribution of the da-

Table 4.1: Modeling of Uncertainties of Various Power System Components

Power system components	Generators	Loads	SPV systems
Distributions	Normal $(\pm 10\% \ var. \ of \ \mu)$	Normal $(\pm 10\% \ var. \ of \ \mu)$	Normal $(\pm 10\% \ var. \ of \ \mu)$

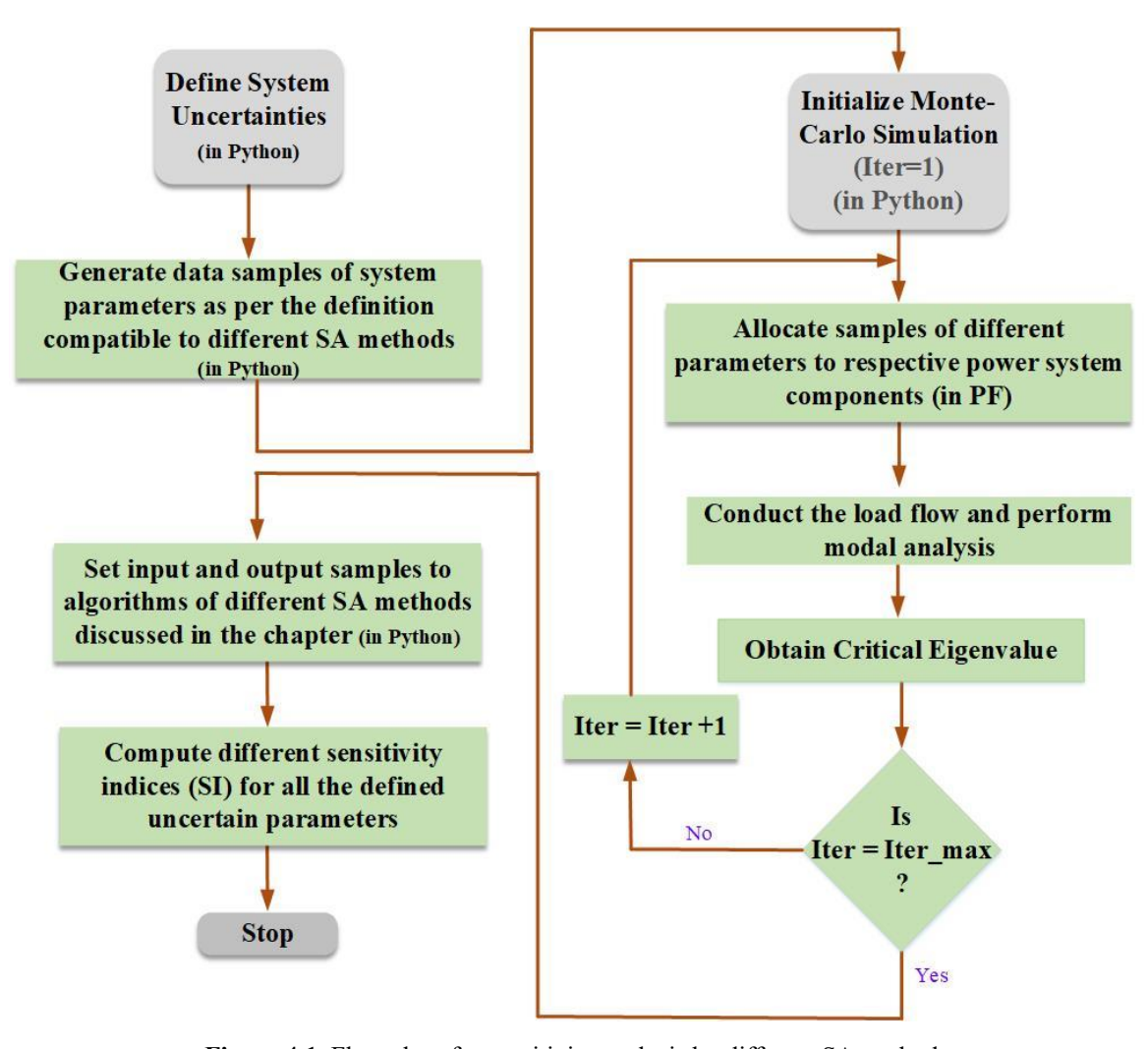


Figure 4.1 Flow chart for sensitivity analysis by different SA methods

mping ratio of the most critical eigenvalue resulting from the Monte Carlo simulation is shown in Figure 4.2. The overall impact of all the uncertain parameters is defined by the cumulative sensitivity index (SI_{cum}) . The SI_{cum} is resulted by considering the sum of 1st-order sensitivity of individual input parameters.

$$SI_{cum} = \sum_{a=1}^{n} S_a \tag{4.19}$$

where S_a indicates the 1st-order sensitivity of a^{th} stochastic input parameter obtained by all the GSA methods discussed earlier. The result of SI_{cum} of (4.19) due to the integration of SPVs in place are supposed to be replaced by SPVs as presented in Table 4.3. The ranking for each Sensitivity Analysis (SA) method is defined in such a way that the highest SI_{cum} refers to rank 1 and the reverse refers to rank 8. As it is observed from Table 4.3, the ranking of the generators obtained from different GSA methods does not match each other. However, the higher-ranked top four generators, i.e., G3, G6, G7, and G9, resulting from different GSA methods, have very good agreement. This indicates that the grid would experience a significant impact from the uncertain parameters of the power system if those generators were replaced by the identical-rated SPV syst-

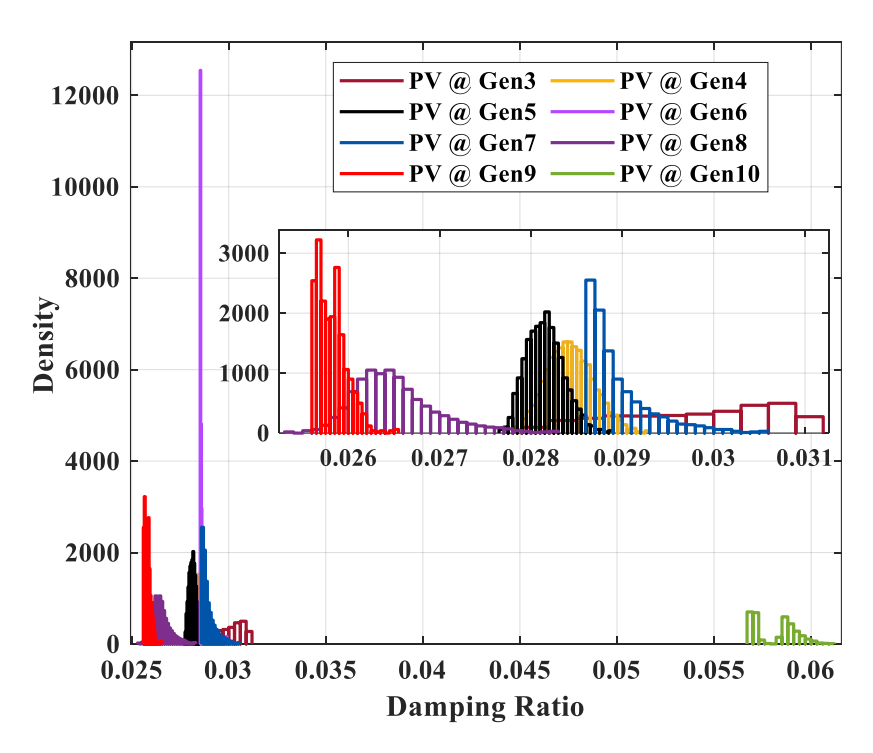


Figure 4.2 Probabilistic distribution of the damping ratio of most critical eigenvalue

Table 4.2: SI_{cum} of All Uncertain Parameters by Different SA Methods

SA Methods SPV @	Sobol	RBD-FAST	Delta	PAWN
G3	2.387025	0.503491	2.60537	7.796071
G4	1.35724	0.286452	1.90348	6.589632
G5	1.381363	0.307463	1.92528	6.987321
G6	2.648322	0.796277	2.735526	7.53203
G7	1.74387	0.523782	2.587431	7.098491
G8	1.451456	0.460785	2.442156	7.013791
G9	1.965372	0. 585431	2.620457	7.924003
G10	1.096601	0.472613	2.556236	6.410748

Table 4.3: Ranking of SGs to be Replaced by an SPV Considering System Uncertainties

	Name of the Sensitivity Analysis					
Ranking	Techniques					
of SGs	Sobol	RBD- FAST	Delta	PAWN		
1	G6	G6	G6	G9		
2	G3	G9	G9	G3		
3	G9	G7	G3	G6		
4	G7	G3	G7	G7		
5	G8	G10	G10	G8		
6	G5	G8	G8	G5		
7	G4	G5	G5	G4		
8	G10	G4	G4	G10		

em. Likewise, there is strong consensus among various sensitivity analysis methods regarding the less crucial generators, namely G4, G5, G8, and G10. This indicates that the ranking of the generators lying under the most crucial category (i.e., rank 1 to 4 of Table 4.3) obtained by different GSA methods are identical. Substituting these generators with SPV is likely to introduce signific-

Table 4.4: Electromechanical modes of the modified IEEE 39 bus NETS

Sl.no.	Modes	Damping Frequency	Damping Ratio
1	-0.10024 ± 4.25369	0.6769	2.4083
2	-0.6129 ± 8.49022	1.35126	7.2007
3	-0.35431 ± 7.4516	1.18595	4.74951
4	-0.25832 ± 6.23905	0.99297	4.1369

ant adverse effects on the grid, primarily caused by the uncertainties of the power system. Therefore, in the next section, the most influential uncertain parameters are identified for the modified IEEE standardized 39 bus NETS, where G3, G6, G7, and G9 are substituted by SPVs of similar ratings.

4.3.2 Identify the most influential parameter of the modified IEEE 39 bus system

Typically, the installation of PV systems is deemed appropriate in areas where there is abundant solar irradiance. However, in this research, to investigate the potential impact of SPVs as a substitute for SGs on the small signal stability of the power system, the decision has been made to replace generators G3, G6, G7, and G9 with equivalently rated SPVs. These generators are the most influential in the preceding section, as they have higher sensitivity of uncertain input to the most critical eigenvalue. In this section, the IEEE 39 bus NETS has been modified by substituting G3, G6, G7, and G9 with SPVs of equivalent rating. The modified IEEE 39 bus test system is shown in Figure 4.3. Given the data provided in [81] for the rest of the power system components of IEEE 39 NETS without PSS connected to any SG, the list of obtained eigenvalues through linearization at the initial operating point is presented in Table 4.4. As mentioned in the table, all the modes except mode 1 are the local oscillatory modes. Mode 1, whose damping frequency lies in the range of the inter-area mode of the frequency band, has the lowest damping ratio of the system. Hence, the oscillatory mode can be treated as the most critical for the given power system.

The prime focus of the section is to investigate the modified IEEE 39 bus test system to identify the most influential stochastic parameters that impact system stability by various GSA methods. A total of 25 uncertainties are dealt with for the given analysis. As highlighted in the preceding subsection, uncertainties in this context relate to loads, generators, and SPV systems. The uncertainties of the input parameters are modeled as normal distributions, as described in Table 4.1. The sensitivity indices obtained by different GSA methods are presented in Table 4.5.

and are derived according to the flow chart shown in Figure 4.1. The indices of Table 4.5 indicate the sensitivity of uncertainties of different system parameters under consideration to the change in the output of the system. The output of the system here is considered the most crucial eigenvalue, as presented in Table 4.4. As per the sensitivity results presented in Table 4.5, the three most sensitive input uncertain parameters to the change in the system's output are the power output from generator G5, PV_2 , and PV_3 as highlighted in the table. It is evident that the top 3 highly influential parameters identified by all four SA methods have good matching. In reality, the output of SPV systems is expected to vary more intermittently than the power output from G5. The summary of

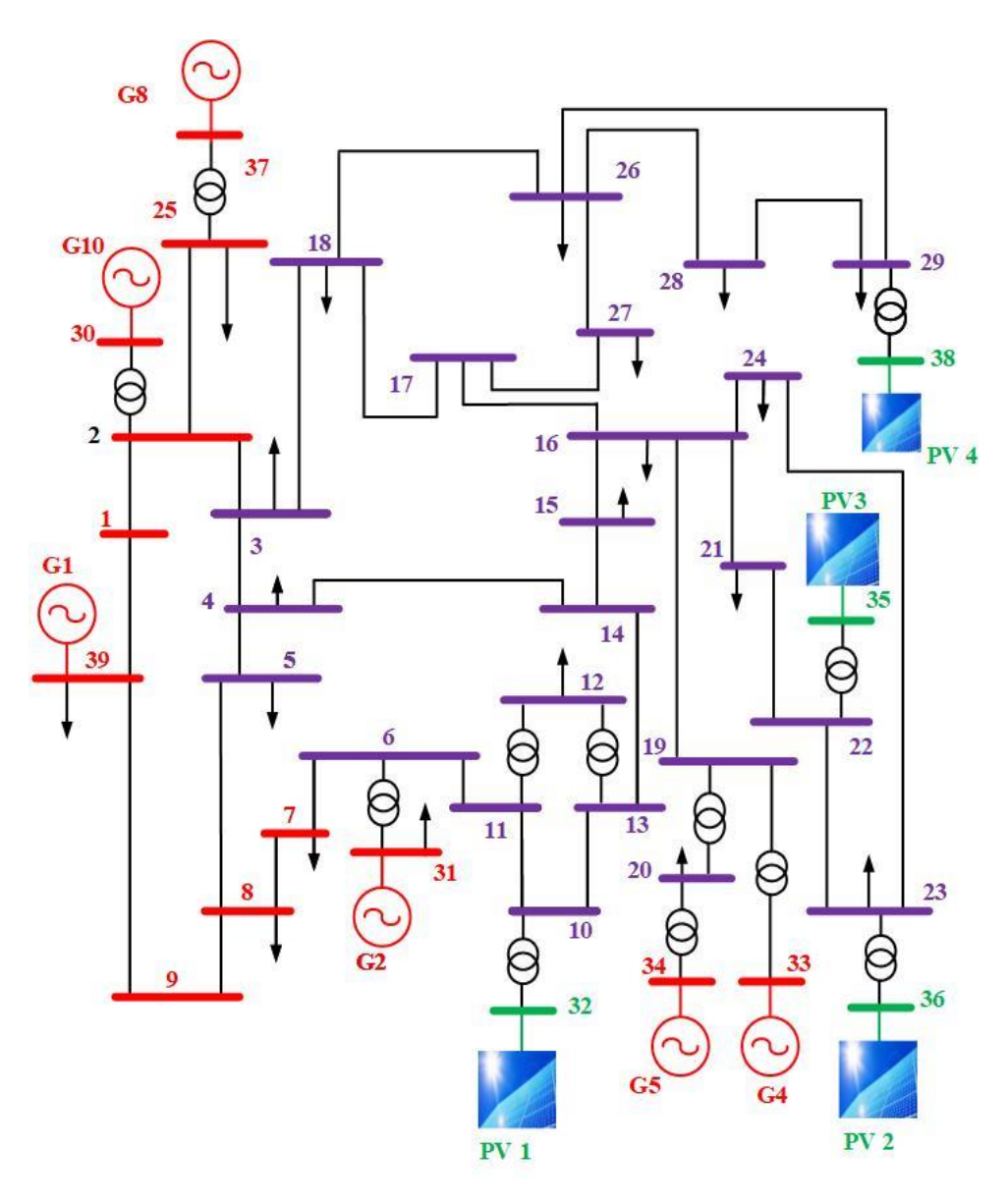


Figure 4.3 Modified IEEE 39 bus NETS

this subsection is that the various GSA methods rank the group of generators (G3, G6, G7, and G9) as crucial if replaced by the SPV systems of similar ratings. Further, the sensitivity analysis by different SA methods shows that the uncertain input parameters of the system, such as power out-

Table 4.5: Sensitivity of Different Uncertain Parameters Considered for the Modified IEEE 39 Bus System

Parameters	Nan	ne of different Sensi	tivity analysis me	thods
1 at affecters	Sobol	RBD-FAST	Delta	PAWN
Pv1	0.144447	0.010684223	0.139872	0.0994199
Pv2	0.564031	0.087693693	0.171178	0.165561
Pv3	0.549726	0.096755943	0.18903	0.187682
Pv4	0.315493	0.006461477	0.135502	0.0880387
PL3	0.0658955	0.00885694	0.147434	0.0627499
PL4	0.0917224	0.004992404	0.142615	0.0730644
PL7	0.0668444	0.002255826	0.142294	0.0704069
PL8	0.0689527	0.001929642	0.137548	0.0541003
PL15	0.107045	0.008068896	0.136009	0.0735608
PL16	0.144171	0.001466366	0.144876	0.0604409
PL20	0.342151	0.008748524	0.150836	0.114082
PL21	0.181447	0.003860279	0.153138	0.0647771
PL23	0.143471	0.011518852	0.138493	0.0934312
PL24	0.110041	0.002017981	0.13619	0.0648522
PL25	0.124505	0.008903336	0.142638	0.0770486
PL27	0.113611	0.005246082	0.137491	0.0736646
PL28	0.0997238	0.007900446	0.142585	0.0751708
PL29	0.080744	0.002361533	0.142288	0.0626575
PL39	0.188559	0.01134638	0.143617	0.0954848
G1	0.155768	0.004694353	0.136597	0.0935124
G4	0.225982	0.005093812	0.14113	0.0740508
G5	0.770507	0.187996871	0.261883	0.254866
G8	0.132171	0.014364291	0.147027	0.0816359
G10	0.18212	0.007434521	0.137809	0.0814631

put of G5, PV_2 , and PV_3 are the most sensitive parameters to the change in the most critical eigenvalue of the system.

4.4 Inertial Distribution of Modified NETS

The NETS has been modified by replacing the group of generators named G3, G6, G7, and G9 with the SPV of equivalent rating. This subsection aims to observe the distribution of inertia among the buses after a large-scale modification in terms of the replacement of synchronous generators with SPVs. Inertia distribution is the electrical distance of any bus to the location of Center of Inertia (COI) [93]. The electrical distance is evaluated from instant, t_0 sec., when the fault is applied, to over a period T and can be quantified by the following:

$$D_{k} = \lim_{N \to \infty} \sum_{i=1}^{N} (F_{k}(n_{i}) - F_{COI}(n_{i}))^{2} \cdot \Delta n$$

$$D_{index} = \frac{D_{k}}{\max_{k \in \{1, \dots, n_{b}\}} D_{k}}$$
(4.20)

where $\Delta n = T/N$, $n_i = t_0 + \Delta n$, $F_{COI} = \sum_{j=1}^{ng} (H_j f_j) / \sum_{j=1}^{ng} H_j$ and f_j is frequency of j^{th} generator and n_b denotes the total number of buses. From the above set of equations, the higher the value of D_k specifies the electrical distance between the k^{th} bus and COI is high. Therefore, the kth bus is located under a low concentration of inertia. Hence, the bus with a higher value of D_{index} refers to the larger electrical distance between the measured bus and COI. As the COI location may not exactly lie on any particular bus, the nearest bus can be identified with a lower D_{index} . The result of the inertial distribution of NETS is represented in Figure 4.4. It is observed from Figure 4.4 that the bus where PV_2 and PV_3 are installed have the highest D_{index} . According to [93], the bus with a higher D_{index} has a better damping effect on the critical oscillatory eigenvalue. Further, it can also be reviewed from the result of the previous subsection that the same PV buses, i.e., in PV_2 and PV_3 have the highest sensitivity to the movement of the most critical eigenvalue. Therefore, it can be assumed that a damping controller-enabled BESS, if placed at the location of PV_2 or PV_3 may exert a better damping phenomenon on the critically damped electromechanical oscillatory mode. Hence, in the rest of the chapter, the effort has been made to design a damping controller for BESS to be installed at the location of PV_3 .

4.5 Parameter Tunning of VIC-based BESS with PSS of SGs

Referring to the result discussed in the previous section, the bus B_{pv3} and B_{22} are expected to be the best locations for the installation of BESS to have a better damping phenomenon for the critical oscillatory mode, as the buses are located far away from the location of COI. Here, B_{pv3} denotes the bus where PV_3 has been installed. In this research, the BESS is equipped with a virtual inertia controller (VIC) and is installed at B_{22} . The control loop of VIC is shown in Figure 4.5. The fundamental idea behind the design of VIC is that the power reference change proportional to the change in system frequency is given as input to the BESS active power controller loop. The

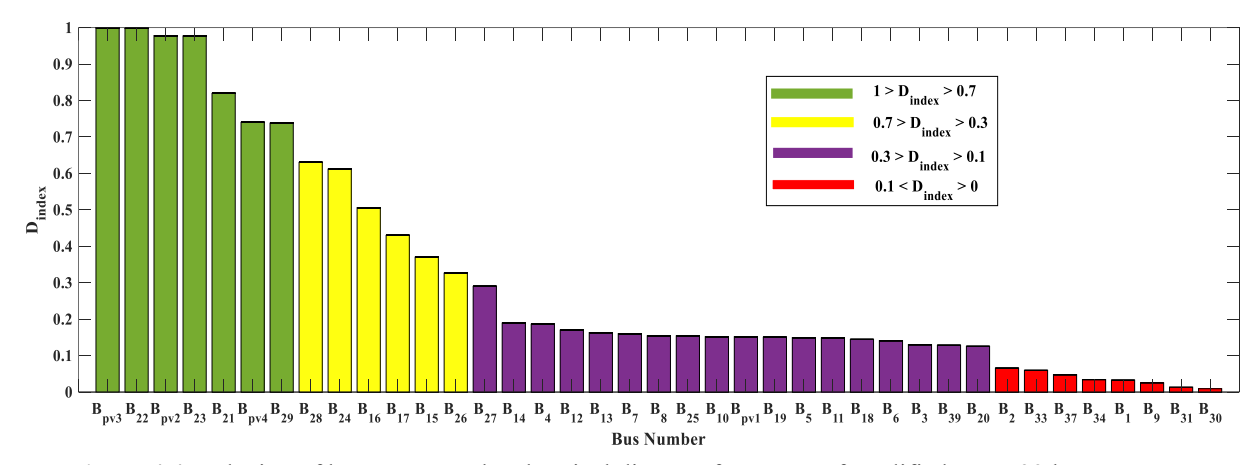


Figure 4.4 Indexing of busses as per the electrical distance from COI of modified IEEE 39 bus test system

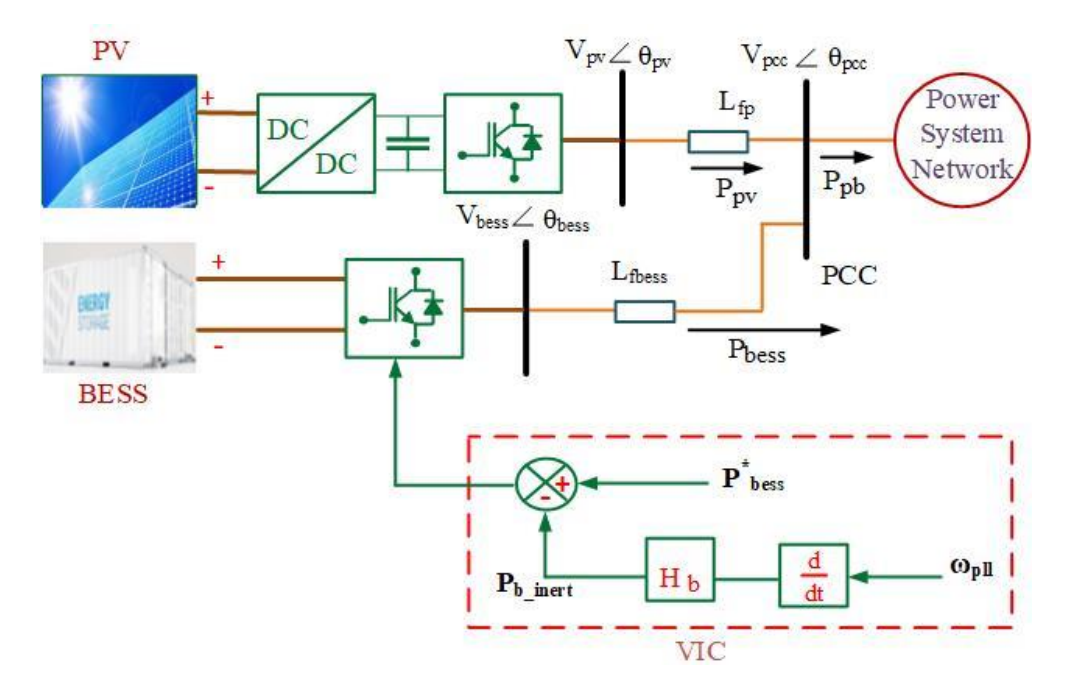


Figure 4.5 VIC Enabled PV-BESS system

details about the control loop of the PV-BESS system can be found in [94]. The PSSs to be installed with the remaining synchronous generators are identified by the Sensitive PSS effect (SPE) theory [95].

$$SPE = \varphi_{\Delta\delta_g} \psi_{\Delta E_f} \frac{K_a}{T_a} \tag{4.21}$$

where the $\varphi_{\Delta\delta_g}$ and $\psi_{\Delta E_f}$ are left and right eigenvectors corresponding to load angle and exciter field voltage deviation, respectively, for the given oscillatory mode. The K_a and T_a are the gain and time constant of the IEEE Type 1A exciter control loop. The SPE of each synchronous generator is represented in Table 4.6. The higher SPE indicates a suitable location for PSS to be installed. Hence, in this research, the PSS is installed at G4 and G5. The coordinated tunning of VIC gain and PSS parameters is conducted to minimize the following optimization problem:

$$minimize \begin{cases} Obj_1 = \sum_{i=1}^{N_g} \sum_{d_{i,j} \ge d_{req}} (d_{req} - d_{ij})^2 \\ Obj_2 = K_{inert} \end{cases}$$
(4.22)

Subject to:

$$\begin{split} K_{inert}^{min} & \leq K_{inert} \leq K_{inert}^{max} \\ K_{pss1}^{min} & \leq K_{pssi} \leq K_{pss1}^{max} \\ T_{1i}^{min} & \leq T_{1i} \leq T_{1i}^{min} \\ T_{2i}^{min} & \leq T_{2i} \leq T_{2i}^{min} \\ T_{3i}^{min} & \leq T_{3i} \leq T_{3i}^{min} \\ T_{4i}^{min} & \leq T_{4i} \leq T_{4i}^{min}, \quad i = 1,2 \end{split}$$

where d_{req} is the required damping value of the given no. of critical eigenvalues and d_{ij} is the obtained value of damping factors of j^{th} operating point corresponding to the i^{th} synchronous generator. K_{inert} is the inertia gain of the inertia controller of the BESS connected at B_{22} . The PSS parameters are represented by K_{pssi} , T_{1i} , T_{2i} , T_{3i} , and T_{4i} for i^{th} generator. The given problem

Table 4.6: SPE of Each Synchronous Generator

Generator	G2	G4	G5	G8	G10
SPE	0.00016	0.003	0.002	0.00002	0.00005

Table 4.7: Parameter of VIC and PSS

Parameters	Values	Parameters	Values
K _{inert}	0.018	T ₄₁	0.1482
K_{pss1}	0.028	T ₁₂	0.87
K_{pss2}	88	T ₂₂	0.02
T ₁₁	1.5	T ₃₂	0.4
T ₂₁	0.1395	T ₄₂	0.0296
T ₃₁	1.5		

formulation is solved by the PSO optimization method, and the parameters obtained from the solution are given in Table 4.7.

4.6 Results and Discussions

The optimized values of different parameters like inertia gain and PSS parameters obtained from PSO optimization are being tested on the modified NETS shown in Figure 4.3 for the time domain analysis. According to the SPE presented in Figure 4.4, the PSS has been chosen to be installed at G4 and G5. As per the Dindex results of Figure 4.4 suggests the VIC-based BESS is expected to exert better damping to the critical oscillatory modes if installed at B_{22} . Because B_{22} is located far from the location of COI. Given the above setting, the NETS is simulated to obtain the time domain response presented in Figure 4.6 and Figure 4.7. The plots are real power flow in L_{4-14} due to a three-phase fault created at L_{17-18} at 2 sec of the start of the simulation. Plots of the real power flow in L_{4-14} due to the three-phase fault created at L_{17-18} are exhibited in Figure 4.6. It shows the plots are taken for three cases: without BESS and PSS, with BESS and no PSS, and with BESS and PSS. Among all the results, it is evident that when no BESS or PSS is installed in the system, the post-effect of the three-phase fault appears oscillatory. However, the use of BESS at a suitable place, i.e., resulted as B_{22} , from the previous sections, the post-effect oscillations seem to be dampened out very quickly. In the case of both BESS and PSS in operation with optimally tuned parameters, there is significant damp-out of oscillations in the post-fault response of real power flow in L_{4-14} .

In Figure 4.7, the time domain response of the real power flow through line L_{4-14} are represented to witness the post-effect of the three-phase fault created at the line L_{17-18} due to the

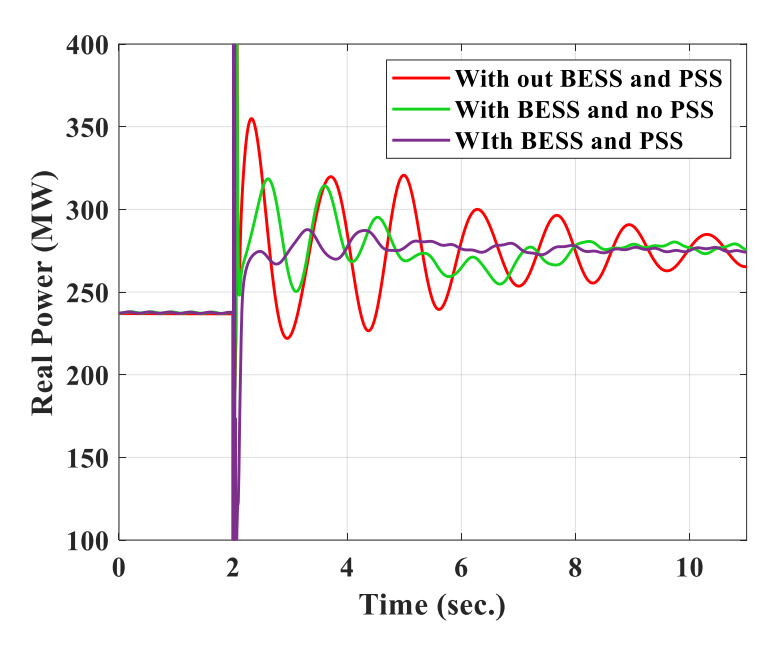


Figure 4.6 The real power flow of L_{4-14} due to BESS at B_{22}

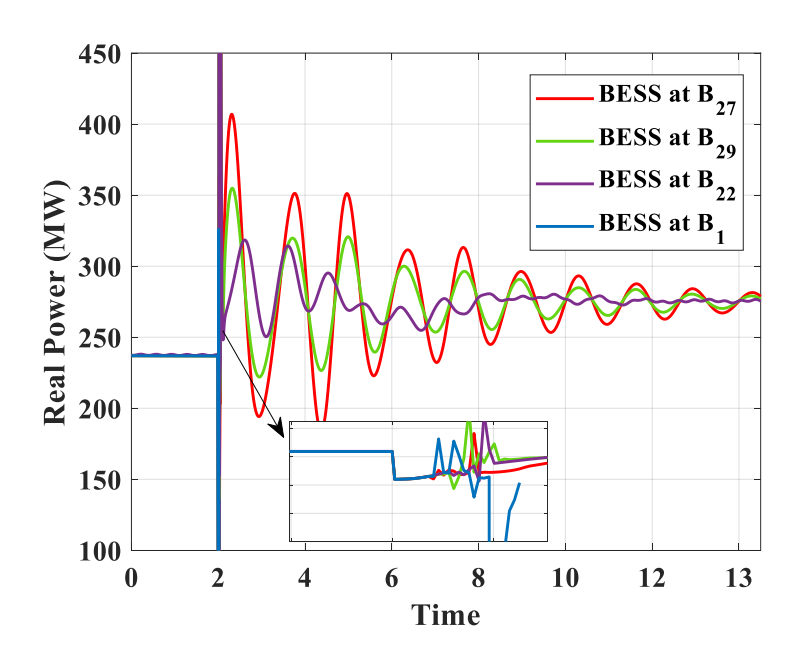


Figure 4.7 The real power flow of L_{4-14} due to BESS at different busses

VIC-based BESS placed on different buses. To validate the suitable location of BESS to be B_{22} as a result of section 1.4, the performance of BESS is decided to be tested by placing it at different busses such as B_1 , B_{22} , B_{27} , and B_{29} . Figure 4.7 shows that the installation of BESS other than B_{22} experiences sustained oscillations in the post-fault response of the real power flow in L_{4-14} . The post-fault response becomes unstable when the BESS is installed at B_1 which is very close to

the location of COI. However, the VIC-based BESS at B_{22} , the real power flow in L_{4-14} after clearing the fault, it experiences an acceptable phenomenon with quick damp out of oscillations.

4.7 Conclusion

The power system is undergoing swift incorporation of converter-based energy resources like SPV, wind energy systems, BESS, HVDC, etc., such that the transformation originates in rising uncertainties in power injection into the grid and reduced inertia. The growing uncertainties in renewable sources involve complexity in power systems and pose significant challenges in damping the fluctuations of system frequency and electromechanical oscillations. In this chapter, the intensity of the uncertainties is evaluated by different GSA methods. The GSA methods are employed to identify the most impactful parameters among extensive sets of uncertain inputs. The system uncertainties dealt with by various GSA methods are (a) generations from conventional sources, (b) variations in loads, and (c) power injection from SPVs. The severity of the uncertainties is evaluated to rank all the generator buses except the slack generator (G2) and G1, which represents the aggregation of a large New York Power System (NYPS) by replacing one of the SGs with a similarly rated SPV once at a time. Various GSA techniques like Sobol sensitivity, RBD FAST, Delta moment indices, and PAWN were employed to assess the ranking of generators, and a high degree of consensus was achieved among all the GSA techniques used. Then, the generators G3, G6, G7, and G9, as identified in Table 4.3 under the severe category, are replaced by similarly rated SPVs to identify the most influential parameter. The identified most influential parameters from Table 4.5 are validated against D_{index} of buses presented in Figure 4.4. It is concluded from Table 4.5 and Figure 4.4 that the power injection from PV_2 (or B_{22}) is found to be the most influential and the farthest bus from the location of COI. Hence, a VIC-based BESS is placed on B_{22} , expected to have a better damping phenomenon. The PSSs are assigned to the SGs G4 and G5 based on the theory of SPE. A PSO algorithm is used to tune the parameters of VIC and PSS optimally. The time domain plots of real power flow thorough L_{17-18} in Figure 4.6 and Figure 4.7 evidence that the most influential uncertain parameter may have a high Dindex value, which is expected to have a better damping phenomenon, and the control parameters of VIC and PSS tuned by PSO have the optimal coordination to achieve better damping of power oscillations.

In essence, the research highlighted the critical role of system uncertainties in influencing the dynamic performance of the IEEE 39 bus test system. Through comprehensive modal sensitivity analysis using various GSA methods, the study identified 25 uncertainties, including variations in generator output, load, and solar photovoltaic (SPV) output. By ranking the severity of these uncertainties, the analysis facilitated a clearer understanding of their impact on system stability. This ranking was instrumental in determining the optimal placement for a Battery Energy Storage System (BESS) equipped with a Virtual Inertia Controller (VIC). The practical findings of the study suggest

- (i) Accurately identifying and ranking the system uncertainties can significantly enhance the strategic placement of stabilizing mechanisms, thereby improving overall grid stability.
- (ii) Uncertainties associated with PV systems are the most critical and require proper attention.
- (iii) Proper coordination in tuning the control parameters of the Virtual Inertia Controller (VIC) and Power System Stabilizer (PSS) can achieve better damping of power system oscillations.

The research work in this chapter may help identify the most critical uncertain parameters that influence system performance. Further, the research in this chapter effectively contains the system uncertainties in designing a control system to achieve better-damping power system oscillations.

Chapter 5

Evaluation of Power System Oscillatory Modes Under the Influence of PV-BESS Dynamics

The increase of power electronically interfaced Photo-Voltaic (PV) power plants into power systems causes severe stability problems due to lack of inertia and damping effect. The Battery Energy Storage Systems (BESS) at PV stations can be controlled by a Virtual Inertia Controller (VIC) to provide virtual inertia and damping support while smoothing the power fluctuations of the PV power plant. The research of this chapter investigates the probabilistic distribution of power systems' Low-frequency Electromechanical Oscillations (LEOs) for various controller gains of VIC and stochastic variation of solar irradiance under the influence of Phase-Locked Loop (PLL) dynamics. The modal interaction of PLL and virtual inertia controller with power system oscillatory modes are investigated by stochastic eigenvalue analysis using the Monte Carlo simulation approach.

5.1 Introduction

As the modern power system is transforming towards more sustainability, Solar Photo-Voltaic (SPV) is the most adaptable alternative. However, the uncertainty and variability in power harnessing from SPV introduces serious concerns about instability. In this scenario, PV-BESS has become a promising solution for addressing this challenge. PV generates power during the day, while BESS stores electricity for later use. As PV-BESS has zero inertia, it cannot maintain frequency stability in case of sudden changes in load or generation. Hence, a Virtual Inertia Controller (VIC) with PV-BESS imitates a traditional synchronous generator by providing an inherent inertia mechanism. Therefore, a VIC-based PV-BESS can prevent frequency fluctuation and smooth out power fluctuations. However, VIC's parameter setting becomes challenging while power generation uncertainties from the PV-BESS system are considered. As concluded in the previous chapter, the VIC-enabled BESS could enhance the damping phenomenon of the low inertia-based power system. It is necessary to further analyze the stochastic shift of concerned eigenmodes to incorporate a better damping phenomenon from a VIC-based PV-BESS system. Based on the literature survey, it is observed that limited research papers, like [71] and [44], have analyzed stochastic eigenvalue studies to investigate the shifting of eigenvalue resulting from

various operating points due to the increasing penetration of renewable sources. This implies that the stochastic analysis of modal shifting of PV-integrated power systems has an adequate scope of research.

This work investigates the stochastic behavior of power systems' small signal stability under the joint dynamic impact of a VIC-based PV-BESS system. Most of the research contributions presented in this chapter include the following:

- (i) A probabilistic small signal model of a VIC-based PV-BESS system is developed with joint dynamics of PLL.
- (ii) A stochastic eigenvalue analysis is proposed based on the Montecarlo simulation approach.
- (iii) Finally, the proposed methodology is implemented on the IEEE 39 bus test system to propose a better design of VIC controller gain to enhance system stability.

5.2 Small Signal Modeling of PV-BESS-Based Power Systems

The power system in this research consists of Synchronous generators (SGs), a PV-BESS-based power plant, and loads. It is very important to establish the dynamic model of each power system component for modal analysis. Each of the SGs considered here is modeled with a 7th-order system consisting of IEEE Type 1 exciter, and none of the SGs are equipped with Power System Stabilizers (PSS). The electrical loads of the power system are modeled as a constant power load. The complete dynamics of Rest of the Power Systems (RPS) is described by a set of differential equations that represent the dynamics of SG and the algebraic equations that represent the stator and network equations [81], [79]. The grid-connected PV-BESS comprises a PV array, inverter, and associated controllers of PV and BESS, as shown in Figure 5.1. As the article focuses on how the power penetration from the PV-BESS combination affects the modal interaction through the converter controllers with the electromechanical oscillation of SGs of the power system, the solar farm with battery energy sources is considered a single generator [76]. The small signal model of all the associated controllers of PV-BESS is described in the next section.

5.2.1 Modeling of PV inverters

The modeling of the PV system in this study is carried out by controllers associated with the DC/AC inverter that converts the DC power output from the PV array to the AC power that is

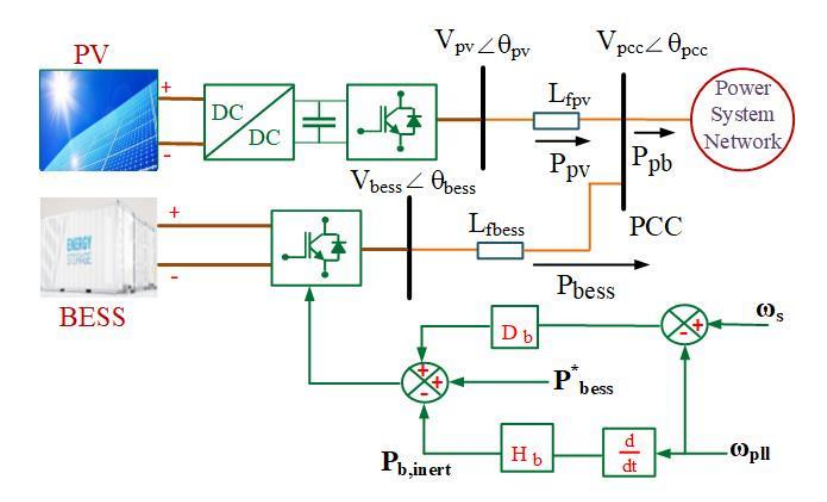


Figure 5.1 Schematic of grid-integrated PV-BESS system

interfaced with the rest of the power system by a coupling transformer. The control dynamics of the DC-DC converter used for drawing MPP power from the PV array and that of DC link capacitor control are assumed to be fast dynamics. Hence, the small signal modeling of the PV system is accomplished by involving the control dynamics of the active power controller, reactive power controller, PLL, and the dynamics involved with filter impedance.

i. Active/Reactive Power Controller

The active/reactive power control scheme of the PV system is modeled by a Proportional and Integral (PI) controller based on the outer loop and inner loop controllers. The outer loop power controller equations are given in (5.1) set the current references for the inner loop current controller, while the inner loop current controller, as given in (5.2), sets the voltage reference for PWM switching.

$$\begin{cases} I_{qpv}^* = \left(P_{pv}^* - P_{pv}\right) \left(K_{pp1} + \frac{K_{ip1}}{S}\right) \\ I_{dpv}^* = \left(Q_{pv}^* - Q_{pv}\right) \left(K_{pp3} + \frac{K_{ip3}}{S}\right) \end{cases}$$
(5.1)

$$\begin{cases} V_{qpv}^* = \left(I_{qpv}^* - I_{qpv} \right) \left(K_{pp2} + \frac{K_{ip2}}{S} \right) \\ V_{dpv}^* = \left(I_{dpv}^* - I_{dpv} \right) \left(K_{pp4} + \frac{K_{ip4}}{S} \right) \end{cases}$$
(5.2)

The $I_{qpv} - jI_{dpv}$ and $V_{qpv} - jV_{dpv}$ of (5.1) and (5.2) are the current and voltage in d - q axis, respectively. " * " in (5.1) and (5.2) denotes the reference value of the corresponding signals. P_{pv}

and Q_{pv} are active and reactive power generation from the solar PV system and are computed based on the following equations:

$$\begin{cases} P_{pv} = V_{pb}^{q} I_{qpv} + V_{pb}^{d} I_{dpv} \\ Q_{pv} = V_{pb}^{q} I_{dpv} - V_{pb}^{d} I_{qpv} \end{cases}$$
 (5.3)

ii. PLL

The whole PV-BESS system is frequency synchronized by PLL. The PLL traces the phase as the output of the phasor quantity at its input [96]. The working principle of the PLL used in this article is based on the Synchronous Reference Frame-based PLL (SRF-PLL). The following equilibrium can describe the PLL operation:

$$V_{pb}^d = V_{pcc} (\theta_{pcc} - \theta_{pll}) = 0 (5.4)$$

where $V_{pcc} \angle \theta_{pcc}$ is the input phasor to PLL at the terminal of PV-BESS, θ_{pll} refers to the measured output of PLL and V_{pb}^d is the d-axis voltage at the Point of Common Coupling (PCC). The dynamic characteristic of PLL can be explained by:

$$\begin{cases} x_{pll} = K_i^{pll} V_{pcc} (\theta_{pcc} - \theta_{pll}) \\ \theta_{pll} = K_p^{pll} V_{pcc} (\theta_{pcc} - \theta_{pll}) + x_{pll} \end{cases}$$
(5.5)

iii. Filter

The dynamics related to line voltage across the filter impedance (i.e., $\omega_{pll}L_{fpv}$) can be defined as follows:

$$\begin{cases}
L_{fpv} \frac{dI_q}{dt} = -\omega_{pll} I_{dpv} + V_{qpv} - V_{pb}^q \\
L_{fpv} \frac{dI_d}{dt} = -\omega_{pll} I_{qpv} + V_{dpv} - V_{pb}^d
\end{cases}$$
(5.6)

5.2.2 Model BESS Controllers

PV systems without BESS contribute almost zero inertia to the rest of the power system. In this literature, installing BESS with a PV system for smooth and constant power generation can introduce a certain level of inertia to enhance the overall stability of the power system. Introducing the swing equation of synchronous generator (SG) to the converter controller can emulate SG and provide virtual inertia to improve power system stability.

i. Inertia Controller

The virtual inertia control mechanism of the converter can be emulated by the following equation.

$$P_{bess} = P_{bess}^* + D_b (\omega_s - \omega_{pll}) - H_b \frac{d\omega_{pll}}{dt}$$
 (5.7)

where H_b imitates the inertia constant of SG and D_b as damping constant., ω_s is the synchronous frequency and ω_{pll} is the frequency measured at the terminal of BESS by PLL. The first part of (5.7) (i.e., P_{bess}^*) is the reference input to the active power controller of BESS's converter, corresponding to the smoothing effect due to intermittent power output from the solar PV system. However, the second part of the equation is the additional input to the active power controller due to a change in frequency at the BESS terminal.

ii. Active/Reactive Power Controller of BESS

As in the case of active/reactive power controllers of PV, BESS also comprises PI-based outer and inner loop controllers, as given in (5.1) and (5.2), respectively.

$$\begin{cases} I_{qbess}^* = (P_{bess}^{**} - P_{bess}) \left(K_{pb1} + \frac{K_{ib1}}{s} \right) \\ I_{dbess}^* = (Q_{bess}^* - Q_{bess}) \left(K_{pp3} + \frac{K_{ib3}}{s} \right) \end{cases}$$
(5.8)

$$\begin{cases} V_{qbess}^* = \left(I_{qbess}^* - I_{qpv}\right) \left(K_{pb2} + \frac{K_{ib2}}{s}\right) \\ V_{dbess}^* = \left(I_{dbess}^* - I_{dpv}\right) \left(K_{pb4} + \frac{K_{ib4}}{s}\right) \end{cases}$$

$$(5.9)$$

where $I_{qbess} - jI_{dbess}$ and $V_{qbess} - jV_{dbess}$ are the current and voltage in d-q axis of the BESS controller, respectively. " * " in (5.8) and (5.9) denotes the reference value of the corresponding signals. However, the " ** " relates to modified reference input to the active power controller due to the change in frequency response. P_{bess} and Q_{bess} are active and reactive power generation from the solar PV system and are computed based on the following equations:

$$\begin{cases} P_{bess} = V_{qbess}I_{qbess} + V_{dbess}I_{dbess} \\ Q_{bess} = V_{qbess}I_{dbess} - V_{dbess}I_{qbess} \end{cases} \tag{5.10}$$

iii. BESS Filter

The dynamics related to line voltage across the filter impedance (i.e., $\omega_{pll}L_{fbess}$) can be defined as follows:

$$\begin{cases} L_{fbess} \frac{dI_{qbess}}{dt} = -\omega_{pll}I_{dbess} + V_{qbess} - V_{pb}^{q} \\ L_{fbess} \frac{dI_{dbess}}{dt} = -\omega_{pll}I_{qbess} + V_{dbess} - V_{pb}^{d} \end{cases}$$

$$(5.11)$$

5.3 Stochastic Model Analysis of PV-BESS-Integrated Power System

In order to investigate the impact of PV-BESS on the Low-Frequency Electromechanical Oscillatory Modes (LEOs) of RPS, this work considers PV-BESS and the RPS as two open loop sub-systems inter-connected to form the closed loop where the PV-BESS is in the feedback path [93]. The set of non-linear differential and algebraic equations, the PV-BESS and RPS, are linearized around an equilibrium point to obtain the state-space model of each of the open loop sub-systems as given below:

$$\Delta \dot{x}_{rps} = A_{rps} \Delta x_{rps} + B_{rps} \Delta P_{pb}$$

$$\Delta V_{pb} = C_{rps} \Delta x_{rps} + D_{rps} \Delta P_{pb}$$
(5.12)

$$\Delta \dot{x_{rps}} = A_{rps} \Delta x_{rps} + B_{rps} \Delta P_{pb}$$

$$\Delta V_{pb} = C_{rps} \Delta x_{rps} + D_{rps} \Delta P_{pb}$$
(5.13)

where x_{rps} and x_{pb} are the vector of state variables of RPS and PV-BESS sub-systems, respectively. Then, the closed loop state equation can be established based on the following form:

$$[\dot{x_{cl}}] = [A_{cl}][x_{cl}] \tag{5.14}$$

where $[x_{cl}] = [x_{rps}, x_{pb}]^T$, $[A_{cl}] = \begin{bmatrix} A_{rr} & A_{rp} \\ A_{pr} & A_{pp} \end{bmatrix}$. The elements of A_{rp} and A_{pr} establish the relationship between the states of RPS and PV-BESS-based power plants. However, A_{rr} and A_{pp} are the decoupled matrix of RPS and PV-BESS, respectively. This chapter considers the stochastic variation of PV output power for small signal stability analysis of the closed-loop power system. The work uses the Monte Carlo simulation technique for stochastic modal analysis. The algorithm used in the Monte Carlo simulation is explained in Figure 5.2.

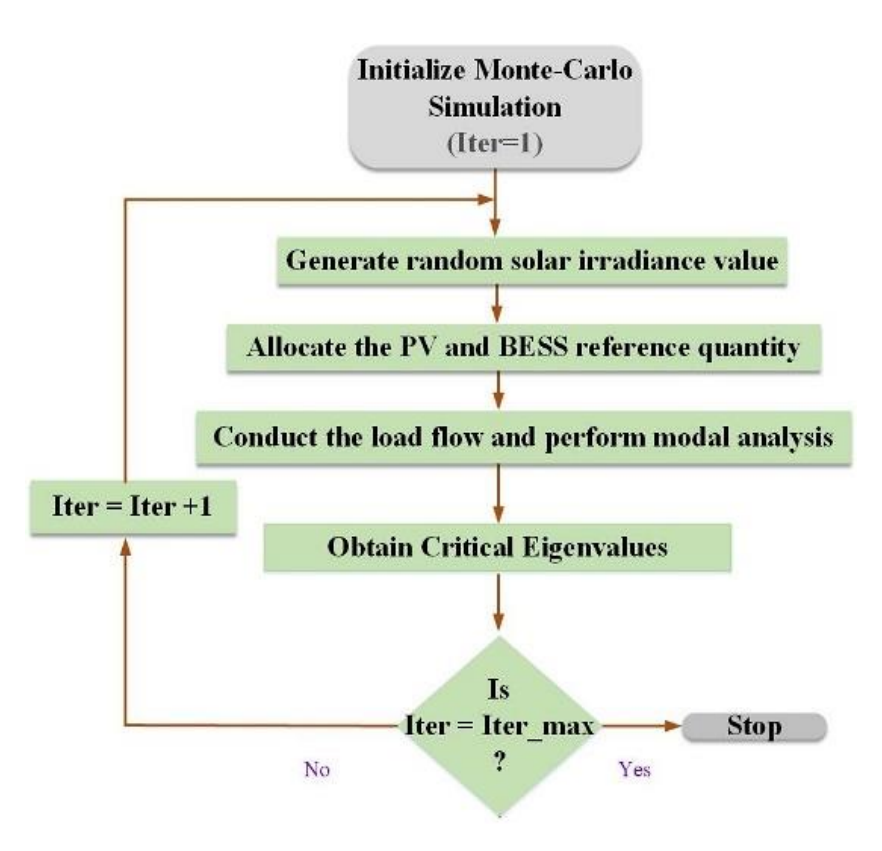


Figure 5.2 Proposed algorithm of Monte Carlo Simulation

5.4 Results and Discussions:

A small signal stability study has been conducted to observe the influence of PV-BESS on RPS. The analysis is evaluated on the IEEE 39 bus test system. As shown in Figure 5.3, generator G3 is assumed to be replaced by a PV-BESS system of equivalent rating. The PV-BESS system rating is 650 MW. In this work, the capacity of the BESS unit is assumed to be 0.35 times the rating of the PV system, i.e., 230 MW. Table 5.1 consists of all the parameters associated with the PV and BESS controllers in per-unit values on the base of the corresponding PV and BESS ratings, respectively. For all the case studies with PV-BESS, the PLL parameters are set to $K_P^{pll} = 1.5$ and $K_I^{pll} = 15$ and the filter inductance $L_{fbess} = L_{fpv} = 0.021$ p.u. The base of the whole power system is taken as 100 MVA. As mentioned in section 5.2, each of the SGs of RPS is modeled using the 7th-order system, which comprises an IEEE Type 1 exciter. None of the SGs are enabled with PSS. The parameters of the SGs of the IEEE 39 bus tests system can be obtained from Appendix A. 4. The whole PV-BESS-integrated power system has been developed in MATLAB 2019b. The test case is analyzed based on two scenarios:

i. Power system without PV-BESS

ii. Power System with PV-BESS

5.4.1 Power System without PV-BESS

In this section, the IEEE 39 bus test system without PV-BESS installed has undergone a small signal stability study to obtain information regarding the critical inter-area eigenmodes that the system contains. The modes listed in Table 5.2 are critical because the damping ratio is as low as < 10%, and the damping frequency lies < 1 Hz, indicating the inter-area modes. The generators that participate in the critical inter-area modes are also listed in Table 5.2. The next section describes how these modes are affected by the involvement of stochastic characteristics of PV-BESS-based power plants.

5.4.2 Power system with PV-BESS

In the last section, it is observed that the open loop RPS has two critical inter-area modes. The eigenvalues of the closed-loop PV-BESS are given in Table 5.3. The modal analysis results in Table 5.3 are obtained from the PV-BESS-integrated IEEE 39 bus test system, while PV and BESS

Component	Active Power Controller				Reactive Power Controller			
Component	K_{pp1}	K_{ip1}	K_{pp2}	K_{ip3}	K_{pp3}	K_{ip3}	K_{pp4}	K_{ip4}
PV	2	10	2	10	2	10	2	10
BESS	K_{pb1}	K_{ib1}	K_{pb2}	K_{ib2}	K_{pb3}	K_{ib3}	K_{pb4}	K_{ib4}
BESS	1	5	1	5	1	5	1	5

Table 5.1: Parameters of PV-BESS Controllers

Table 5.2: Inter-Area Modes of IEEE 39 Bus Test System Without PV-BESS

Sl.	Eigenvalues	Damping Ratio (%)	Participating Generators
1	$-0.2077 \pm j$ 6.184	3.356	G3, G4, G5, G6, G7, G8, G10
2	-0.2996 ± <i>j</i> 4.0614	7.36	G1, G2, G3, G4, G5, G6, G7, G8, G9, G10

 Table 5.3: Critical Eigenmodes of IEEE 39 Bus Test System With PV-BESS

Sl.	Eigenvalues	Damping Ratio (%)	Participating Generators
1	$-0.2096 \pm j \ 6.2269$	3.364	G5, G6, G7, G8, G10
2	$-0.3057 \pm j \ 4.3886$	6.956	G1, G5, G6, G7, G8, G10, PV- (Filter)
3	-0.3277± j 4.2119	7.76	G7, G8, G10, PV(Filter)
4	-0.0137± j 3.2538	0.42	G1, PLL

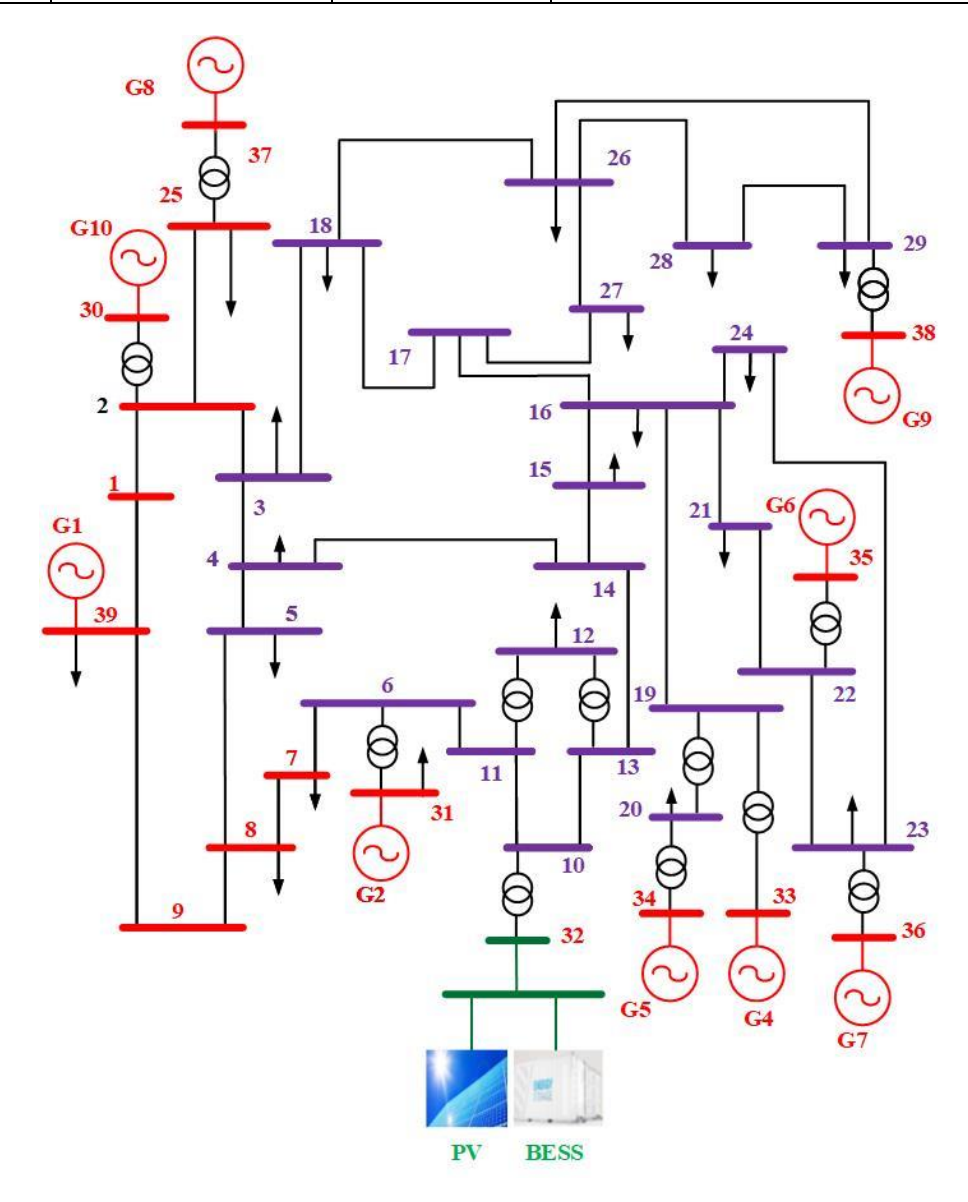


Figure 5.3 Modified IEEE 39 bus test system

operates at 550 MW and 100 MW, respectively. As shown in Table 5.3, modes 3 and 4 are newly added oscillatory modes, which are associated with the dynamics of the PLL and filter component of the PV-BESS system. Mode 4 of PV-BESS is found to be the most critical eigenvalue of the closed-loop systems. Further, mode 3 affects mode 2 by reducing the damping ratio from 7.36 to 6.956 because of modal resonance. As the influence of PV-BESS on modal interaction is inevitable, it is further necessary to examine the pattern of the probabilistic distribution of all the concerned eigenvalues under variation of PV-BESS output power. Regarding the PV output power distribution, the solar irradiance is assumed to be Gaussian. The Probability Density Function (PDF) of 5 years of solar irradiance data is displayed in Figure 5.4. The PDF of solar irradiance data is obtained based on the following equation:

$$\begin{cases}
f_d(l) = \frac{1}{\sigma_l \sqrt{2\pi}} e^{\frac{-(l-\mu_l)^2}{2\sigma_l^2}}
\end{cases}$$
(5.15)

where σ_l and μ_l are the standard deviation and mean of a set of random numbers l. The l is the set of Gaussian/Normal random numbers of solar irradiance. The stochastic eigenvalue evaluation is

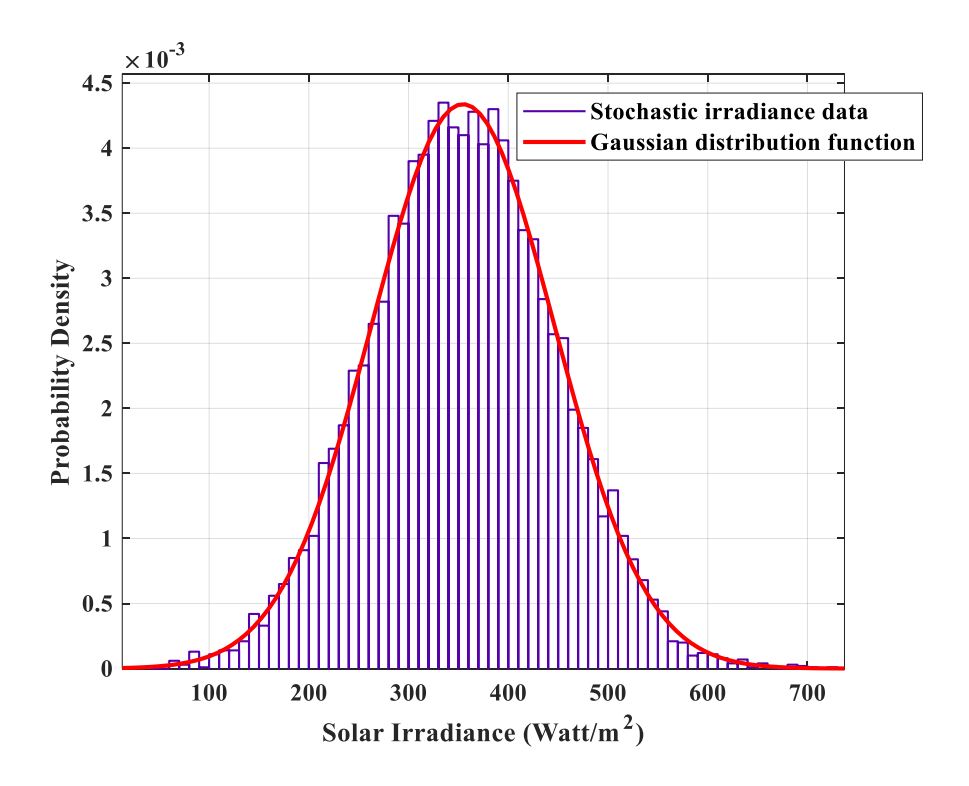


Figure 5.4 Stochastic Solar Irradiance data

conducted according to the steps of Monte Carlo simulation narrated in Figure 5.2 with 1000 iterations. The stochastic eigenvalue analysis is evaluated for different values of inertia controller gain, H_b , of the BESS. For each complete simulation, the H_b value is decided to increase from 2 to 12. The stochastic distribution of eigenvalues such as mode 1, mode 2, mode 3, and mode 4 are displayed in Figure 5.5 (a), (b), (c), and (d) respectively. The figures display only the variations of the real part of eigenmodes as the variations in the imaginary part are minimal and hence are ignored. Table 5.4 presents the mean and variance of critical modes for different values of H_b . Figure 5.5 (a) shows the shift of mode 1 in terms of probabilistic density due to stochastic variations in solar irradiance over a year for different values of H_b . From Figure 5.5 (a), it is observed that mode 1 is normally distributed in the range from -0.2098 to -0.2094 because of the normal distribution of solar irradiance. Moreover, from Table 5.4, the mean of the Gaussian distribution of mode-1 has a rightward shift due to the variation of H_b from 2 to 12. According to

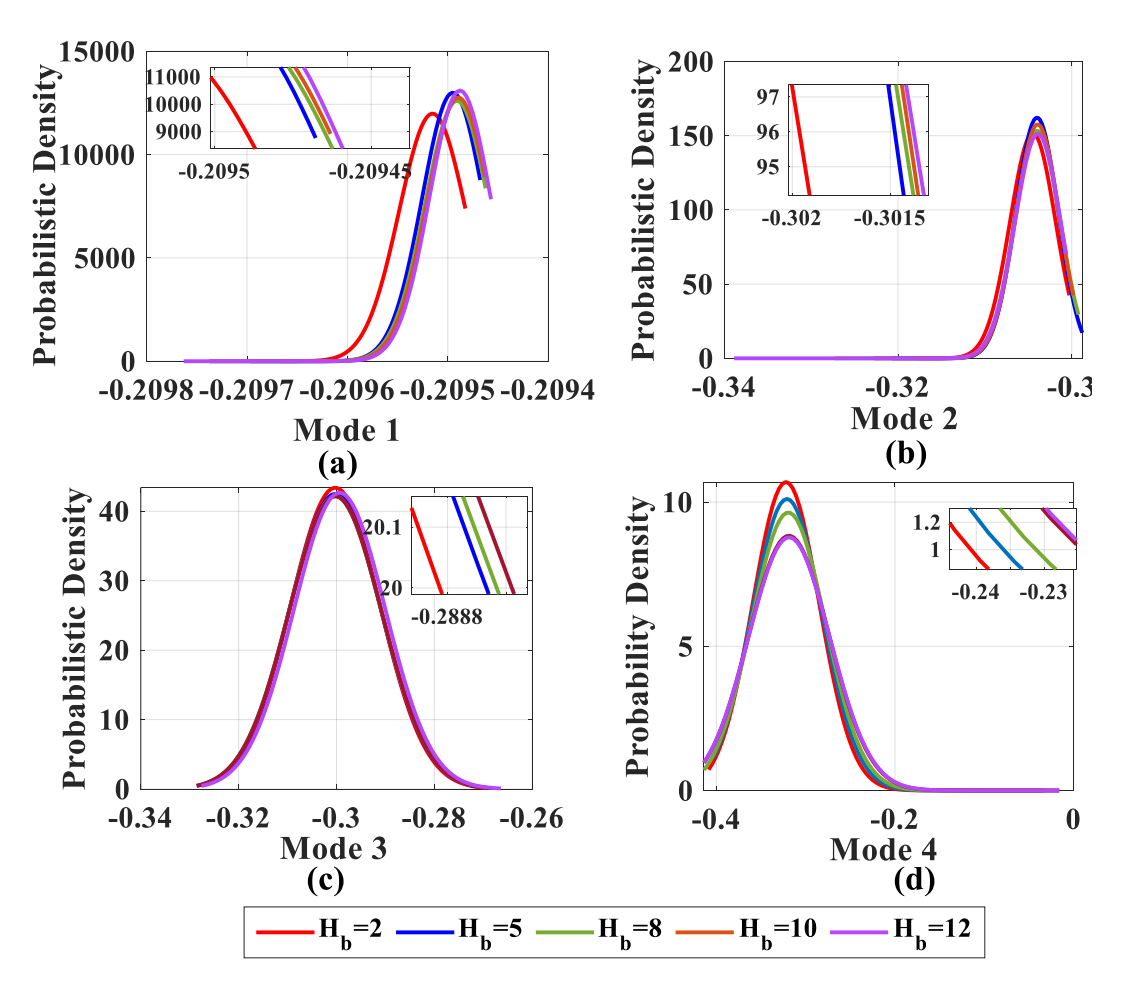


Figure 5.5 Probabilistic Distribution function of critical eigenvalues

Table 5.4: Mean And Variance of Critical Modes

Inertia	Mod	le 1	Mo	de 2	
controller gain	Mean	Var	Mean	Var	
2	-0.20951	1.1e-09	-0.30447	6.026e-06	
5	-0.20949	9.42e-10	-0.30399	6.905e-06	
10	-0.20948	9.77e-10	-0.30392	6.9408e-6	
12	-0.20943	1.076e-9	-0.30302	6.991e-06	
Inertia	Mod	le 3	Mode 4		
controller gain	Mean	Var	Mean	Var	
2	-0.30027	8.741e-05	-0.31937	0.0017	
5	-0.30025	8.811e-05	-0.3187	0.002	
10	-0.28936	8.915e-05	-0.3109	0.0026	
12	-0.2828	8.916e-05	-0.3092	0.0028	

the shift in the probabilistic distribution of mode 1, it can be said that the higher the H_b adversely affects mode 1 by moving the modal distribution toward the imaginary axis of the complex plane. However, the amount of shift is minimal compared to the shifts observed for modes 2, 3, and 4 because, according to Table 5.3, PV-BESS dynamics do not participate in mode 1. In Figure 5.5 (b), the consequence of increasing H_b on the probabilistic distribution of mode 2 due to the stochastic variation in solar irradiance has been exhibited. Further, as seen in Table 5.4, in this case, it is also observed that the increasing value of H_b adversely influence mode 2 by shifting the mean of its probabilistic distribution towards the imaginary axis. As per the result in Table 5.3, this mode participates in PV-BESS dynamics. Hence, this mode is more sensitive than mode 1 for solar intermittency and change in the value of H_b . A similar probabilistic distribution pattern of modes 3 and 4 has been observed from Figure 5.5 (c) and (d). A significant modal distribution is observed due to the stochastic variation in solar irradiance because these modes participate in PV-BESS dynamics. Moreover, the observed rightward shift of the mean of the modal distributions of modes 3 and 4 on the complex plane, as presented in Table 5.4, suggests that the increasing value of H_b can deteriorate the system's stability. As per the normal distribution of all the modes for every H_b it is clearly revealed that when H_b increases from 2 to 12, the mean of the Gaussian distribution of corresponding eigenmodes also shifts gradually towards the right half of the complex plane and eventually pushes the system towards instability. Consequently, it is implied that a lower H_b can cause the system to be more stable.

5.5 Conclusion

The solar PV system has great potential to meet the future energy demand as one of the renewable sources. As the PV provides almost zero inertia, the increasing penetration of the PV power plants into the grid causes serious concerns about system stability. The BESS controlled by VIC at PV stations not only smoothens the intermittent output power of PV but also can extend the support of virtual inertia by damping the LEOs of power systems. This chapter thoroughly discusses the dynamics of controllers associated with the PV-BESS system. The impact of VIC at PV-BESS station on LEOs of RPS is tested on the IEEE standardized 39 bus test system. It is witnessed from Table 5.2 and Table 5.3 that the PV-BESS with VIC contributes results in additional oscillatory modes and significantly deteriorates the small-signal stability due to closely resonated modes. A Monte Carlo simulation-based stochastic eigenvalue analysis is conducted to observe the impact pattern of the concerned eigenvalues due to the different values of inertia controller gain, H_b , with probabilistic variation in solar irradiance. As per the results shown in Figure 5.5, it is observed that the stochastic distributions of all the concerned eigenvalues of IEEE 39 bus test systems move rightward of the complex plane while H_b of BESS's VIC is increased from 2 to 12. Therefore, it can be concluded that higher VIC gain of PV-BESS may result in power system instability. Alternatively, the lesser value of H_b poses enhanced power system stability. Further, this research can be helpful for the design of VIC of BESS under the impact of stochastic variation in PV output.

Chapter 6

Conclusion and Future Scope

This chapter presents the key findings of the thesis research work. Additionally, the chapter encompasses the potential area of research for future aspects.

6.1 Recap of Main Contributions

In response to the post-Paris agreement, a significant transition has been observed in modern power systems driven by the rapid integration of renewable-based energy resources like solar or wind. The prime cause behind the unconventional shift in the energy sector is worldwide awareness regarding the importance of sustainable energy generation, technological advancement in power electronic-based converter stations, and effective policy implementation. As a result, the complexity of modern power systems increases with respect to the complex architecture of converter control and uncertainties in power injection due to renewable sources. Consequently, maintaining dynamic stability is a challenging task for the modern power system with such a large-scale integration of renewable sources. In this response, most of the research contribution in this thesis highlights the following points:

- i. Synchronizing/Damping Torque analysis: To ensure grid stability, a crucial aspect is understanding how renewable energy sources, through their control systems, can contribute to the electromechanical oscillation damping provided by synchronous generators. As a major contribution to the thesis, it introduces a DFIG-based wind-integrated power system to present a simplified mathematical formulation for analyzing system parameters' impact on damping inter-area oscillations.
- ii. Influence of VIC and PLL dynamics on small signal stability: To support the WES during frequency excursion events, the dynamics of the VIC and PLL control loop combined impact the electromechanical oscillation loop of the power system's synchronous generator. In dealing with the given issue, the thesis has proposed a mathematical formulation to analyze the influence of the control parameters of VIC and PLL on the synchronizing and damping torque coefficient of the WES-integrated Single Machine Infinite Bus (SMIB) system. Further, a new methodology has been proposed to

design a Power System Stabilizer (PSS), considering the combined impact of VIC and PLL dynamics.

- **Quantification of uncertainties associated with SPV:** The power system deals with various uncertainties related to (a) generations from conventional sources, (b) variations in loads, and (c) power injection from SPVs. In this scenario, the thesis also has introduced a probabilistic ranking methodology for all the generator buses to identify the most suitable bus that could be replaced with SPV by popular GSA tools like Sobol, RBD-FAST, DMIM, and PAWN. Additionally, the GSA tools recognize the most influential uncertain parameter.
- iv. Probabilistic eigenvalue analysis: The stochastic power injection from large-scale SPV impacts the power system by shifting the oscillatory modes of interest. Hence, this research also introduces probabilistic small signal stability of power systems with large-scale SPVs. This analysis has also considered stochastic PV generation with the joint dynamic impact of BESS, VIC, and PLL.

6.2 Summary of the Key Findings

A major part of the thesis focuses on analyzing the impact of various influential parameters of renewable-integrated power systems, including WES and SPV systems, on damping the electromechanical oscillations of synchronous generators. In this regard, the summary of the research findings of the thesis is provided chapter by chapter as below:

Chapter 1 lays the foundation of the research undertaken in this thesis. The chapter provides brief glimpses into climate change and its impacts on Earth, along with the steps carried out to combat the effect of climate change. It has explored the challenges in the transition of the modern power system in rapidly integrating various renewable sources such as wind or solar-based energy stations. A significant part of the chapter is dedicated to the literature review of recent technological developments, which forms the backbone of the research work presented in the thesis. Finally, the chapter outlines the objectives and key contributions of the research, followed by a thesis outline.

Chapter 2 investigates various system parameters' impact on the EOL of SGs. For the given investigation, the chapter considers a DFIG-based WES-integrated power system, and to

account for system parameters, it considers line reactance, bus voltage, and machine inertia. The objective of the mentioned investigation is accomplished by developing a set of equations described as synchronizing and damping torques provided by DFIG-based WES to EOL of SGs as a function of the defined system parameters for a 3-bus system consisting of two synchronous machines and a DFIG-based WES. Further, the chapter also examines the locational parameter that defines the location of DFIG with respect to the COI for any possible impact on the damping of electromechanical oscillations of synchronous machines. After validation of the obtained results obtained for both the three-bus system and the IEEE standardized 39-bus test system, the research has proposed the following novel findings:

- a) The damping torque produced by DFIG to the EOL of RPS is greatly influenced by transmission line reactance.
- b) The parameters like bus voltage and synchronous machine inertia have a negligible impact on the damping torque contributed by DFIG.
- c) The positive or negative characteristic of damping torque mainly happens due to the load angle difference between synchronous machines.
- d) A better damping phenomenon is observed in the low-frequency oscillatory mode of the system, while the DFIG-based WES is chosen to be located far from COI.

Chapter 3 emphasizes the investigation of VIC and PLL dynamics on change in synchronizing/damping torque coefficients caused by the involvement of DFIG-based WES. A modified SMIB system consisting of an SG and DFIG-based WES is considered for the small-signal analysis of the system influenced by VIC and PLL dynamics. The significance of the involvement of VIC and PLL dynamics is achieved by deriving mathematical equations for the change in synchronizing/damping torque coefficients as a function of line reactance, K_{inert}, and PLL parameters. From the analysis of the result verifications obtained from both the modified SMIB and the IEEE 9 bus system, most of the findings are as listed below:

a) The increase in value of virtual inertial gains K_{inert} reduces synchronizing torque but increases the damping torque of the system. Therefore, a system with high K_{inert} may lose synchronism.

b) To improve the stability performance of a power system, the joint effects of the PLL and inertial controller of the DFIG must be considered in the design process of the PSS for the SG.

The research in Chapter 4 addresses the uncertainties of power injection from growing SPVs in the modern power system. Additionally, the research of the chapter also considers the uncertainties associated with load variation and generations from SG. The uncertainties in this chapter are dealt with by various GSATs, such as Sobol sensitivity, RBD-FAST, Delta moment indices, and PAWN, to identify the most impactful parameters among extensive sets of uncertain inputs. The GSATs employed here are utilized to assess the severity of uncertainties based on which the ranking of IEEE 39 bus NETS generators is evaluated by replacing one of the SGs with an equal-rated SPV once at a time and further, have revealed a high degree of consensus among all the GSA techniques used. As presented in Chapter 4, the generators classified under the most severe category, such as G3, G6, G7, and G9, are replaced by similarly rated SPVs and have undergone the GSA to determine the most influential uncertain parameters. Further, from the distance indexing D_{index} , of all the busses, is evidenced by the fact that the most influential bus, B_{22} , lies at the farthest location from the COI. As is seen from Chapter 3, the farthest bus from COI has a better damping phenomenon. This characteristic is well observed when a time domain plot of real power flow of line, L_{17-18} , for a three-phase fault is taken for a VIC-based BESS when placed at B_{22} and optimized with PSSs for SGs G4 and G5. From the response of real power flow, it is observed that the highest distanced bus from COI, where VIC-based BESS is placed, provides better power oscillation damping of power oscillation. Hence, the main finding of this chapter is that:

- a) The uncertainties associated with modern power systems can be easily analyzed by GSATs.
- b) The bus linked with the most influential uncertain parameter may exert a better damping contribution to the most critical oscillatory modes.
- c) Coordinated PSO optimization for parameter tuning of VIC-based BESS and PSSs provides a better damping phenomenon than individual BESS or PSS controller tuning.

Finally, in Chapter 5, probabilistic small signal stability analysis is introduced to study the stochastic behavior of the EmOM of interest. In this context, the chapter thoroughly discusses the detailed dynamics of controllers associated with the PV-BESS system and VIC dynamics. The

probabilistic eigen-analysis is employed in the IEEE 39 bus test system to demonstrate the impact of uncertainties associated with PV-BESS on shifting the EmOM of the rest of the power system. It is revealed in the chapter that the inclusion of the PV-BESS with VIC contributes additional oscillatory modes and significantly deteriorates the closely resonated modes. A Monte Carlo simulation is conducted to perform a stochastic eigenvalue analysis. This analysis aims to observe the impact pattern of the system's eigenvalues due to combined variations in stochastic solar irradiance and the inertia controller gain, H_b . As per the results presented in this chapter, it is observed that the stochastic distributions of all the concerned eigenvalues of IEEE 39 bus test systems move rightward of the complex plane while H_b of BESS's VIC is increased from 2 to 12. Therefore, it can be ensured that a higher VIC gain of PV-BESS may risk power system instability. On the other hand, the lesser value of H_b poses enhanced power system stability.

6.3 Future Research Scope

The research findings of the thesis reveal the crucial involvement of various system parameters and control loops of the DFIG-based WES and SPV of modern power systems in the damping of electromechanical oscillations. Further research could focus on the following key aspects in future investigations:

- Modern power systems will be transformed in the future with the complete shift to renewable-based energy resources. In that scenario, the present research of the thesis can be extended to investigate the implication of system parameters like line reactance, bus voltage, and control parameters of various control loops of converters associated with renewable sources or HVDC links for virtual inertia estimation.
- Investigation of power system oscillation damping for a power system composed of entirely renewable sources utilizing multi-terminal HVDC links where controllers operate in grid forming mode could be a crucial area of research in future research aspects.
- As VIC will play a crucial role in the grid-forming mode of operations in converterinterfaced power systems, future research could focus on the advanced design of VIC in coordination with damping controller design under the influence of various system uncertainties, including intermittent power injection and load variations.

Appendix A

A. 1 State space derivation DFIG-based WES

Derivation of state space model representation of DFIG-based WES is very important for a thorough understanding of Chapter 2 and Chapter 3. However, this section is directly related to Chapter 2. As mentioned in Chapter 2, the stator and rotor flux linkage of DFIG is considered to have fast dynamics and hence is dropped to consider their dynamics for the modeling of DFIG. Therefore, the major components considered for modeling DFIG-based WES here are the turbine and gearbox, the Rotor Side Converter (RSC), and the Grid Side Converter (GSC). The detailed dynamics associated with these components are presented in (2.14) - (2.19) of Chapter 2. Now the linearization of (2.14) - (2.19) can be represented in the following form:

$$\begin{bmatrix} \Delta I_{qrD} \\ \Delta I_{drD} \end{bmatrix} = \frac{1}{X_{mD}} \begin{bmatrix} X_{sD} & -R_{sD} \\ R_{sD} & X_{sD} \end{bmatrix} \begin{bmatrix} I_{qsD} \\ I_{dsD} \end{bmatrix} + \begin{bmatrix} 0 \\ \frac{1}{X_{mD}} \end{bmatrix} [\Delta V_D]$$
 (A. 2)

$$\begin{bmatrix} \Delta I_{qsD} \\ \Delta I_{dsD} \end{bmatrix} =$$

$$\begin{bmatrix} \left\{ -\frac{sX_{rD}I_{qrDo}\omega_{s}}{X_{mD}} - \omega_{s} \left(R_{rD}I_{drDo} - V_{drD} - sX_{rD}I_{qrDo} \right) \right\} \frac{X_{mD}}{(\omega_{rDo} - \omega_{s})^{2}} & 0 & 0 & 0 & 0 \\ \left\{ -\frac{sX_{rD}I_{drDo}\omega_{s}}{X_{mD}} - \omega_{s} \left(V_{qrD} - R_{rD}I_{qrDo} - sX_{rD}I_{drDo} \right) \right\} \frac{X_{mD}}{(\omega_{rDo} - \omega_{s})^{2}} & 0 & 0 & 0 & 0 \end{bmatrix} \begin{bmatrix} \Delta\omega_{rD} \\ \Delta x_{1} \\ \Delta x_{2} \\ \Delta x_{3} \\ \Delta x_{A} \end{bmatrix} +$$

$$\begin{bmatrix} \frac{X_{rD}}{X_{mD}} & -\frac{R_{rD}}{sX_{mD}} \\ \frac{R_{rD}}{sX_{mD}} & \frac{X_{rD}}{X_{mD}} \end{bmatrix} \begin{bmatrix} \Delta I_{qrD} \\ \Delta I_{drD} \end{bmatrix} + \begin{bmatrix} 0 & \frac{X_{mD}}{s} \\ -\frac{X_{mD}}{s} & 0 \end{bmatrix} \begin{bmatrix} \Delta V_{qrD} \\ \Delta V_{drD} \end{bmatrix}$$

(A. 3)

$$\begin{bmatrix} \Delta \omega_{rD} \\ \Delta x_1 \\ \Delta x_2 \\ \Delta x_3 \\ \Delta x_1 \end{bmatrix} + \begin{bmatrix} \frac{K_{P1}K_{P2}V_{qSDo}}{K_{P1}K_{P2}I_{qrDo} - 1} & \frac{K_{P1}K_{P2}K_{P3}K_{P4}I_{drDo}V_{qSDo}}{K_{P1}K_{P2}I_{qrDo} - 1} \\ 0 & -K_{P3}K_{P4}V_{qSDo} \end{bmatrix} \begin{bmatrix} \Delta I_{qSD} \\ \Delta I_{drD} \end{bmatrix} +$$

$$\begin{bmatrix} -\frac{K_{P2}(K_{P1}V_{qrDo}-)}{K_{P1}K_{P2}I_{qrDo}-1} & \frac{K_{P1}K_{P2}(K_{P4}I_{drDo}-V_{drDo})}{K_{P1}K_{P2}I_{qrDo}-1} \\ 0 & -K_{P4} \end{bmatrix} \begin{bmatrix} \Delta I_{qrD} \\ \Delta I_{drD} \end{bmatrix} + \begin{bmatrix} \frac{K_{P1}K_{P2}(I_{qsDo}+K_{P3}K_{P4}I_{drDo}I_{dsDo})}{K_{P1}K_{P2}I_{qrDo}-1} \\ -I_{dsDo}K_{P3}K_{P4} \end{bmatrix} [\Delta V_{D}]$$
(A. 4)

$$\begin{bmatrix}
\Delta P_g \\
\Delta Q_g
\end{bmatrix} = \begin{bmatrix}
-V_{qrDo} & -V_{qrDo} \\
0 & 0
\end{bmatrix} \begin{bmatrix}
\Delta I_{qrD} \\
\Delta I_{drD}
\end{bmatrix} + \begin{bmatrix}
V_{qsDo} & 0 \\
0 & V_{qsDo}
\end{bmatrix} \begin{bmatrix}
\Delta I_{qsD} \\
\Delta I_{dsD}
\end{bmatrix} + \begin{bmatrix}
-I_{qrDo} & -I_{drDo} \\
0 & 0
\end{bmatrix} \begin{bmatrix}
\Delta V_{qrD} \\
\Delta V_{drD}
\end{bmatrix} + \begin{bmatrix}
I_{qsDo} \\
I_{qsDo}
\end{bmatrix} [\Delta V_D]$$
(A. 5)

The above equation can be symbolically represented as:

$$[\Delta \dot{x_D}] = A_{D1}[\Delta x_D] + B_{D1} \begin{bmatrix} \Delta I_{qSD} \\ \Delta I_{dSD} \end{bmatrix} + B_{D2} \begin{bmatrix} \Delta I_{qrD} \\ \Delta I_{drD} \end{bmatrix} + B_{D3} \begin{bmatrix} \Delta V_{qrD} \\ \Delta V_{drD} \end{bmatrix} + B_{D4}[\Delta V_D]$$
 (A. 6)

$$\begin{bmatrix} \Delta I_{qrD} \\ \Delta I_{drD} \end{bmatrix} = D_{D1} \begin{bmatrix} \Delta I_{qsD} \\ \Delta I_{dsD} \end{bmatrix} + D_{D2} [\Delta V_D] \tag{A. 7}$$

$$\begin{bmatrix} \Delta V_{qrD} \\ \Delta V_{drD} \end{bmatrix} = C_{D1} [\Delta x_D] + D_{D3} \begin{bmatrix} \Delta I_{qrD} \\ \Delta I_{drD} \end{bmatrix} + D_{D4} \begin{bmatrix} \Delta I_{qsD} \\ \Delta I_{dsD} \end{bmatrix} + D_{D5} [\Delta V_D]$$
 (A. 8)

$$\begin{bmatrix} \Delta I_{qsD} \\ \Delta I_{dsD} \end{bmatrix} = C_{D2} [\Delta x_D] + D_{D6} \begin{bmatrix} \Delta I_{qrD} \\ \Delta I_{drD} \end{bmatrix} + D_{D7} \begin{bmatrix} \Delta V_{qrD} \\ \Delta V_{drD} \end{bmatrix}$$
(A. 9)

$$\begin{bmatrix} \Delta P_g \\ \Delta Q_g \end{bmatrix} = D_{D8} \begin{bmatrix} \Delta I_{qrD} \\ \Delta I_{drD} \end{bmatrix} + D_{D9} \begin{bmatrix} \Delta I_{qsD} \\ \Delta I_{dsD} \end{bmatrix} + D_{D10} \begin{bmatrix} \Delta V_{qrD} \\ \Delta V_{drD} \end{bmatrix} + D_{D11} [\Delta V_D]$$
 (A. 10)

From (A. 6) to (A. 10) the state equation of the DFIG-based WES can then be composed to

$$[\Delta \dot{x_D}] = A_D [\Delta x_D] + B_D [\Delta V_D]$$

$$\begin{bmatrix} \Delta P_g \\ \Delta Q_g \end{bmatrix} = C_D [\Delta x_D] + D_D [\Delta V_D]$$
(A. 11)

where

$$A_{D} = A_{D1} + B_{D3} * C_{D1} + F * E * (C_{D2} + D_{D7} * C_{D1})$$

$$B_{D} = F * E * G + K$$

$$C_{D} = H * E(C_{D2} + D_{D7} * C_{D1}) + D_{D10} * C_{D1}$$

$$D_{D} = H * E * G + J$$

The matrices E, F, G, H, J, K are further defined by:

$$E = (I - (D_{D6} + D_{D7} * D_{D3}) * D_{D1} - D_{D7} * D_{D4})^{-1}$$

$$F = B_{D1} + B_{D3} * D_{D4} + (B_{D3} * D_{D3} + B_{D2}) * D_{D1}$$

$$G = (D_{D6} + D_{D7} * D_{D3}) * D_{D2} + D_{D7} * D_{D5}$$

$$H = D_{D8} * D_{D1} + D_{D9} + D_{D10} * (D_{D4} + D_{D3} * D_{D1})$$

$$J = D_{D8} * D_{D2} + D_{D10} * (D_{D3} * D_{D2} + D_{D5}) + D_{D11}$$

$$K = (B_{D3} * D_{D3} + B_{D2}) * D_{D2} + B_{D3} * D_{D5} + B_{D4}$$

The matrix 'I' in E is an identity matrix of order 2

A. 2 Derivations to Support Section 3.2 of Chapter 3

This section assists in deriving ΔK_1 to ΔK_6 discussed in Section 3.2. From power balance equations (3.18) and (3.23), the following can be derived:

$$\begin{cases} \Delta \theta_p = T_1 \Delta \delta + T_2 \Delta E_q' \\ \Delta V_p = T_3 \Delta E_q' + T_4 \Delta \delta \end{cases}$$
 (A. 12)

$$\begin{cases} T_{1} = \frac{V_{po}V_{no}\cos\theta_{po}/X_{L2}}{V_{Po}M_{en}/(X_{L2}X_{1}) + s^{2}K_{in}F_{pll}/(2\pi)} \\ T_{2} = \frac{P_{go}/E'_{qo}}{V_{Po}M_{en}/(X_{L2}X_{1}) + s^{2}K_{in}F_{pll}/(2\pi)} \\ T_{3} = \frac{V_{po}X_{L2}\cos(\delta_{o} - \theta_{po})}{M_{en}} \\ T_{4} = -\frac{P_{go}X_{1}X_{L2}}{M_{en}} \end{cases}$$
(A. 13)

Using (A. 12) into (3.18), ΔP_g can be derived to the following form:

$$\Delta P_q = G_1(s)\Delta\delta + G_2(s)\Delta E_q' \tag{A. 14}$$

Further applying (A.12) to the linearization of \dot{E}'_q of synchronous generator mentioned in (3.14), the following can be derived:

$$\Delta \dot{E}'_{q} = -\frac{1}{T'_{do}G_{3}(s)} \dot{\Delta E'_{q}} - \frac{G_{4}(s)}{T'_{do}} \Delta \delta + \frac{\Delta E_{fd}}{T'_{do}}$$
(A. 15)

Using (3.23), ΔV_t can be derived to:

$$\Delta V_t = G_5(s)\Delta \delta + G_6(s)\Delta E_q' \tag{A. 16}$$

Now $G_1(s)$ to $G_6(s)$ derived in, (A. 14) to (A.16), can be separated as per the format expressed in (3.26) to derive ΔK_1 to ΔK_6 of (3.25).

A. 3 Data of parameters of DFIG-based WES

Table A. 1: Parameter of Generator, AVR, and Transformer

	Generator					VR	Transformer
H x_d x'_d x_q T'_{do}						T_a	x_T
6.4 0.8958 0.1198 0.8645 6					400	0.02	0.0625

Table A. 2: Parameters of a DFIG in a Wind Farm

MVA Rating	H_D (sec.)	R_{sD} (p.u)	X_{SD} (p.u)	R_{rD} (p.u)	X_{rD} (p.u)
3.6	5.23	0.007	3.37	0.005	3.47

A. 4 Parameter Data of IEEE 39 bus New England Test System

Table A. 3: Dynamic data of generators of IEEE 39 bus system

Generator	Н	R_a	X'_d	X_q'	X_d	X_q	T'_{do}	T'_{qo}	X_l
G1	500	0	0.006	0.008	0.02	0.019	7.0	0.7	0.003
G2	30.3	0	0.0697	0.170	0.295	0.282	6.56	1.5	0.035
G3	35.8	0	0.0531	0.0876	0.2495	0.237	5.7	1.5	0.0304
G4	28.6	0	0.0436	0.166	0.262	0.258	5.69	1.5	0.0295
G5	26	0	0.132	0.166	0.67	0.62	5.4	0.44	0.054
G6	34.8	0	0.05	0.0814	0.254	0.241	7.3	0.4	0.0224
G7	26.4	0	0.049	0.186	0.295	0.292	5.66	1.5	0.0322
G8	24.3	0	0.057	0.0911	0.290	0.280	6.7	0.41	0.028
G9	34.5	0	0.057	0.0587	0.2106	0.205	4.79	1.96	0.0298
G10	42	0	0.031	0.008	0.1	0.069	10.2	0.00	0.0125

Table A. 4: Generator Exciter Data

Generator	K_A	T_A	K_E	T_E	K_F	T_F
G1	40	0.02	1	1.4	0	0.03
G2	6.2	0.05	0.63	0.41	0	0.06
G3	5.0	0.06	-0.02	0.5	0	0.08
G4	5.0	0.06	-0.05	0.5	0	0.08

G5	40.0	0.02	-0.04	0.785	0	0.03
G6	5.0	0.02	1	0.471	0	0.08
G7	40.0	0.02	1	0.73	0	0.03
G8	5.0	0.02	-0.05	0.528	0	0.09
G9	40.0	0.02	1	1.4	0	0.03
G10	5.0	0.06	-0.05	0.25	0	0.4

Table A. 5: Line Data

From Bus	To Bus	R	X	В
1	2	0.0035	0.0411	0.6987
1	39	0.0010	0.0250	0.7500
2	3	0.0013	0.0151	0.2572
2	25	0.0070	0.0086	0.1460
3	4	0.0013	0.0213	0.2214
3	18	0.0011	0.0133	0.2138
4	5	0.0008	0.0128	0.1342
4	14	0.0008	0.0129	0.1382
5	6	0.0002	0.0026	0.0434
5	8	0.0008	0.0112	0.1476
6	7	0.0006	0.0092	0.1130
6	11	0.0007	0.0082	0.1389
7	8	0.0004	0.0046	0.0780
8	9	0.0023	0.0363	0.3804
9	39	0.0010	0.0250	1.2000
10	11	0.0004	0.0043	0.0729
10	13	0.0004	0.0043	0.0729
13	14	0.0009	0.0101	0.1723
14	15	0.0018	0.0217	0.3660
15	16	0.0009	0.0094	0.1710
16	17	0.0007	0.0089	0.1342

16	19	0.0016	0.0195	0.3040
16	21	0.0008	0.0135	0.2548
16	24	0.0003	0.0059	0.0680
17	18	0.0007	0.0082	0.1319
17	27	0.0013	0.0173	0.3216
21	22	0.0008	0.0140	0.2565
22	23	0.0006	0.0096	0.1846
23	24	0.0022	0.0350	0.3610
25	26	0.0032	0.0323	0.5130
26	27	0.0014	0.0147	0.2396
26	28	0.0043	0.0474	0.7802
26	29	0.0057	0.0625	1.0290
28	29	0.0014	0.0151	0.2490
12	11	0.0016	0.0435	0.0000
12	13	0.0016	0.0435	0.0000
6	31	0.0000	0.0250	0.0000
10	32	0.0000	0.0200	0.0000
19	33	0.0007	0.0142	0.0000
20	34	0.0009	0.0180	0.0000
22	35	0.0000	0.0143	0.0000
23	36	0.0005	0.0272	0.0000
25	37	0.0006	0.0232	0.0000
2	30	0.0000	0.0181	0.0000
29	38	0.0008	0.0156	0.0000
19	20	0.0007	0.0138	0.0000
L	ı	1	1	1

Table A. 6: Load Data

Bus	Tyma	Voltage	L	oad	Gen	erator
Dus	Type	Voltage	MW	MVar	MW	MVar
1	PQ	-	0.0	0.0	0.0	0.0
2	PQ	-	0.0	0.0	0.0	0.0
3	PQ	-	322.0	2.4	0.0	0.0
4	PQ	-	500.0	184.0	0.0	0.0
5	PQ	-	0.0	0.0	0.0	0.0
6	PQ	-	0.0	0.0	0.0	0.0
7	PQ	-	233.8	84.0	0.0	0.0
8	PQ	-	522.0	176.0	0.0	0.0
9	PQ	-	0.0	0.0	0.0	0.0
10	PQ	-	0.0	0.0	0.0	0.0
11	PQ	-	0.0	0.0	0.0	0.0
12	PQ	-	07.5	88.00	0.0	0.0
13	PQ	-	0.0	0.0	0.0	0.0
14	PQ	-	0.0	0.0	0.0	0.0
15	PQ	-	320.0	153.0	0.0	0.0
16	PQ	-	329.0	32.3	0.0	0.0
17	PQ	-	0.0	0.0	0.0	0.0
18	PQ	-	158.0	30.0	0.0	0.0
19	PQ	-	0.0	0.0	0.0	0.0
20	PQ	-	628.0	103.0	0.0	0.0
21	PQ	-	274.0	115.0	0.0	0.0
22	PQ	-	0.0	0.0	0.0	0.0
23	PQ	-	247.5	84.6	0.0	0.0
24	PQ	-	308.6	-92.0	0.0	0.0
25	PQ		224.0	47.2	0.0	0.0
26	PQ	-	139.0	17.0	0.0	0.0

27	PQ	-	281.0	75.5	0.0	0.0
28	PQ	-	206.0	27.6	0.0	0.0
29	PQ	-	283.5	26.9	0.0	0.0
30	PV	1.0475	0.0	0.0	250.0	-
31	PV	0.9820	9.2	4.6	-	-
32	PV	0.9831	0.0	0.0	650.0	-
33	PV	0.9972	0.0	0.0	632.0	-
34	PV	1.0123	0.0	0.0	508.0	-
35	PV	1.0493	0.0	0.0	650.0	-
36	PV	1.0635	0	0	560	
37	PV	1.0278	0	0	540	
38	PV	1.0265	0	0	830	
39	PV	1.0300	1104.0	250.0	1000	

A. 5 Parameter Data of IEEE 9 bus Test System

Table A. 7: Generator Data of IEEE 9 bus system

Generator	Н	R_a	X'_d	X_q'	X_d	X_q	T'_{do}	T_{qo}'
G1	23.64	0	0.0608	0.0969	0.146	0.0969	8.96	0.31
G2	6.4	0	0.1198	0.1969	0.8958	0.8645	6.0	0.535
G3	3.01	0	0.1813	0.25	1.3125	1.2578	5.89	0.6

Table A. 8: Exciter Data of IEEE 9 bus system

Generator	K_A	T_A	K_E	T_E	K_F	T_F
G1	20	0.2	1.0	0.314	0.063	0.35
G2	20	0.2	1.0	0.314	0.063	0.35
G3	20	0.2	1.0	0.314	0.063	0.35

Table A. 9: Line parameters of IEEE 9 bus system

From Bus	To Bus	R	X	В
1	4	0.0	0.0576	0.0
4	5	0.01	0.085	0.176
5	7	0.032	0.161	0.306
4	6	0.017	0.092	0.158
6	9	0.039	0.17	0.358
7	8	0.0085	0.072	0.149
3	9	0.0	0.0586	0.0
8	9	0.0119	0.1008	0.209
2	7	0.0	0.0625	0.0

Table A. 10: Bus Data of IEEE 9 bus system

Bus	Туре	Voltage	Loa	ıd	Generator	
Dus		(p.u)	P_L (p.u)	Q_L (p.u)	P (p.u)	Q (p.u)
1	PV	1.04	-	-	0.716	0.27
2	PV	1.025∠9.3 ⁰	-	-	1.63	0.067
3	PV	1.025∠4.7 ⁰	-	-	0.85	-0.109
4	PQ	-	-	-	-	-
5	PQ	-	1.25	0.5	-	-
6	PQ	-	0.9	0.3	-	-
7	PQ	-	-	-	-	-
8	PQ	-	1.0	0.35	-	-
9	PQ	-	-	-	-	-

Appendix B

List of Publications

Journal Publications

- 1. B. Sahu and B. P. Padhy, "Evaluation of Damping Effect Influenced by System Parameters on a DFIG Integrated Power System," in *IEEE Systems Journal*, vol. 17, no. 2, pp. 1939-1949, June 2023, doi: 10.1109/JSYST.2023.3239933.
- 2. B. Sahu and B. P. Padhy, "Design of Power System Stabilizer for DFIG-Based Wind Energy Integrated Power Systems under Combined Influence of PLL and Virtual Inertia Controller," in *Journal of Modern Power Systems and Clean Energy*, doi: 10.35833/MPCE.2023.000202.
- 3. B. Sahu and B. P. Padhy, "Probabilistic Sensitivity Analysis Of Large-Scale Solar PV Integrated Power System," in *Electric Power Systems Research. (Under Review)*.
- 4. (Under Review).

Conference Publications

- 1. B. Sahu and B. P. Padhy, "Stability Analysis of Power system Connected to Wind Farm Using Eigenvalue Sensitivity Approach," 2021 9th IEEE International Conference on Power Systems (ICPS), Kharagpur, India, 2021, pp. 1-6, doi: 10.1109/ICPS52420.2021.9670402.
- 2. B. Sahu and B. P. Padhy, "Small Signal Stability Analysis of DFIG Integrated Power System Considering PLL Dynamics Under Different Grid Strengths," 2023 IEEE PES Conference on Innovative Smart Grid Technologies Middle East (ISGT Middle East), Abu Dhabi, United Arab Emirates, 2023, pp. 1-5, doi: 10.1109/ISGTMiddleEast56437.2023.10078449.
- 3. B. Sahu and B. P. Padhy, "Impact of Large-Scale PV-BESS on Dynamics of Power System Oscillatory Modes," 2023 3rd International Conference on Energy, Power and Electrical Engineering (EPEE), Wuhan, China, 2023, pp. 1333-1338, doi: 10.1109/EPEE59859.2023.10351868

References

- [1] [Online]. Available: https://earthobservatory.nasa.gov/world-of-change/global-temperatures. [Accessed 06 04 2024].
- [2] [Online]. Available: https://www.irena.org/Publications/2024/Mar/Renewable-capacity-statistics-2024. [Accessed 06 04 2024].
- [3] N. Golait, R. M. Moharil and P. S. Kulkarni, "Wind electric power in the world and perspectives of its development in India," *Renewable and Sustainable Energy Reviews*, vol. 13, no. 1, pp. 233-247, 2009.
- [4] L. Schleisner, "Life cycle assessment of a wind farm and related externalities," *Renewable Energy*, vol. 20, no. 3, pp. 279-288, 2000.
- [5] H. A. Pulgar Painemal, "Wind farm model for power system stability analysis," 2011.
- [6] Festo Didactic, "Principles of Doubly-Fed Induction," Festo Didactic Ltd, Canada, 2015.
- [7] S. Liu, X. P. Liu and X. Wang and . X. Wang, "Stochastic Small-Signal Stability Analysis of Grid-Connected Photovoltaic Systems," *IEEE Transactions on Industrial Electronics*, vol. 63, no. 2, pp. 1027-1038, Feb. 2016.
- [8] A. A. Eshkaftaki, A. Rabiee, A. Kargar and S. T. Boroujeni, "An Applicable Method to Improve Transient and Dynamic Performance of Power System Equipped With DFIG-Based Wind Turbines," *IEEE Transactions on Power Systems*, vol. 35, pp. 2351-2361, 2020.
- [9] W. Du, J. Bi, J. Cao and H. F. Wang, "A Method to Examine the Impact of Grid Connection of the DFIGs on Power System Electromechanical Oscillation Modes," *IEEE Transactions on Power Systems*, vol. 31, pp. 3775-3784, 2016.
- [10] J. Quintero, V. Vittal, G. Heydt and H. Zhang, "The impact of increased penetration of converter control-based generators on power system modes of oscillation," in 2015 IEEE Power Energy Society General Meeting, 2015.

- [11] H. Pulgar-Painemal, Y. Wang and H. Silva-Saravia, "On Inertia Distribution, Inter-Area Oscillations and Location of Electronically-Interfaced Resources," *IEEE Transactions on Power Systems*, vol. 33, pp. 995-1003, 2018.
- [12] J. G. Slootweg and W. L. Kling, "The impact of large scale wind power generation on power system oscillations," *Electric Power Systems Research*, 2003.
- [13] W. Du, W. Dong and H. F. Wang, "Small-Signal Stability Limit of a Grid-Connected PMSG Wind Farm Dominated by the Dynamics of PLLs," *IEEE Transactions on Power Systems*, vol. 35, pp. 2093-2107, 2020.
- [14] L. Yang, Z. Xu, J. Østergaard, Z. Y. Dong, K. P. Wong and X. Ma, "Oscillatory Stability and Eigenvalue Sensitivity Analysis of A DFIG Wind Turbine System," *IEEE Transactions on Energy Conversion*, vol. 26, pp. 328-339, 2011.
- [15] W. Du, Y. Wang, H. Wang, X. Xiao, X. Wang and X. Xie, "Analytical Examination on the Amplifying Effect of Weak Grid Connection for the DFIGs to Induce Torsional Subsynchronous Oscillations," *IEEE Transactions on Power Delivery*, vol. 35, pp. 1928-1938, 2020.
- [16] M. Li, L. Xiong, H. Chai, L. Xiu and J. Hao, "Mechanism of PV Generation System Damping Electromechanical Oscillations," *IEEE Access*, vol. 8, pp. 135853-135865, 2020.
- [17] S. Q. Bu, X. Zhang, J. B. Zhu and X. Liu, "Comparison analysis on damping mechanisms of power systems with induction generator based wind power generation," *International Journal of Electrical Power & Energy Systems*, vol. 97, pp. 250-261, 2018.
- [18] J. Bi, H. Sun, S. Xu, R. Song, B. Zhao and Q. Guo, "Mode-based damping torque analysis method in power system low-frequency oscillations," *CSEE Journal of Power and Energy Systems*, pp. 1-10, 2020.
- [19] J. Luo, S. Bu, J. Zhu and C. Y. Chung, "Modal Shift Evaluation and Optimization for Resonance Mechanism Investigation and Mitigation of Power Systems Integrated With FCWG," *IEEE Transactions on Power Systems*, vol. 35, pp. 4046-4055, 2020.

- [20] D. Brahma and N. Senroy, "Sensitivity-Based Approach for Assessment of Dynamic Locational Grid Flexibility," *IEEE Transactions on Power Systems*, vol. 35, pp. 3470-3480, 2020.
- [21] P. He, S. A. Arefifar, C. Li and Y. Tao, "Small signal stability analysis of doubly-fed induction generator-integrated power systems based on probabilistic eigenvalue sensitivity indices," *IET Generation, Transmission Distribution*, vol. 13, pp. 3127-3137, 2019.
- [22] P. H. A. Barra, W. C. de Carvalho, T. S. Menezes, R. A. S. Fernandes and D. V. Coury, "A review on wind power smoothing using high-power energy storage systems," *Renewable and Sustainable Energy Reviews*, vol. 137, p. 110455, 2021.
- [23] W. Jin and Y. Lu, "Stability Analysis and Oscillation Mechanism of the DFIG-Based Wind Power System," *IEEE Access*, vol. 7, pp. 88937-88948, 2019.
- [24] J. Liu, W. Yao, J. Wen, J. Fang, L. Jiang, H. He and S. Cheng, "Impact of Power Grid Strength and PLL Parameters on Stability of Grid-Connected DFIG Wind Farm," *IEEE Transactions on Sustainable Energy*, vol. 11, pp. 545-557, 2020.
- [25] J. Ekanayake and N. Jenkins, "Comparison of the response of doubly fed and fixed-speed induction generator wind turbines to changes in network frequency," *IEEE Transactions on Energy Conversion*, vol. 19, pp. 800-802, 2004.
- [26] Z. Wang, C. Shen and F. Liu, "Impact of DFIG with phase lock loop dynamics on power systems small signal stability," in 2014 IEEE PES General Meeting | Conference Exposition, 2014.
- [27] K. H. LaCommare, "Review of the Recent Frequency Performance of the Eastern, Western and ERCOT Interconnections," *Lawrence Berkeley National Laboratory*, 2011.
- [28] M. F. M. Arani and Y. A.-R. I. Mohamed, "Analysis and Mitigation of Undesirable Impacts of Implementing Frequency Support Controllers in Wind Power Generation," *IEEE Transactions on Energy Conversion*, vol. 31, pp. 174-186, 2016.

- [29] E. Rakhshani, A. Perilla, J. L. R. Torres, F. M. Gonzalez-Longatt, T. B. Soeiro and M. A. M. M. Van Der Meijden, "FAPI Controller for Frequency Support in Low-Inertia Power Systems," *IEEE Open Access Journal of Power and Energy*, vol. 7, pp. 276-286, 2020.
- [30] Y. Wang, J. Meng, X. Zhang and L. Xu, "Control of PMSG-Based Wind Turbines for System Inertial Response and Power Oscillation Damping," *IEEE Transactions on Sustainable Energy*, vol. 6, pp. 565-574, 2015.
- [31] A. B. T. Attya and J. L. Dominguez-García, "Insights on the Provision of Frequency Support by Wind Power and the Impact on Energy Systems," *IEEE Transactions on Sustainable Energy*, vol. 9, pp. 719-728, 2018.
- [32] M. Garmroodi, D. J. Hill, G. Verbič and J. Ma, "Impact of Tie-Line Power on Inter-Area Modes With Increased Penetration of Wind Power," *IEEE Transactions on Power Systems*, vol. 31, pp. 3051-3059, 2016.
- [33] E. Rakhshani, D. Gusain, V. Sewdien, J. L. Rueda Torres and M. A. M. M. Van Der Meijden, "A Key Performance Indicator to Assess the Frequency Stability of Wind Generation Dominated Power System," *IEEE Access*, vol. 7, pp. 130957-130969, 2019.
- [34] A. Ashouri-Zadeh and M. Toulabi, "Adaptive Virtual Inertia Controller for DFIGs Considering Nonlinear Aerodynamic Efficiency," *IEEE Transactions on Sustainable Energy*, vol. 12, pp. 1060-1067, 2021.
- [35] C. Zhong, J. Zhang and Y. Zhou, "Adaptive Virtual Capacitor Control for MTDC System With Deloaded Wind Power Plants," *IEEE Access*, vol. 8, pp. 190582-190595, 2020.
- [36] M. Sun, Y. Min, L. Chen, K. Hou, D. Xia and H. Mao, "Optimal auxiliary frequency control of wind turbine generators and coordination with synchronous generators," *CSEE Journal of Power and Energy Systems*, vol. 7, pp. 78-85, 2021.
- [37] V. Gholamrezaie, M. G. Dozein, H. Monsef and B. Wu, "An Optimal Frequency Control Method Through a Dynamic Load Frequency Control (LFC) Model Incorporating Wind Farm," *IEEE Systems Journal*, vol. 12, pp. 392-401, 2018.

- [38] J. Ma, Y. Zhang, Y. Shen, P. Cheng and A. G. Phadke, "Equipment-Level Locating of Low Frequency Oscillating Source in Power System With DFIG Integration Based on Dynamic Energy Flow," *IEEE Transactions on Power Systems*, vol. 35, pp. 3433-3447, 2020.
- [39] J. Ma, Y. Qiu, Y. Li, W. Zhang, Z. Song and J. S. Thorp, "Research on the Impact of DFIG Virtual Inertia Control on Power System Small-Signal Stability Considering the Phase-Locked Loop," *IEEE Transactions on Power Systems*, vol. 32, pp. 2094-2105, 2017.
- [40] M. N. H. Shazon, N. Al-Masood and A. Jawad, "Frequency control challenges and potential countermeasures in future low-inertia power systems: A review," *Energy Reports*, vol. 8, pp. 6191-6219, 2022.
- [41] P. Hu, Y. Li, Y. Yu and F. Blaabjerg, "Inertia estimation of renewable-energy-dominated power system," *Renewable and Sustainable Energy Reviews*, vol. 183, p. 113481, 2023.
- [42] M. Haugen, H. Farahmand and S. e. a. Jaehnert, "Representation of uncertainty in market models for operational planning and forecasting in renewable power systems: a review. Energy Syst (2023).," *Energy Systems*, 2023.
- [43] B. S. C. S. B. R. R Kumar, "A control topology for frequency regulation capability in a grid integrated PV system," *Archives of Electrical Engineering*, vol. 69, no. 2, pp. 389-401, 2020.
- [44] J. Khazaei, Z. Tu and W. Liu, "Small-Signal Modeling and Analysis of Virtual Inertia-Based PV Systems," *IEEE Transactions on Energy Conversion*, vol. 35, pp. 1129-1138, 2020.
- [45] X. Zhao, J. Wu, L. Guo, S. Wang and D. Zhao, "Primary Frequency Regulation Strategy for Combined Wind-storage System Based on Improved Virtual Inertia Integrated Control," in 2023 3rd New Energy and Energy Storage System Control Summit Forum (NEESSC), 2023.
- [46] B. Yuan, M. Zhou, G. Li and X.-P. Zhang, "Stochastic Small-Signal Stability of Power Systems With Wind Power Generation," *IEEE Transactions on Power Systems*, vol. 30, pp. 1680-1689, 2015.

- [47] W. C. Wong and C. Y. Chung, "Coordinated Damping Control Design for DFIG-Based Wind Generation Considering Power Output Variation," *IEEE Transactions on Power Systems*, vol. 27, pp. 1916-1925, 2012.
- [48] J. Ma, Z. Song, Y. Zhang, Y. Zhao and J. S. Thorp, "Robust Stochastic Stability Analysis Method of DFIG Integration on Power System Considering Virtual Inertia Control," *IEEE Transactions on Power Systems*, vol. 32, pp. 4069-4079, 2017.
- [49] J. A. O. Lala and C. F. Gallardo, "Adaptive Tuning of Power System Stabilizer Using a Damping Control Strategy Considering Stochastic Time Delay," *IEEE Access*, vol. 8, pp. 124254-124264, 2020.
- [50] A. Prakash, M. S. E. Moursi, S. K. Parida and E. F. El-Saadany, "Design of Adaptive Damping Controller With Wide-Area Measurements Considering Unknown Power System Dynamics," *IEEE Transactions on Power Systems*, pp. 1-13, 2023.
- [51] H. Sheng and X. Wang, "Online Measurement-Based Estimation of Dynamic System State Matrix in Ambient Conditions," *IEEE Transactions on Smart Grid*, vol. 11, pp. 95-105, 2020.
- [52] L. Liu, Z. Hu and A. Mujeeb, "Automatic Generation Control Considering Uncertainties of the Key Parameters in the Frequency Response Model," *IEEE Transactions on Power Systems*, vol. 37, pp. 4605-4617, 2022.
- [53] S. Liu, P. X. Liu and X. Wang, "Stochastic Small-Signal Stability Analysis of Grid-Connected Photovoltaic Systems," *IEEE Transactions on Industrial Electronics*, vol. 63, pp. 1027-1038, 2016.
- [54] A. Singla, K. Singh and V. K. Yadav, "Optimization of Distributed Solar Photovoltaic Power Generation in Day-ahead Electricity Market Incorporating Irradiance Uncertainty," *Journal of Modern Power Systems and Clean Energy*, vol. 9, pp. 545-560, 2021.
- [55] T. M. D. J. Vikas Singh, "Probabilistic Steady Analysis of Power System with Photo Voltaic Generations," in *Renewable Energy Integration to the Grid*, CRC Press, 2022, pp. 199-238.

- [56] S. Saha, M. I. Saleem and T. K. Roy, "Impact of high penetration of renewable energy sources on grid frequency behaviour," *International Journal of Electrical Power & Energy Systems*, vol. 145, p. 108701, 2023.
- [57] J. W. Shim, G. Verbič and K. Hur, "Stochastic Eigen-Analysis of Electric Power System With High Renewable Penetration: Impact of Changing Inertia on Oscillatory Modes," *IEEE Transactions on Power Systems*, vol. 35, pp. 4655-4665, 2020.
- [58] D. Métivier, M. Vuffray and S. Misra, "Efficient polynomial chaos expansion for uncertainty quantification in power systems," *Electric Power Systems Research*, vol. 189, p. 106791, 2020.
- [59] V. A. Maslennikov, J. V. Milanovic and S. M. Ustinov, "Robust ranking of loads by using sensitivity factors and limited number of points from a hyperspace of uncertain parameters," *IEEE Transactions on Power Systems*, vol. 17, pp. 565-570, 2002.
- [60] C. Y. Chung, K. W. Wang, C. T. Tse and R. Niu, "Power-system stabilizer (PSS) design by probabilistic sensitivity indexes (PSIs)," *IEEE Transactions on Power Systems*, vol. 17, pp. 688-693, 2002.
- [61] C. Shuai, Y. Deyou, G. Weichun, L. Chuang, C. Guowei and K. Lei, "Global sensitivity analysis of voltage stability in the power system with correlated renewable energy," *Electric Power Systems Research*, vol. 192, p. 106916, 2021.
- [62] I. A. Hiskens and J. Alseddiqui, "Sensitivity, Approximation, and Uncertainty in Power System Dynamic Simulation," *IEEE Transactions on Power Systems*, vol. 21, pp. 1808-1820, 2006.
- [63] E. Borgonovo and L. Peccati, "Uncertainty and global sensitivity analysis in the evaluation of investment projects," *International Journal of Production Economics*, vol. 104, pp. 62-73, 2006.

- [64] H. R. Lee, H. Y. Kim, J. H. Jeon and Y. J. Kang, "Application of global sensitivity analysis to statistical energy analysis: Vehicle model development and transmission path contribution," *Applied Acoustics*, vol. 146, pp. 368-389, 2019.
- [65] F. Sarrazin, F. Pianosi and T. Wagener, "Global Sensitivity Analysis of environmental models: Convergence and validation," *Environmental Modelling & Software*, vol. 79, pp. 135-152, 2016.
- [66] A. Miftakhova, "Global sensitivity analysis for optimal climate policies: Finding what truly matters," *Economic Modelling*, vol. 105, p. 105653, 2021.
- [67] S. M. T. P. M. e. a. Parpia, "Sensitivity analysis in clinical trials: three criteria for a valid sensitivity analysis," *Eye*, vol. 36, p. 2073–2074, 2022.
- [68] K. N. Hasan, R. Preece and J. V. Milanović, "Priority Ranking of Critical Uncertainties Affecting Small-Disturbance Stability Using Sensitivity Analysis Techniques," *IEEE Transactions on Power Systems*, vol. 32, pp. 2629-2639, 2017.
- [69] R. Preece and J. V. Milanović, "Assessing the Applicability of Uncertainty Importance Measures for Power System Studies," *IEEE Transactions on Power Systems*, vol. 31, pp. 2076-2084, 2016.
- [70] "Executive summary," 2022. [Online]. Available: https://www.iea.org/reports/renewables-2023/executive-summary. [Accessed 4 Aug. 2023].
- [71] J. W. Shim, G. Verbič and K. Hur, "Stochastic Eigen-Analysis of Electric Power System With High Renewable Penetration: Impact of Changing Inertia on Oscillatory Modes," *IEEE Transactions on Power Systems*, vol. 35, no. 6, pp. 4655-4665, Nov. 2020.
- [72] R. Kumar, B. Sahu, C. K. Shiva and B. Rajender, "A control topology for frequency regulation capability in a grid integrated PV system," *Archives of Electrical Engineering*, vol. 69, no. 2, p. 389–401, 2020.

- [73] R. Liu, Z. Wang and H. Xing, "Virtual Inertia Control Strategy for Battery Energy Storage System in Wind Farm," in *Asia-Pacific Power and Energy Engineering Conference (APPEEC)*, Macao, China, 2019.
- [74] U. Datta, A. Kalam and J. Shi, "Battery Energy Storage System Control for Mitigating PV Penetration Impact on Primary Frequency Control and State-of-Charge Recovery," *IEEE Transactions on Sustainable Energy*, vol. 11, no. 2, pp. 746-757, April 2020.
- [75] X. Zhou, S. Cheng, X. Wu and X. Rao, "Influence of Photovoltaic Power Plants Based on VSG Technology on Low Frequency Oscillation of Multi-Machine Power Systems," *IEEE Transactions on Power Delivery*, vol. 37, no. 6, pp. 746-757, Dec. 2022.
- [76] K. Kumar, . A. Prakash, P. Singh and S. K. Parida, "Large-Scale Solar PV Converter Based Robust Wide-Area Damping Controller for Critical Low Frequency Oscillations in Power Systems," *IEEE Transactions on Industry Applications*, vol. 59, pp. 4868-4879, 2023.
- [77] Y. Zhu, C. Liu, B. Wang and K. Sun, "Damping control for a target oscillation mode using battery energy storage," *Journal of Modern Power Systems and Clean Energy*, vol. 6, no. 4, pp. 833-845, July 2018.
- [78] Y. L. Jiang, Z.-Z. Qi and P. Yang, "Model Order Reduction of Linear Systemsvia the Cross Gramian and SVD," *IEEE TRANSACTIONS ON CIRCUITS AND SYSTEMS—II: EXPRESS BRIEFS*, 2019.
- [79] M. A. P. Peter W. Sauer, Power System Dynamics and Stability, Prentice Hall, 1998.
- [80] H. A. Pulgar-Painemal and P. W. Sauer, "Power system modal analysis considering doubly-fed induction generators," in 2010 IREP Symposium Bulk Power System Dynamics and Control VIII (IREP), 2010.
- [81] W. Du, H. Wang and S. Bu, Small-Signal Stability Analysis of Power Systems Integrated with Variable Speed Wind Generators, Springer, 2018.

- [82] S. Xia, Q. Zhang, S. T. Hussain, B. Hong and W. Zou, "Impacts of Integration of Wind Farms on PowerSystem Transient Stability," *Applied Sciences*, 2018.
- [83] B. Pal and B. Chaudhuri, Robust Control in Power Systems, Springer US, 2005.
- [84] P. Kundur, M. Klein, G. J. Rogers and M. S. Zywno, "Application of power system stabilizers for enhancement of overall system stability," *IEEE Transactions on Power Systems*, vol. 4, pp. 614-626, 1989.
- [85] D. Zhang, Y. Wang, J. Hu, S. Ma, Q. He and Q. Guo, "Impacts of PLL on the DFIG-based WTG's electromechanical response under transient conditions: analysis and modeling," CSEE Journal of Power and Energy Systems, vol. 2, pp. 30-39, 2016.
- [86] E. V. Larsen and D. A. Swann, "Applying Power System Stabilizers Part III: Practical Considerations," *IEEE Power Engineering Review*, Vols. PER-1, pp. 63-63, 1981.
- [87] E. V. Larsen and D. A. Swarm, "Applying Power system Stabilizers Part II: PerformanceObjectives and Tuning Concepts," *IEEE Transactions on Power Apparatus and Systems*, vol. 100, no. 6, pp. 3025-3033, 1981.
- [88] F. P. Demello and C. Concordia, "Concepts of Synchronous Machine Stability as Affected by Excitation Control," *IEEE Transactions on Power Apparatus and Systems*, vol. 88, no. 4, pp. 316-329, 1969.
- [89] A. Saltelli, P. Annoni, I. Azzini, F. Campolongo, M. Ratto and S. Tarantola, "Variance based sensitivity analysis of model output. Design and estimator for the total sensitivity index," *Computer Physics Communications*, vol. 181, pp. 259-270, 2010.
- [90] S. Tarantola, D. Gatelli and T. A. Mara, "Random balance designs for the estimation of first order global sensitivity indices," *Reliability Engineering & System Safety*, vol. 91, pp. 717-727, 2006.
- [91] E. Borgonovo, "A new uncertainty importance measure," *Reliability Engineering & System Safety*, vol. 92, pp. 771-784, 2007.

- [92] F. Pianosi and T. Wagener, "A simple and efficient method for global sensitivity analysis based on cumulative distribution functions,," *Environmental Modelling & Software*, vol. 67, pp. 1-11, 2015.
- [93] B. Sahu and B. P. Padhy, "Evaluation of Damping Effect Influenced by System Parameters on a DFIG Integrated Power System," *IEEE Systems Journal*, vol. 17, pp. 1939-1949, 2023.
- [94] B. Sahu and B. P. Padhy, "Impact of Large-Scale PV-BESS on Dynamics of Power System Oscillatory Modes," in 2023 3rd International Conference on Energy, Power and Electrical Engineering (EPEE), 2023.
- [95] E. Zhou, O. P. Malik and G. S. Hope, "Design of stabilizer for a multimachine power system based on the sensitivity of PSS effect," *IEEE Transactions on Energy Conversion*, vol. 7, pp. 606-613, 1992.
- [96] B. Sahu and B. P. Padhy, "Design of Power System Stabilizer for DFIG-based Wind Energy Integrated Power Systems Under Combined Influence of PLL and Virtual Inertia Controller," *Journal of Modern Power Systems and Clean Energy*, vol. 12, pp. 524-534, 2024.
- [97] C. Lv, W. Du and T. Littler, "Damping torque analysis of power systems with DFIG wind turbine generators," in *International Conference on Renewable Power Generation (RPG 2015)*, 2015.